The deep structure of Axial Volcano

Michael Edwin West

Submitted in partial fulfillment of the
requirements for the degree
of Doctor of Philosophy in the
Graduate School of Arts and Sciences

COLUMBIA UNIVERSITY

2001

Abstract

The deep structure of Axial Volcano

Michael West

The subsurface structure of Axial Volcano, near the intersection of the Juan de Fuca Ridge and the Cobb–Eickelberg seamount chain in the northeast Pacific, is imaged from an active source seismic experiment. At a depth of 2.25 to 3.5 km beneath Axial lies an 8 km x 12 km region of very low seismic velocities that can only be explained by the presence of magma. In the center of this magma storage chamber at 2–3.5 km below sea floor, the crust is at least 10–20% melt. At depths of 4–5 km there is evidence of additional low concentrations of magma (a few percent) over a larger area. In total, 5–11 km^3 of magma are stored in the mid–crust beneath Axial. This is more melt than has been positively identified under any basaltic volcano on Earth. It is also far more than the 0.1–0.2 km^3 emplaced during the 1998 eruption. The implied residence time in the magma reservoir of a few hundred to a few thousand years agrees with geochemical trends which suggest prolonged storage and mixing of magmas. The large volume of melt bolsters previous observations that Axial provides much of the material to create crust along its 50 km rift zones. A high velocity ring–shaped feature sits above the magma chamber just outside the caldera walls. This feature is believed to be the result of repeated dike injections from the magma body to the surface during the construction of the volcanic edifice. A rapid change in crustal thickness from 8 to 11 km within 15 km of the caldera implies

focused delivery of melt from the mantle. The high flux of magma suggests that melting occurs deeper in the mantle than along the nearby ridge. Melt supply to the volcano is not connected to any plumbing system associated with the adjacent segments of the Juan de Fuca Ridge. This suggests that, despite Axial's proximity to the ridge, the Cobb hot spot currently drives the supply of melt to the volcano.

Contents

I. Problems and Objectives

II. Airgun–to–OBS seismic experiment

III. The velocity structure of Axial Volcano

Synthesis of Chapter 3 and 4 to be submitted to *Journal of Geophysical Review.*

IV. Massive magma reservoir beneath Axial Volcano, Juan de Fuca Ridge

V. Regional and upper mantle observations at Axial Volcano

Section 5.2, 5.3, 5.4 in preparation for submission to *Geophysical Research Letters*.

Appendix: Shallow crustal magma chamber beneath the axial high of the Coaxial Segment of Juan de Fuca Ridge at the "Source Site" of the 1993 eruption

W. Menke, M. West, M. Tolstoy, S. Webb and R. Sohn

Acknowledgements

Four people deserve special recognition for their roles, direct or indirect, in this thesis. They have all nurtured me and are responsible for who I have become as a scientist (or for at least the good parts). Their influences are intertwined and compliment each other to the point I sometimes question taking credit for anything I have done.

Charles West, my father, is responsible for introducing me to the vast world that lies on the outside of the windows behind which we all spend too much time. His excitement for the natural world rubbed off on me during the countless hours we have spent one–on–one over thirty years. While his influence was great when I was young, he continues to inspire and influence more of my life than is perhaps recognized. This, together with his example of honest living, has determined much of who I am today (not to mention my academic interests). Simply put, he taught me to explore the world and, to steal from Thoreau..., live deliberately.

Marcia West, my mother, provided the compass by which I try to live. Her unwavering values and respect for other people have shown me what is important in life and how our personal behavior can have a tremendous ripple effect on others. She also taught me the value of time and how to get things done. From times tables to French to *Great Expectations*, she taught me academic perseverance – never an easy task with me. On a practical level, I will never be able to repay her tireless 11th–hour science fair assistance.

I am indebted to William Menke for his selfless and compassionate approach to mentoring. His every action during my tenure at Lamont has been in my best interest. He has provided a role model for what it means to advise. I expect I will spend much of my career trying to emulate his advising style. His drive to distill complex thought to intuitive explanations is unrivaled. His clarity impacts countless endeavors around Lamont, most without formal recognition. Bill is a teacher *par excellence*, colleague and friend.

Above all, I am indebted to Krista. From day one at Lamont (actually it was about day 11) she has challenged me and pushed me to be the best scientist and teacher I can be. Her daily support and perspective on life have made graduate school an enviable experience. She has shaped my thoughts about Earth science and is in many ways responsible for the academic directions I have taken. She has opened my eyes to the other half of the natural sciences – that which focusses on life as opposed to dirt. Never did I imagine that I would leave graduate school knowing and caring so much about turtles, geraniums and ecology. We share a different but complimentary awe for the world and I am profoundly happy to be exploring it together.

I. Problems and Objectives

1.1 Introduction

1.1.1 Motivation

The emergence of plate tectonics in the late 1960s allowed different aspects of Earth science to be unified under a single elegant concept. Mid–ocean ridges were recognized as the source of new crust in the ocean basins. Mountain ranges resulted from collisions between continents or volcanism. Ocean trenches resulted from the subduction of one tectonic plate under another. Even earthquakes took on new meaning as they were the direct consequence of the movement of plates.

Plate tectonics also provides simple explanations for the gross location of volcanoes. Volcanoes above subduction zones are triggered by the byproducts of the down–going slab. Mid–ocean ridge volcanism is the effect of passive upwelling mantle beneath the ridge. Hot spot volcanism, while still debated, results from long–lived perturbations in the mantle.

These explanations of volcanism describe mantle processes whose products are visible on the surface of the planet. However, between the mantle source and Earth's surface lie many kilometers of crust which molten magma must traverse before it is erupted. We know very little about how magma is transported, stored and erupted in the crust. For proof, one need only look at the many popular and

scientific depictions of magma in the crust – pipes which channel magma into and out of magma storage reservoirs, inverted tear drops migrating up through the crust, partially molten mush from which melt is extracted (fig. 1.1).

In defense of these ideas, the fact that unifying explanations remain elusive is testimony to the difficulty of the problem. With the exception of a few small areas of ophiolites and plutons (exposed sections of ancient mid–ocean ridges and magma intrusion), few of these transport mechanisms have been observed first hand. Similarly, there is only scant evidence revealing the structure of the magma storage chambers thought to exist under many volcanoes.

An understanding of how magmatic systems really work has applications in fundamental and applied geology. There are few more basic questions in geology than understanding the process which created most of the land around us (including the Palisades sill on which Lamont is built). Though we observe this process on Earth today, it remains partially unexplained because it occurs out of sight, beneath the surface. On an applied level, magma transport in the crust is one of the few phenomena where human and geologic timescales overlap. Sometimes the effects of magmatic processes are visible on the scale of days, hours and even seconds. A great deal of effort is expended world–wide to understand the magma which actually makes it to the surface during volcanic eruptions. This is an incidental effect of a larger process going on at depth. It is my belief, that if we are ever going to understand eruptive processes at the surface, we must first understand what is happening deep in the crust to cause

magma to rise to the surface.

This thesis is a contribution to our understanding of how magma is stored and distributed in the crust. Using a combination of seismic methods, and comparisons with bathymetric, gravitational and geochemical data, this thesis directly images the deep structure of one volcano. While it does not attempt to answer all our questions about volcanic processes, it offers new insight into key issues including magma storage, the production and structure of the crust and the competing roles of hot spots and ocean ridges.

1.1.2 Why Axial?

Axial Volcano, near the Juan de Fuca Ridge in the northeast Pacific, is an ideal place to undertake such a seismic imaging project. It shares many features with mid−ocean ridges, which have been well studied during the past 2 decades. Yet it is a singular volcano similar in many aspects to terrestrial volcanoes in Iceland, Hawaii and elsewhere.

For twenty years Axial Volcano has been the focus of intense research. From the original morphologic puzzle posed by an intersecting ridge and seamount chain, to the discovery of thriving hydrothermal vent communities, to having the first closely−monitored marine volcanic eruptions, Axial has fed a steady stream of questions and answers into several Earth science disciplines. Though Axial has long benefited from its close proximity to the Pacific Northwest coast, its significance is justified on many scientific levels.

Axial and its surroundings have been mapped, scanned, sampled, dredged, and monitored as much as any patch of the deep seafloor. As many theories exist to explain Axial's features as there have been cruises. Yet surprisingly little work has been done to illuminate the deep structure of Axial Volcano. From the bias of a solid Earth geophysicist, knowledge of the structure beneath the surface is paramount to understanding Axial. It is this magmatic plumbing that controls eruption activity, surface morphology, hydrothermal activity, petrologic signature and water column chemistry and temperature.

The motivations for this thesis are three−fold:

    1. to better understand the magmatic systems under all basaltic volcanoes.

    2. to weigh the competing magmatic influences of the Juan de Fuca ridge and the Cobb hot spot.

    3. to provide a template on which other research at Axial may be interpreted.

1.2 On a ridge and a hot spot

1.2.1 Juan de Fuca ridge plate and ridge

The Juan de Fuca plate, off the coast of Washington and Oregon, is the last remaining corner of an ancient tectonic plate that has largely been subducted beneath North America. The western edge of this plate meets the Pacific plate along the Juan de Fuca ridge (fig. 1.2). This mid−ocean ridge is spreading apart at an intermediate rate of 5−6 cm/yr roughly perpendicular to the ridge axis. It is

divided into 7 offset segments of 75–150 km each and is bounded to the north by the Nootka fault zone and to south by the Blanco fracture zone (Wilson 1988). The spreading rate at the northern end of the ridge is up to 0.5 cm/yr greater than in the south causing ridge segment tips to propagate along the ridge axis in lieu of developing stable transform faults. Today, clear transform faults are not found along most of the Juan de Fuca (JdF) Ridge.

Geochemically, most lavas erupted along the Juan de Fuca are relatively depleted of incompatible elements. Some enriched lavas are found along the Endeavour segment, slight enrichment is observed near Axial Volcano, and unusually depleted basalt is common along the CoAxial segment. But overall, JdF chemistries are similar to "normal" mid–ocean ridge basalt. Though the segments are structurally distinct, there is limited variation in their chemistries with the exception of Endeavour and CoAxial (Delaney *et al.* 1981, Rhodes *et al.* 1990, Perfit *et al.* 1988). Like many ridges, the relative absence of incompatible elements on the Juan de Fuca ridge suggests an upper mantle source that has been subjected to repeated melt extraction. That is, many of the incompatible components thought to exist in the primitive mantle were removed prior to the current melting episode.

1.2.2 Cobb–Eickelberg seamount chain

There are several seamount chains west of the JdF ridge on the Pacific plate. Most notable of these is the Cobb–Eickelberg Seamount (CES) (fig. 1.2) chain which trends northwest along a 450 km trace consistent with Pacific plate

movement over a fixed point source (Karsten and Delaney 1989). K–Ar dating reveals progressive aging to the north west along the chain, also indicative of a fixed hot spot source (Morgan 1972). The oldest seamount that is clearly part of the chain was formed 8–9 Mya (Desonie and Duncan 1990). It has been proposed that three more distant seamounts, separated by a gap of 800 km, are part of the chain. If so the age of the hot spot would be at least 26 Mya. However, evidence associating these seamounts with the CES chain is tenuous at best. The mass distribution of volcanoes in the chain has been used to suggest that the production rate of the so–called Cobb hot spot has varied by 20% over the past 10 Mya (Karsten and Delaney 1989).

The distribution and ages of Cobb–Eickelberg seamounts fits the classic hot spot paradigm in which a deeply rooted mantle source remains fixed over millions of years while the lithosphere passes over it. The CES chain is enigmatic however, because geochemical samples do not indicate a deeply rooted source. Sr, Nd and Pb isotope compositions along the chain, which would reveal a primitive mantle source, are indistinguishable from JdF lavas (Desonie and Duncan 1990), and the slight enrichment of incompatible elements is hardly enough to imply a deep mantle source.

A fixed heat source in the shallow mantle can explain the ages, locations and chemistries of the CES seamounts. Few theories, however, can explain a long term stationary heat source without invoking the deep mantle. This puzzle is not resolved here. However to be clear, the term "hot spot" will be used to refer to

the hot, and/or wet, region of the shallow mantle responsible for high magma production. "Hot spot" should not be confused with the concept of a "mantle plume", a term which is often inappropriately swapped with hot spot.

1.2.3 Convergence of hotspot and ridge

The JdF ridge has been migrating northwest for at least the last 10 Mya. During this time the ridge has been closing in on the hot spot at 3 cm/yr, roughly its half spreading rate (Karsten and Delaney 1989). As the two have converged, the ridge and seamount morphology have become superimposed. In the resulting current situation, the effects of hot spot and ridge are difficult to separate and the singular existence of either is called into question.

Delaney *et al.* (1981) observed that spreading in the central portion of the JdF ridge, near the intersection with the CES chain, appeared offset by 15–20 km from the main JdF ridge axis and coincided with a bathymetric high rising above the rest of the ridge. Detailed swath and sidescan sonar mapping during the 1980s revealed a volcanic edifice 20–30 km in diameter, rising 700 meters above the mean elevation of the JdF ridge (fig. 1.3). The discovery of a summit caldera cemented the interpretation of the seamount as a recently active volcano. Active rift zones were imaged extending 50 km north and south from the volcano. The central seamount was given the misnomered title of Axial Volcano – a misnomer because Axial appears to sit 15–20 km *off–axis* to the west.

Our best understanding of the hot spot–ridge interaction at Axial currently comes from petrologic and gravity studies. The ideal chemical discriminant, which would reveal the relative influence of ridge and hot spot at Axial, does not exist because the CES chain lacks chemistry that is sufficiently distinct from the ridge. However, increased MgO contents have shown that melting beneath Axial begins deeper in the mantle and melts more than under the rest of the JdF ridge (Rhodes *et al.* 1990). Hotter mantle temperatures are also implied. A gravity analysis of the Juan de Fuca (Hooft and Detrick 1995) estimated crustal thickening under Axial of 1.5–2 km and mantle temperatures elevated by 30–40°. All of these observations suggest a hot region of excess magma production in the upper mantle. This is what might be expected from the coalescence of two separate melting features – a ridge and a hot spot.

From the outset, Axial was presumed to result from the combined interaction of ridge and hot spot. Though 20 years of research have not altered this interpretation, few new details of this interaction have been explained. Do the rift zones of Axial constitute a bona fide ridge segment of the Juan de Fuca or is Axial an adjacent rifting shield volcano? Is the Axial system better described as a hot spot–perturbed ridge, or a ridge–perturbed hot spot? This work provides some answers to these questions.

1.3 Axial Volcano

1.3.1 Morphology of an undersea rift volcano

A 3 km x 8 km caldera and prominent rift zones are Axial's most obvious structural feature. Caldera walls are roughly 100 meters high though the caldera floor shoals toward the southeast covering any previous expression of the caldera (fig. 1.4). The stress field, as reflected in surface lineations, shows both radial trends and trends aligned with the ridge axis. This feature is consistent with other volcanoes that are subjected to rifting stresses including Mokuoweoweo on Mauna Loa, Hawaii and Krafla in Iceland (Embley *et al.* 1990). The variety of eruption styles at Axial reflects these superimposed stresses. Side–scan sonar has revealed recent lava flows emanating from the caldera walls and from lineations in the middle of the caldera floor. The rift zones have been traced all the way to the summit connecting with lineations along the east and west edges of the caldera. The intersections of the rifts and caldera appear to have hosted much of the recent volcanism. Extrusion from the proximal end of the south rift zone (SRZ) is responsible for burying the southeast caldera wall (Embley *et al.* 1990).

The rift lineations observed in the caldera can be traced to connect with the substantial ridges that extend to the north and south. The rift zones are associated with numerous fresh lava fields along their length. Parallel symmetric ridges along both rift zones suggest they accommodate much of the required spreading across the central JdF ridge (Appelgate 1990, Hammond and Delaney 1985). However, this assessment is qualitative in nature and it is unclear how spreading might be partitioned between the rift zones and the adjacent ridge segments. Volcanic activity on the CoAxial segment in 1993 (Fox 1995) indicates

that Axial's rift zones may not yet be accommodating the full 5–6 cm of spreading per year. Assuming that spreading jumped suddenly to the Axial system, Hammond and Delaney (1985) used the width and volume of the rift zones to estimate Axial's age as 50,000 yr. At the distal ends of the rift zones, small volcanic cones are prevalent as opposed to the linear volcanic fabrics observed nearer the caldera (Appelgate 1990). This suggests that magmas travel to the far ends of the rifts in dikes beneath the surface before finally breaking onto the sea floor in a small area. Morphology suggest that closer to the caldera, linear open rift eruptions are more common.

1.3.2 1998 eruption

Many ideas about Axial's behavior were formed or tested during an eruption in 1998. From eruption detection to rapid response cruises, this was arguably the best observed marine eruption ever. For nearly a decade, monitoring of Axial has benefited from the Navy's SOund SUrveillence System (SOSUS). NOAA has been granted access to a subset of the array allowing the detection of earthquakes down to magnitude mb~1.8. On January 25, 1998, acoustic T–phases from an intense earthquake swarm were detected in the caldera of Axial (fig. 1.5). Over the next 11 days, 8247 events were recorded with peak activity exceeding 120 events/hr (Dziak and Fox, 1999). The caldera remained a locus of activity throughout the eruption. Additional events showed a clear migration away from the caldera and down the rift at a rate of about 0.23 m/s (19.9 km/day). These migrating events were almost certainly the result of a dike injection southward along the rift, propagating until either the magma pressure

was no longer sufficient to fracture rock or until the dike tapped the surface and erupted. This style of rift eruption has been observed along the CoAxial ridge in 1993 (Dziak *et al.* 1995), the east rift of Kilauea in 1983 (Koyanagi *et al.* 1988), and at its type–locality, Krafla, in 1978 (Einarsson and Brandsdottir 1980). The uneven distribution of seismicity along the dike is thought to result from stress differences in the crust. The southern terminus of the swarm coincides with the western normal faults of the Vance segment. Dziak and Fox (1999) propose that the Vance segment acted as a barrier to further propagation of the dike.

T–phase monitoring provides scant information about earthquake depths, but signal rise times have been interpreted to provide relative depth information (Schreiner *et al.* 1995). These rise times suggest that events under the south rift zone occurred near the surface and may indicate eruptions onto the seafloor, while events under the caldera happened at depth in the crust, as if associated with a crustal magma source (Embley *et al.* 1999).

Three earthquakes were large enough to be detected by the Pacific Northwest Seismic Network. Compressional and shear waves were recorded for these events in addition to the T–phases. These three caldera events had motion along sub–vertical faults (Dziak and Fox, 1999). They mark motion along the caldera wall fault system commensurate with the observed caldera collapse (Fox 1999).

During the 1998 eruption magma was extruded along the rise where the south

rift zone meets the caldera. Multibeam surveys before and after the eruption revealed changes in bathymetry associated with fresh lava flows (Embley *et al.* 1999). Based on a bathymetry differencing technique, Embley *et al.* estimate the volume of extruded magma as $0.018-0.076$ km^3. Combined with estimates of the intruded volume (Chadwick et al. 1999), the total volume of magma emplaced during the 1998 eruption is estimated at $0.1-0.2$ km^3. The intruded volume was based on the dike size as estimated from surface deformation and the spatial distribution of seismicity.

1.3.3 Long−term interests at Axial

As part of the rationale for this project, it is worth mentioning a few long−term programs at Axial that will be impacted by the results. Due to its geologic significance and its proximity to the northwestern U.S., Axial and the Juan de Fuca are the site of two separate multi−disciplinary, multi−year investigations.

The NOAA Vents program (Hammond 1990) has supported many of the recent investigations on the JdF. The program's goal is to understand the relationships between volcanic events and the chemistry and distribution of hydrothermal vents and the biologic communities that depend on them. A sub−program within Vents is the New Millennium Observatory. NeMO is addressing these goals by establishing a permanent seafloor observatory at Axial Volcano. This ambitious project is underway with plans to expand site coverage and develop a dedicated on−site remote−controlled vehicle for rapid response to future events.

The NEPTUNE program (Delaney and Chave 2000) is a proposal to cover the JdF plate and ridge with a fiber optic network. This power and communications back bone would provide the framework to allow experiments on a previously unattainable scale.

A better understanding of magma supply at Axial is key to both programs. NeMO's very purpose is to study the effects of the heat produced by the Axial magma source. NEPTUNE, while very broad in scope, plans to address similar issues on a ridge long scale. As Axial is likely to be the most volcanically active portion of the ridge, the distribution of magma deduced in this study has real implications for the program and its experiments.

1.4 Proposed magma chamber

1.4.1 Evidence from the caldera

The single feature most suggestive of a magma chamber under Axial Volcano is its well–defined caldera. There are few plausible mechanisms which can explain a shallow, flat depression bounded by roughly circular fault scarps that is not sediment–filled. Though calderas are typically interpreted as the result of magma removal, they are often associated with the past existence of a magma chamber. Without examining secondary features, there is little connection between a caldera and contemporary magma storage.

Two geochemical trends also suggest that a magma chamber exists beneath

Axial. First, lavas sampled from the caldera show a remarkable degree of homogeneity in major element, trace element and incompatible element ratios as compared to other lavas from the region (See section 5.A) (Perfit *et al.* 1988, Rhodes *et al.* 1990). Since the regional chemistry is know to be fairly heterogeneous (Embley *et al.* 2000), the consistent chemistries in the caldera have been attributed to mixing in a magma chamber. While the actual mechanism by which magma's could be mixed has not been presented, several authors (Perfit 1988, Rhodes et al. 1990) have argued that a mixing volume could smooth the variance from a heterogeneous mantle source.

The second geochemical trend which has been used to argue for the presence of a magma chamber is the MgO content (~7%) indicating a high degree of fractionation. This fractionation has been used to argue that source magma spends an extended period of time cooling in the crust (Perfit 1988). One way to achieve such extra fractionation is to store magma temporarily in a magma chamber.

1.4.2 Evidence from geophysical studies

Gravity and magnetic studies, while less than conclusive, have been consistent with the presence of a melt region beneath the summit. Hildebrand et al. (1990) performed an analysis of the gravity field over the volcano to show that a density anomaly of -0.15 g/cm^3 under the summit is consistent with their sea floor and sea surface gravity measurements.

The magnetic field is complex at Axial. The interpretation of Tivey and Johnson (1990) does not identify a magma chamber *per se*. However, they claim the upper portion of the crust that is magnetized is significantly thinner under the summit. Tivey and Johnson claim this could result either from temperatures above the Curie point or from high temperature hydrothermal alteration in the upper crust. Either process suggests the presence of a significant heat source consistent with a magma chamber.

Numerical models of magma transport have not yet been applied to Axial to estimate the possible melt regime. The best analogues have been conducted for mid−ocean ridges. Morgan and Chen (1993) estimate the depth of a magma lens beneath ridges as a function of spreading rate. They predict a lens at 1−2 km depth under fast spreading ridges and no permanent lens under slow spreading ridges. This model is based on multichannel seismic observations of relfectors under ridges which have been interpreted as magma lenses. According to this model, intermediate ridges should have deeper magma lenses than fast ridges, though they predict an asymptotic spreading rate cut−off below which a steady−state magma chamber is not possible. The JdF is near this cut off with a predicted magma chamber depth below 2.5 km if one exists.

A likely magma lens reflector has been observed under parts of the JdF using multichannel seismic methods. Rohr *et al.* (1988) and Morton *et al.* (1987) identify a seismic reflector under the Endeavour and Cleft segment of the JdF ridge. Neither study determines the reflection polarity which could distinguish a

low velocity from a high velocity reflector. However, the reflectors have similar amplitudes and dimensions as other better constrained magma chambers and it is generally assumed they are true magma lens reflections. Both Rohr *et al.* and Morton *et al.* find indications of a magma lens 2–3 km below seafloor.

However, there is scant evidence that Axial behaves in any way like a normal ridge segment. Indications that Axial is anomalously hot and over–productive are strong. And while the spreading rate of the JdF ridge is 5–6 cm/yr, it is unclear how much of this is currently being accommodated by Axial and how much may still be partitioned to the adjacent segments. These observations, together with the thickened crust and thick extrusives observed in this study, make the relevance of mid–ocean ridge models qualitative at best.

One seismic survey of Axial has been performed. Van Heeswijk (1986) determined the seismic structure beneath the caldera to a depth of ~1.4 km from airgun–to–OBS data. The structure implied high porosity basalts near the surface with porosity decreasing as a function of depth. Compressional wave velocities increased steadily with depth and no evidence of a low velocity zone was detected above 1.4 km.

1.4.3 Evidence from the 1998 eruption

The migration of T–phase seismicity offers compelling evidence for the centralized supply of magma to the south rift zone. Geodetic observations from the 1998 eruption bolster the central magma chamber hypothesis. A pressure

recorder on the caldera floor during the eruption measured a subsidence of over 3 meters synchronous with the onset of caldera earthquakes (Fox 1999). This is a huge deflation by global standards (Dvorak and Dzurisin 1997). Similar subsidence events come from Krafla volcano which is also the site of ridge−hot spot convergence, albeit on a very different scale.

Limited strain measurements during the eruption come from Chadwick et al. (1999). Acoustic extensometers, spanning the north rift zone just outside the caldera, recorded a 4 cm horizontal contraction during the eruption. Mogi point source modeling (Mogi 1958) of this contraction and the caldera deflation can be explained by a point source pressure change located 3.8 km beneath the caldera. If magma extraction from a finite−sized reservoir is the source of the stress change, the point source assumption may over−estimate the depth.

While the evidence presented above strongly suggests a magma chamber beneath Axial, the size, depth distribution and connectivity of magma to regional features has been largely unknown. The ridge−hot spot setting is significant not only because of its local implications on the JdF ridge but also for our understanding of shield volcanoes world wide.

Appelgate, T. B., Jr., Volcanic and structural morphology of the south flank of Axial Volcano, Juan de Fuca Ridge; results from a Sea Marc I side scan sonar survey, *J. Geophys. Res., 95,* 12,765–12,783, 1990.

Benz, H. M., B. A. Chouet, P. B. Dawson, J. C. Lahr, R. A. Page, and J. A. Hole, 3–D P and S wave velocity structure of Redoubt volcano, Alaska, *J. Geophys. Res., 101,* 8111–8128, 1996.

Chadwick,W. W., Jr., R. W. Embley, H. B. Milburn, C. Meinig, and M. Stapp, Evidence for deformation associated with the 1998 eruption of Axial Volcano, Juan de Fuca Ridge, from acoustic extensometer measurements, *Geophys. Res. Lett., 26,* 3441–3444, 1999.

Delaney, J. R., H. P. Johnson, and J. L. Karsten, The Juan de Fuca Ridge–hot spot–propagating rift system; new tectonic, geochemical, and magnetic data, *J. Geophys. Res., 86,* 11,747–11,750, 1981.

Delaney , J. R., and A. D. Chave, NEPTUNE; a fiber–optic "telescope" to inner space, *Oceanus, 42,* 10–11, 2000.

Desonie, D. L., and R. A. Duncan, The Cobb–Eickelberg seamount chain; hotspot volcanism with mid–ocean ridge basalt affinity, *J. Geophys. Res., 95,* 12,697–12,711, 1990.

Dvorak, J. J., and D. Dzurisin, Volcano geodesy; the search for magma reservoirs and the formation of eruptive vents, *Rev. Geophys., 35,* 343–384, 1997.

Dziak, R. P., C. G. Fox, and A. E. Schreiner, The June–July 1993 seismo–acoustic event at CoAxial segment, Juan de Fuca Ridge: Evidence for a lateral dike injection, *Geophys. Res. Lett., 22,* 135–138, 1995.

Dziak, R. P., and C. G. Fox, The January 1998 earthquake swarm at Axial Volcano, Juan de Fuca Ridge; hydroacoustic evidence of seafloor volcanic activity, *Geophys. Res. Lett., 26,* 3429–3432, 1999.

Einarsson, P., and B. Brandsdottir, Seismological evidence for lateral magma intrusion during the July 1978 deflation of the Krafla Volcano in NE Iceland, *J. Geophys., 47,* 160–165. 1980.

Embley, R. W., K. M. Murphy, and C.G. Fox, High–resolution studies of the summit of Axial Volcano, *J. Geophys. Res., 95,* 12,785–12,812, 1990.

Embley, R. W., W. W. Chadwick, Jr., D. A. Clague, and D. Stakes, 1998 eruption of Axial Volcano; multibeam anomalies and seafloor observations, *Geophys. Res. Lett., 26,* 3425–3428, 1999.

Embley, R. W., W. W. Chadwick, Jr., M. R. Perfit, M. C. Smith, & J. R. Delaney, Recent eruptions on the CoAxial segment of the Juan de Fuca Ridge: Implications for mid–ocean ridge accretion processes, *J. Geophys. Res.105,* 16,501–16,525, 2000.

Fox, C. G., Special collection on the June 1993 volcanic eruption on the CoAxial segment, Juan de Fuca Ridge, *Geophys. Res. Lett., 22,* 129–130, 1995.

Fox, C. G., In situ ground deformation measurements from the summit of Axial Volcano during the 1998 volcanic episode, *Geophys. Res. Lett., 26,* 3437–3440, 1999.

Gudmundsson, A., N. Oskarsson, K. Gronvold, K. Saemundsson, O. Sigurdsson, R. Stefansson, S. R. Gislason, P. Einarsson, B. Brandsdottir, G. Larsen, H. Johannesson, and T. Thordarson, The 1991 eruption of Hekla, Iceland, *Bull. Volcanol., 54,* 238–246, 1992.

Hammond, S. R., and J. R. Delaney, Evolution of Axial Volcano, Juan de Fuca Ridge, *Eos. Trans. AGU., 66,* 925, 1985.

Hammond, S. R., The NOAA VENTS program; an interdisciplinary research program focused on determining the oceanic chemical and thermal effects of spreading–center hydrothermal venting, *Eos. Trans. AGU., 71,* 1222, 1990.

Hildebrand, J. A., J. M. Stevenson, P. T. C. Hammer, M. A. Zumberge, R. L. Parker, and C. G. Fox, A seafloor and sea surface gravity survey of Axial Volcano, *J. Geophys. Res., 95,* 12,751–12,763, 1990.

Holden, J. C. and P. R. Vogt, Graphic solutions to problems of plumacy, *Eos. Trans. AGU., 58,* 573–580, 1977.

Hooft, E. E. E., and R.S. Detrick, Relationship between axial morphology, crustal thickness, and mantle temperature along the Juan de Fuca and Gorda Ridges, *J. Geophys. Res., 100,* 22,499–22,508, 1995.

Karsten, J. L., and J. R. Delaney, Hot spot–ridge crest convergence in the Northeast Pacific, *J. Geophys. Res., 94,* 700–712, 1989.

Koyanagi, R. Y., W. R. Tanigawa, and J. S. Nakata, Seismicity associated with the eruption, In *The Puu Oo eruption of Kilauea Volcano, Hawaii; episodes 1 through 20, January 3, 1983, through June 8, 1984,* ed. E. W. Wolf, U.S. Geol. Surv. Paper 1463, 183–235, 1988.

Mogi, K., Relations between the eruptions of various volcanoes and the deformation of the ground surfaces around them, *Bull. Earthquake Res. Inst. Univ. Tokyo, 36,* 99–134, 1958.

Morgan, J.P., and J.Y. Chen, The genesis of oceanic crust; magma injection, hydrothermal circulation, and crustal flow, *J. Geophys. Res., 98,* 6283–6297, 1993.

Morgan, J. P., Plate Motions and Deep Mantle Convection, *Memoir – Geol. Soc. Am. 132,* 7–22, 1972.

Morton, J. L., N. H. Sleep, W. R. Normark, and D. H. Tompkins, Structure of the southern Juan de Fuca Ridge from seismic reflection records, *J. Geophys. Res., 92,* 11,315–11,326, 1987.

Perfit, M. R., A. L. Heatherington, S. Hughes, I. R. Jonasson, and J. M. Franklin, Geochemistry of basalts from Axial Volcano; an example of a well–mixed Axial magma chamber, *Eos. Trans. AGU., 69,* 1467, 1988.

Rhodes, J. M., C. Morgan, & R. A. Liias, Geochemistry of Axial Seamount lavas; magmatic relationship between the Cobb hotspot and the Juan de Fuca Ridge, *J. Geophys. Res. 95,* 12,713–12,733, 1990.

Rohr, K. M. M., B. Milkereit, and J. C. Yorath, Asymmetric deep crustal structure across the Juan de Fuca Ridge, *Geology, 16,* 533–537, 1988.

Ryan, M. P., R. Y. Koyangi and R. S. Fiske, Modeling the three–dimensional structure of macroscopic magma transport systems: application to Kilauea Volcano, Hawaii, *J. Geophys. Res. 96,* 7111–7129, 1981.

Schreiner, A. E., C. G. Fox, and R. P. Dziak, Spectra and magnitudes of T–waves from the 1993 earthquake swarm on the Juan de Fuca, *Geophys. Res. Lett., 22,* 139–142, 1995.

Tivey, M. A., and H. P. Johnson, The magnetic structure of Axial Seamount, Juan de Fuca Ridge, *J. Geophys. Res. 95,* 12,735–12,750, 1990.

Van Heeswijk, M., Shallow Crustal Structure of the caldera of Axial Seamount, Juan de Fuca Ridge, M. S. Thesis, Oregon State University, 1986.

Wilson, D. S., Tectonic history of the Juan de Fuca Ridge over the last 40 million years, *J. Geophys. Res. 93,* 11,863–11,876, 1988.

A

B

C

D

E
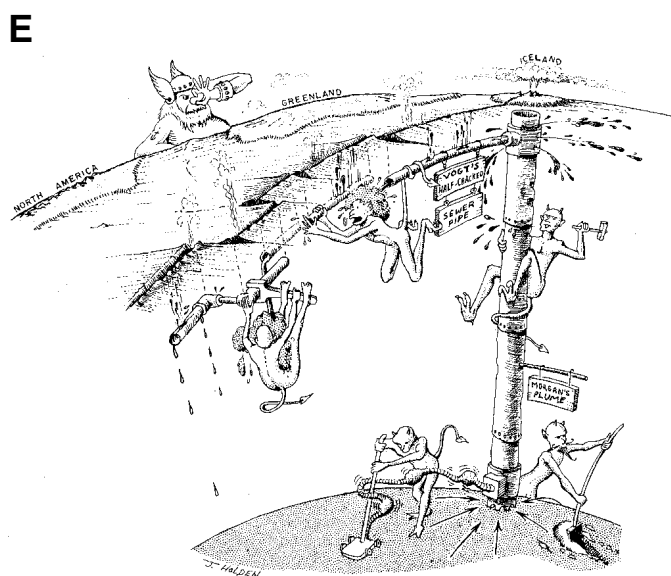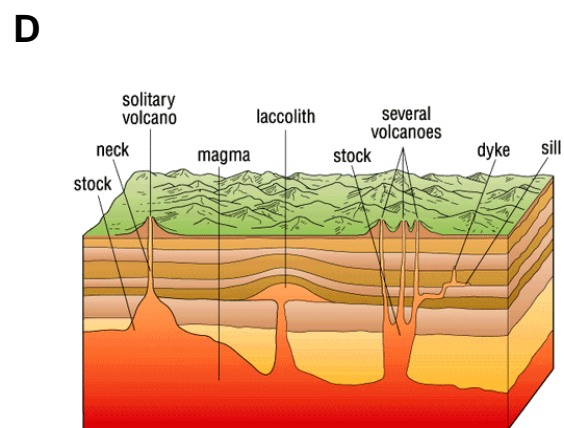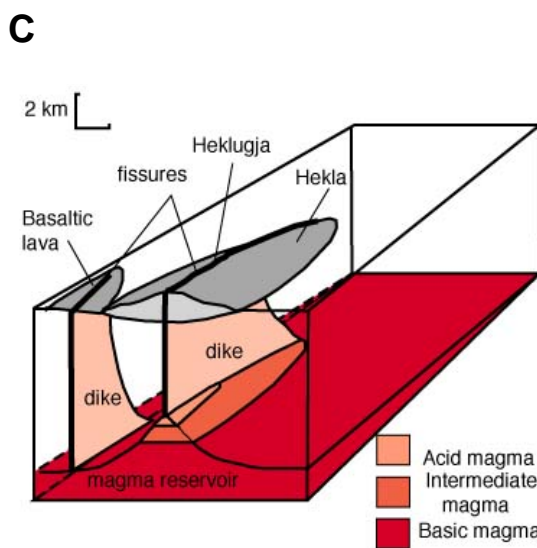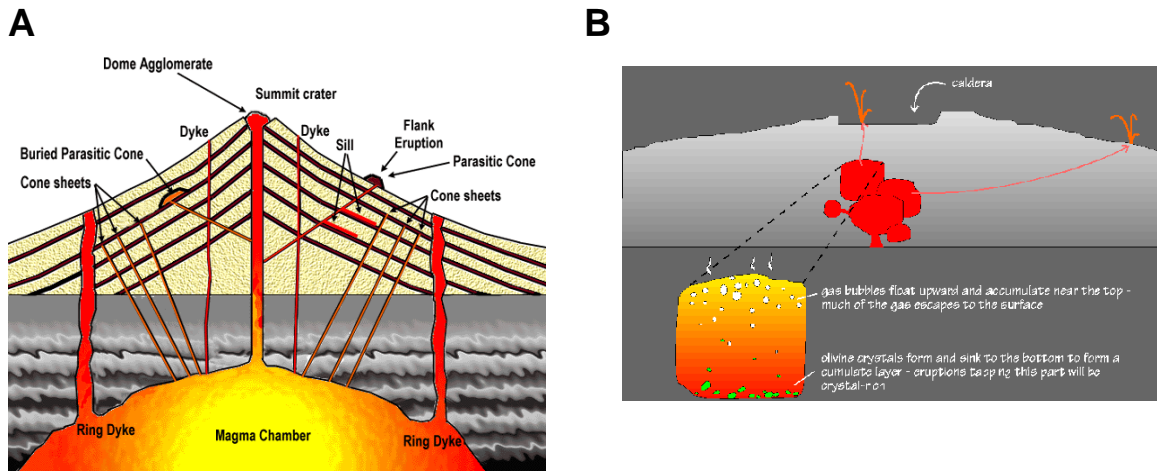
Figure 1.1 A–D Popular depictions of magma storage and transport systems in a range of environments. (see next page for references) **E** Cartoon parody published in EOS (Holden 1977) making light of the numerous, and often hard to reconcile, theories about magma transport in the Earth.

F

flank eruption

shallow magma chamber

lateral intrusion

conduit

magma source region

~2 km
~10 km
approximate scale

G

H

I
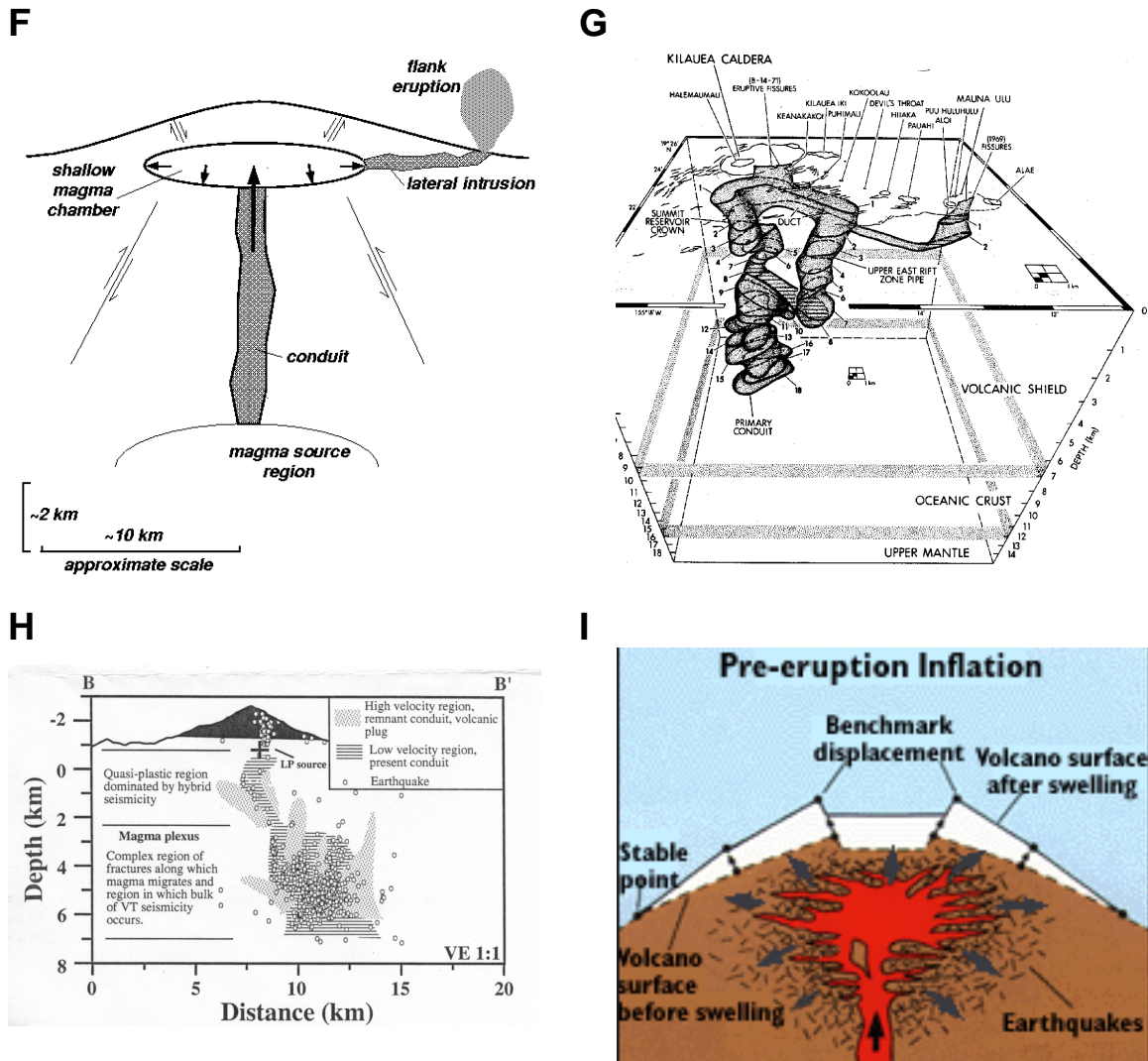
Figure 1.1 F–I More depictions of magma storage and transport in the crust, many drawn from peer–reviewed literature. While different geologic settings are encompassed by these figures, each interpretation includes concepts not present in the others.

Figure 1.1 sources
A Division of Earth Sciences at the University of Derby
B VolcanoWorld project, University of North Dakota
C Adapted from Gudmundsson *et al.* (1992) by VolcanoWorld project, U.N.D.
D The Hutchinson Family Encyclopedia
E Holden and Vogt (1977)
F Department of Earth and Planetary Sciences, Harvard University
G Ryan *et al.* (1981)
H Benz *et al.* (1996)
I United States Geological Survey
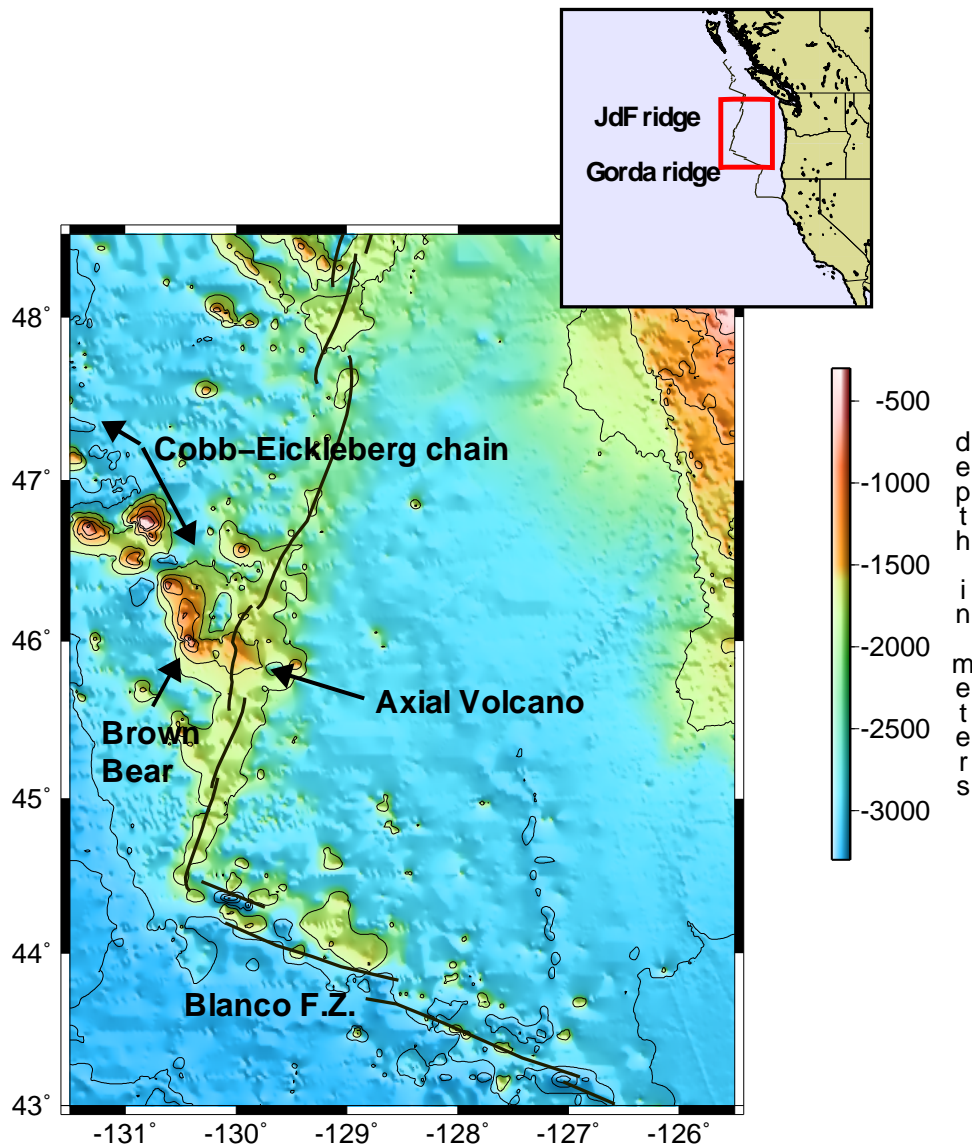
Figure 1.2 Inset: Location of larger map off the Northwest coast of the U.S. The Sovanco fracture zone, Juan de Fuca ridge, Blanco fracture zone and Gorda ridge are drawn respectively from north to south. Main panel: Bathymetry is from the RIDGE Multibeam Synthesis Project (*http://coast.ldeo.columbia.edu*). Contours are drawn at intervals of 500 meters below sea level. Ridge and fracture zone locations, provided by D. Wilson, are superimposed on the bathymetry. The north American Continental shelf is visible in the upper right corner. The Juan de Fuca Ridge trends NNE across the panel. The topographic high in the middle of the ridge is Axial Volcano. The Cobb–Eickelberg seamount chain extends NW from Axial. The shallowest feature just west of Axial is Brown Bear seamount which is thought to be the youngest volcano in the chain preceding Axial. There is no evidence of modern volcanism along the seamount chain except at Axial.
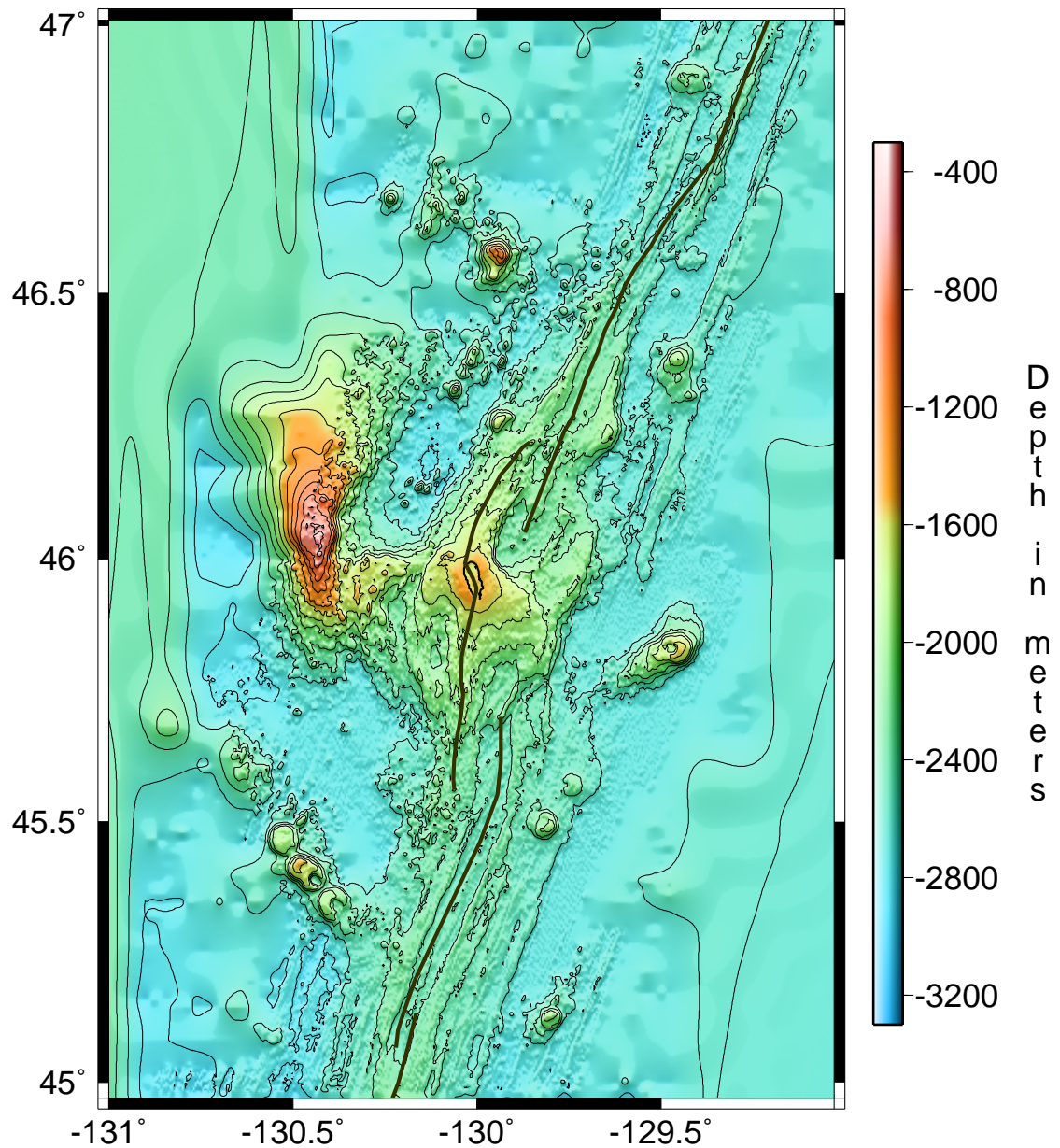
Figure 1.3 High resolution bathymetry of Axial Volcano and its rift zones. Axial caldera is the oval feature at 46°N/130°W. Contours are shown at 200 meter intervals below sea level. The map is roughly 150 km x 220 km. Brown Bear seamount is seen to the west. The north and south rift zones are visible extending in opposite directions away from the caldera. Axial's rift zones (labeled) extend away from the caldera. The Vance segment overlaps the south rift zone, while the CoAxial segment overlaps the north rift zone. Bathymetry is from the RIDGE Multibeam Synthesis Project (*http://coast.ldeo.columbia.edu*)
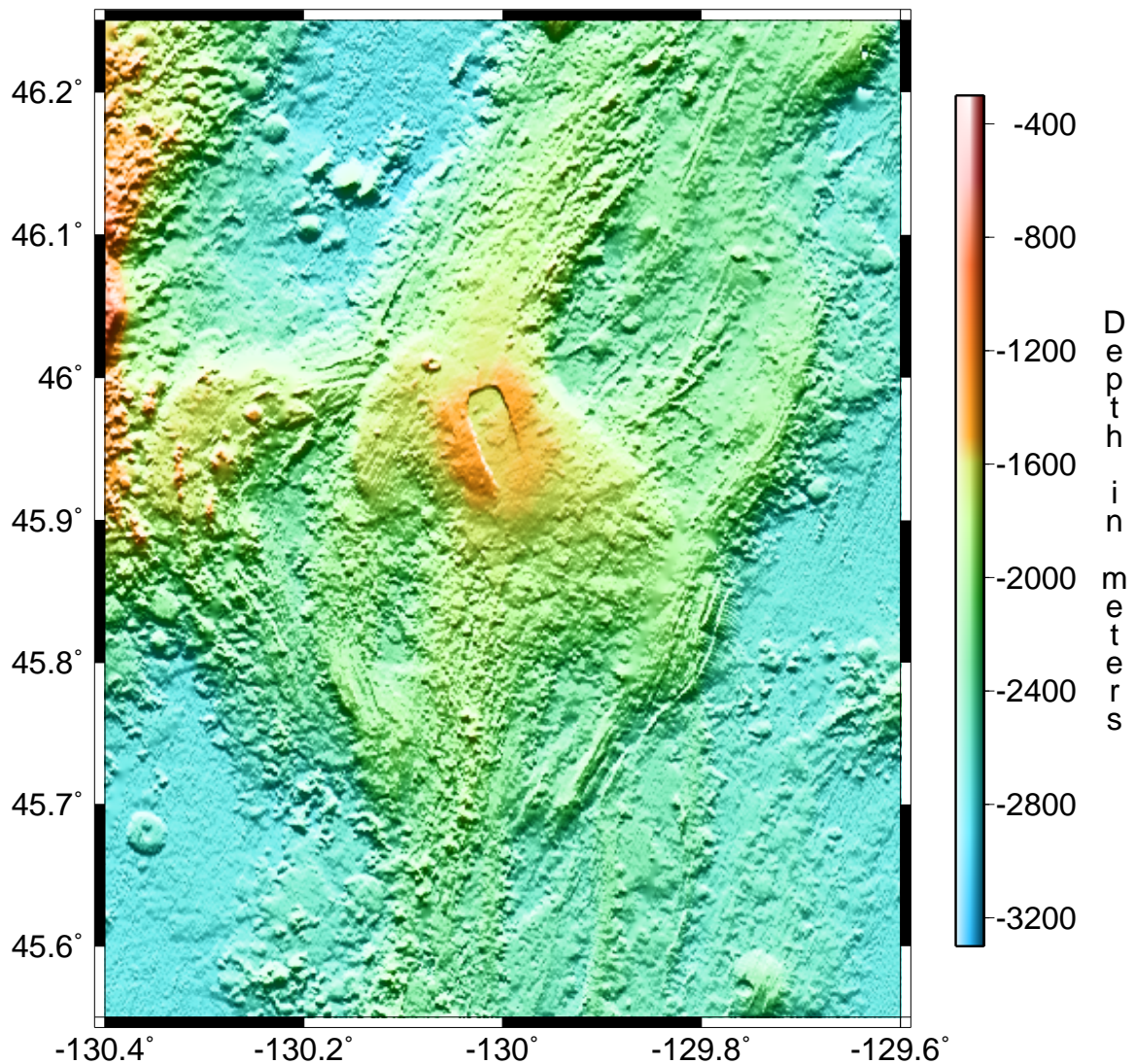
Figure 1.4 High resolution bathymetry of Axial Volcano edifice. Illumination is from the north. The caldera is clear in center of figure. The caldera wall is a prominent feature except along the SE edge of the caldera where any former trace of the wall has been buried by recent eruptive activity. Note ridge lines trending northeast and southwest from the caldera. These are the north and south rift zones, respectively.
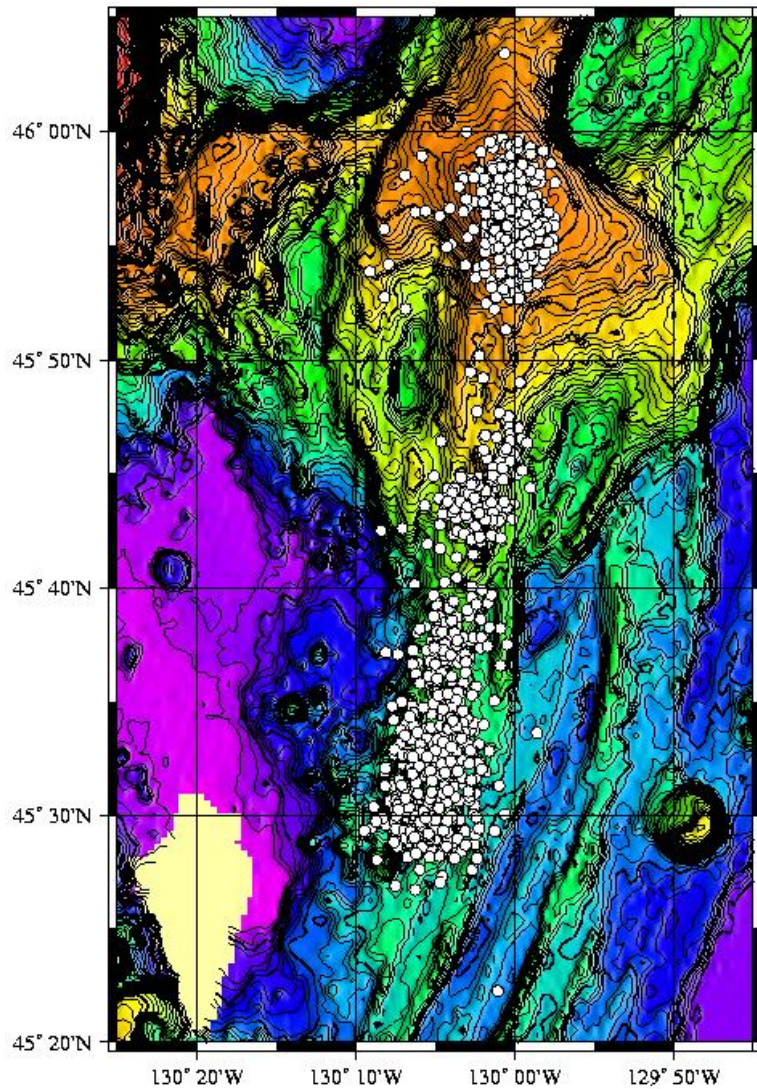
Figure 1.5 The south rift zone with superimposed epicenters from the 1998 eruption (Dziak 1999) (Figure from the NOAA Pacific Marine Environmental Lab). Epicenters were detected acoustically using hydrophones from the Navy's SOund SUrveillence System (SOSUS). The onset of activity on January 28, 1998 occurred in the caldera. The cluster of activity near the top of the figure hides the caldera. Over the next three days, the locus of activity shifted south along the rift zone at an average rate of 0.23 m/s (19.9 km/day) to 45° 30' N. In all, 8247 earthquakes were detected during the 11 day duration of the swarm.

II. Airgun−to−OBS seismic experiment

2.1 Data acquisition

2.1.1 Experiment design and objectives

This project sought to address the crustal mechanics of Axial as a rift volcano, and the effects of the superposition of the Juan de Fuca ridge and the Cobb mantle anomaly. Seismic experiments with closely spaced shots are required for clear phase identification and for seismic tomography. Shallow turning rays to sample the upper crust require seismometers in close proximity to the caldera. However, exploration of Moho and upper mantle phenomena requires large source−receiver offsets. A high signal−to−noise ratio, necessary to detect mantle−refracted energy, mandates at least a two minute interval between shots to allow water column reverbarations to dissipate.

This experiment attempted to provide data for both objectives. Much of the 1226 km of shot lines were concentrated in the vicinity of the volcano (fig. 2.1). The remaining ship time was devoted to 50+ km tracks away from the edifice. Though most of the experiment was shot at intervals of 120 seconds, a small section was shot directly over the caldera at 60 second intervals to provide higher resolution record sections. Because of the generous 7 days devoted to the airgun survey, both objectives were adequately met.

2.1.2 OBS deployment, August 1998

The active source experiment was piggy–backed on a microseismicity study of S. Webb and R. Sohn using the instruments of S. Webb (Sohn *et al.* in preparation). Instruments were deployed during a joint cruise with the Scripps Deep Tow group on the R/V Thomas Thompson. Array geometry was designed to meet the combined objectives of the microseismicity survey and the airgun survey. 18 four–component Ocean Bottom Seismometers (OBS) were deployed, though not all instruments provided data for the active source experiment. In addition, a small 0.5 km x 0.5 km array of five hydrophones was set in the caldera to record hydrothermal cracking events.

Each OBS contains a sensor sphere cantilevered away from the instrument. After settling on the sea floor, the sensor is allowed to fall free away from the package (burnwire release) to improve coupling to the sea floor. The geophones are mounted in motor–driven gimbals that provide 360 degrees of leveling. Power and recording electronics are contained in a pressure case. Anchor weights carry the package to the sea floor. When these are later released by acoustic signals, three glass floats provide flotation back to the surface for recovery. The OBSs recorded vertical and pressure components at 128 Hz throughout the 9 month deployment. During the last 1/3 of the deployment, which included the airgun survey, OBSs recorded 2 horizontal components as well. Timing was performed by Seascan Co. temperature–compensated clocks because of their low–power consumption and fairly constant drift rate.

2.1.3 Airgun survey and OBS recovery, April 1999

In April of 1999, the R/V Ewing arrived at Axial to carry out the airgun survey and to recover the OBSs. The 7 day survey included a total of 5025 shots. The Ewing's full 20–gun array (8670 in^3 / 142 liters) was used throughout. The gun failure rate was low, though on occasion 1 or 2 guns went down for repair. All such irregularities were recorded. The ship's speed was 4 km/hr throughout the survey except for day three when rough seas required a 5 km/hr speed to avoid tangling the gun lines.

Shot positions lie along 22 lines to allow the construction of traditional record sections. To optimize the full 3–D approach however, lines were not shot in a regular grid pattern. Instead, lines were chosen to provide optimum coverage, avoid erratic bathymetric effects, make efficient use of ship time and take advantage of calm seas.

OBS recovery began immediately following the survey. A number of instrument performance problems were discovered at this time. Four instrument packages failed to release their seismometers from the support arm thus compromising the data quality, though the hydrophone channel was unaffected. A larger problem affected some of the OBSs. A small software glitch, introduced during efforts to adapt the instruments to the active source experiment, caused the hard drives to record only the first half of the experiment, missing the airgun survey entirely. In all, seven instruments contained some portion of the active source experiment.

In addition to seismic data, hydrosweep and gravity data were collected continuously throughout the cruise. Much of this area was well covered by previous surveys though new data was acquired west of Brown Bear and east of Son of Brown Bear. To calibrate the hydrosweep mapper, temperature vs. pressure profiles were collected. Though the observed velocity deviations are small (fig. 2.2), they were used to improve seismic raytracing of water waves and crustal phases in addition to improving hydrosweep images.

2.2 Data preparation

2.2.1 Translation to AH format trace files

Six instruments recorded nearly the entire airgun survey. A seventh recorded a few hundred shots far from the instrument. Without close shots, this instrument's timing could not be corrected, so it was not used.

In each of the OBSs four channels of 16–bit data were sent to disk as a single multiplexed stream. A 250 Hz clock inserted a time stamp into this stream roughly every 64 seconds. While this approach is straight forward and minimizes energy consumption on the sea floor, it is preferable to archive seismic traces with location and timing information imbedded in the files. A translation scheme was devised by W. Menke to convert the data into single channel 2 minute AH format trace files. Though this translation generated over 140,000 files, it allowed trace information such as clock corrections and shot time to be stored in trace headers and it facilitated direct access to specific pieces of data.

2.2.2 Archiving

The full set of traces (8.8 Gb) was archived on an automated access mass storage tape device. In each 2 minute trace, there is no more than 15 seconds of useful seismic data. By cropping the appropriate window of data, memory use was trimmed by a factor of 8. This brought the data to a size which could be kept accessible at all times on hard disk.

Efforts to trim and organize the data volume allowed fast access to records and fostered a hands–on approach to interpretation. Traveltime picks were revisited and updated interactively as traveltime features were clarified. In addition, the trim data set could be quickly plotted with up–to–date traveltime interpretations. Combined with a web browser, this allowed rapid perusal of the entire set of traces despite its size.

2.2.3 The MF (Matlab Format) seismic analysis package

The nature of this data created unusual display and manipulation requirements. Automated traveltime picking, sea floor topography corrections and customized plotting scales were among the motivations for creating a new manipulation and display package. The MF (Matlab Format) seismic analysis software unifies seismic processing and display into a single script–driven package. Currently, the MF package includes procedures for filtering, trace scaling, resampling, muting, velocity reduction, static corrections and automatic gain control. A wide array of plotting options permit the user to create customized plots. MF

traveltime picking routines allow automated picking, pick file editing and custom output files. The program suite is written as a fully–documented Matlab toolbox and is available at *http://www.ldeo.columbia.edu/~mwest/software.html.* The Matlab backbone ensures quality export of plots, interactive point–and–click features and easy adaptation to specific needs. The AH format interpreter is adapted with permission from code written by K. Creager and T. McSweeney.

2.3 OBS relocation

2.3.1 Development of raytracing method

Because traveltime tomography is sensitive to predicted traveltime errors, good locations and timing are essential for accurate modeling. OBS studies are particularly susceptible to these errors. During the 45 minute or more descent to the sea floor, currents and the surface area of the OBS package cause the instrument to drift or "glide" away from the precisely–known drop point on the surface. Even a 0.5 knot current could cause an instrument to land on the sea floor 700 meters from its drop point giving rise to an unacceptable error.

Timing errors are more insidious. Unlike their terrestrial counterparts, which can be corrected with GPS updates, the clock in a modern sea floor package must run for many months without adjustment. Add the electronic stress incurred as the clock cools to just above freezing on the sea floor and then returns to ambient temperature on the ship, and accurate timing becomes even more elusive. Several recent advancements in clocks have helped bring this problem

under control. While new clocks are self–corrected for temperature variations, crystal "aging" still limits the accuracy of crystal–based clocks for long deployments. The possible effects of crystal aging can be ignored in this study since the 7 day active source experiment was far too short for significant timing errors to accumulate.

The problem of locating events in space and time is well–studied, most commonly to determine earthquake origins. With an initial estimate of the OBS location, traveltimes can be calculated through the water column. Derivatives of the traveltime misfits with respect to changes in location and timing can then be inverted to find the best–fit OBS location and clock corrections.

$$dt_i = \partial t_i / \partial x_j * dx_j$$

where dt_i is the predicted traveltime error, $\partial t_i / \partial x_j$ is the analytic traveltime derivatives with respect to position and dx_j is the unknown relocation. A lightly damped least squares inversion is suitable to find dx_j. In practice, the OBS relocation problem is easier than earthquake location. The initial location of the OBS is a good estimate, the water velocity structure is measured directly and the raypaths through the water column are relatively straight, unlike their solid rock counterparts. So the linearized Frêchet derivatives, $\partial t_i / \partial x_j$, are typically valid over a large area.

Several OBS relocation procedures exist. Tolstoy (1993) exemplify grid search methods used to get OBS location/clock corrections. Creager and Dorman

(1982) provide a joint inverse approach to estimate instrument position and ship location concurrently. Most approaches however do not raytrace through the water and instead assume straight rays through a homogenous water column. As a result they are subject to the oft−stated "10 kilometer rule" which prevents sources at distances greater than 10 km from being used in the inversion because the straight ray assumption breaks down.

During the recovery cruise multiple water column velocity samples were acquired (fig. 2.2) via a disposable XBT probe. As the probe falls through the water column it simultaneously measures conductivity and temperature. Depth is derived from fall rate while pressure and temperature together provide reliable seismic velocity.

A new OBS relocation code was developed for this project which avoided the straight ray assumption by tracing rays through a 1−D velocity model. Up to five free parameters were included in the inversion: 3−D position, clock offset and clock drift rate. The clock offset is the static time adjustment necessary to correct the clock at the start of the survey. The clock drift, as referred to here, is the drift rate used to calculate small changes in the clock offset during the course of the survey. The complete expression for corrected OBS clock time is

corrected_time =

clock_time + clock_offset + drift_rate * (clock_time − reference_time)

Because the raypaths are nearly straight, the inversion is quite stable for most shot−receiver geometries. As a result, a lightly damped least−squares inversion

is sufficient to acheive reliable results. The OBS relocation is available with documentation at *http://www.ldeo.columbia.edu/~mwest/software.html.*

2.3.2 Stability tests

Noise was added to the data to determine the susceptibility of the solution to poor traveltimes (fig. 2.3). Allowing 0.05 seconds of noise in the traveltimes results in location misfits with $2\sigma < 20$ m. A time error of 0.05 s corresponds to traveltime pick error of a half wavelength at the dominant frequency of 10 Hz, a generous allowance by any measure. The vertical stability of the inversion is poorer because the depth correction trades off with clock offset (fig. 2.3b). To compensate for this, the depth of each OBS was fixed according to the regional bathymetry map which is generally good to < 10 m (Bohnenstiehl, pers. comm.).

An average drift rate for each clock was estimated from total clock error measured between OBS deployment and recovery. Drift was also estimated from the relocation procedure. This inversion for drift parameter was unreliable on all but one clock, however, because little drift occurred over 7 days. The one reliable calculated drift rate (from Victor) of 1.8×10^{-7} (seconds/second) compared favorably with the 9 month averaged drift of 1×10^{-7}. The similarity of these figures allowed us to confidently apply the 9 month averaged drift rates for the other instruments.

2.3.3 Results of relocation

Instrument locations were adjusted by up to 400 meters based on the inversion

results. Adjusting these locations removed as much as 0.2s of traveltime error for shallow crustal phases. Clock corrections were as large as 1.7 seconds. Without such corrections, traveltime comparisons between instruments would have been impossible.

The most notable location adjustment was to instrument Abe. It drifted significantly east of its drop point (fig. 2.1b). Though originally destined for the rim around the caldera, Abe landed on the caldera floor. Sub–caldera features affected wave propagation to Abe and resulted in a unique, if not easily interpretable, seismic record.

Creager, K. C. and L. M. Dorman, Location of instruments on the sea floor by joint adjustment of instrument and ship positions., *J. Geophys. Res., 87,* 8379–8388, 1982.

Tolstoy, M., A. J. Harding, and J. A. Orcutt, Crustal thickness on the Mid–Atlantic Ridge: Bull's–eye gravity anomalies and focused accretion, *Science, 262,* 726–729.

Webb, S.C., T.K. Deaton, and J. C. Lemire, A broadband ocean bottom seismometer system based on a 1 Hz natural period geophone, *Bull. Seismol. Soc. Am.*, 2001.
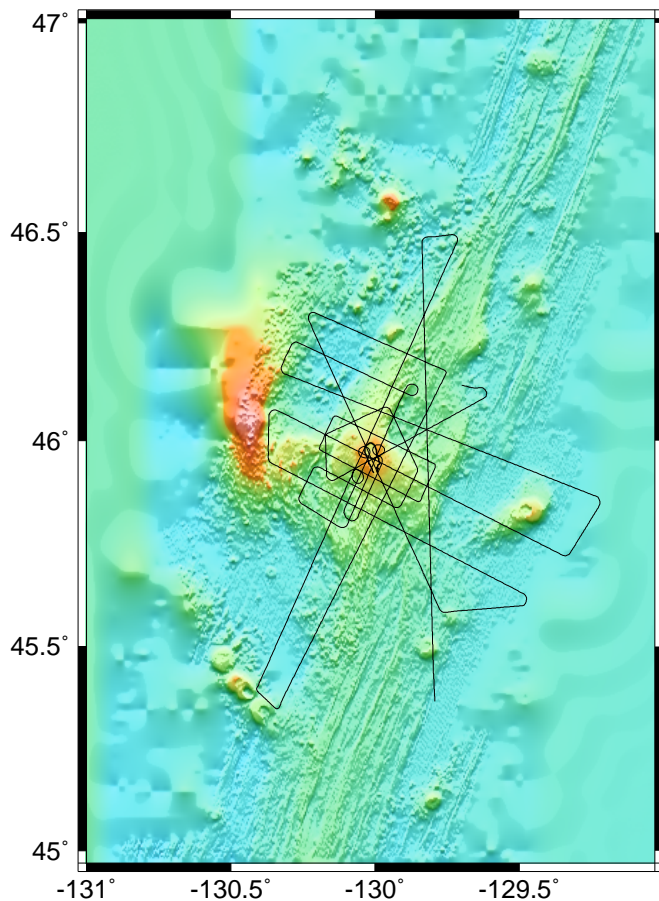
Figure 2.1a Ship tracks of R/V Ewing during airgun survey beginning southeast of Axial. 5025 airgun shots are spread over the 1226 km of tracks. The survey geometry was designed to collect closely spaced samples near the volcano as well as long offset lines to collect deep crust and upper mantle data along the ridge crest and on the adjacent plains.

Figure 2.1b Airgun survey tracks near the caldera. Positions of six Ocean Bottom Seismometers (OBS) are labeled. Three instruments are clustered around the caldera while three others are on the flanks of the volcano.

depth in meters
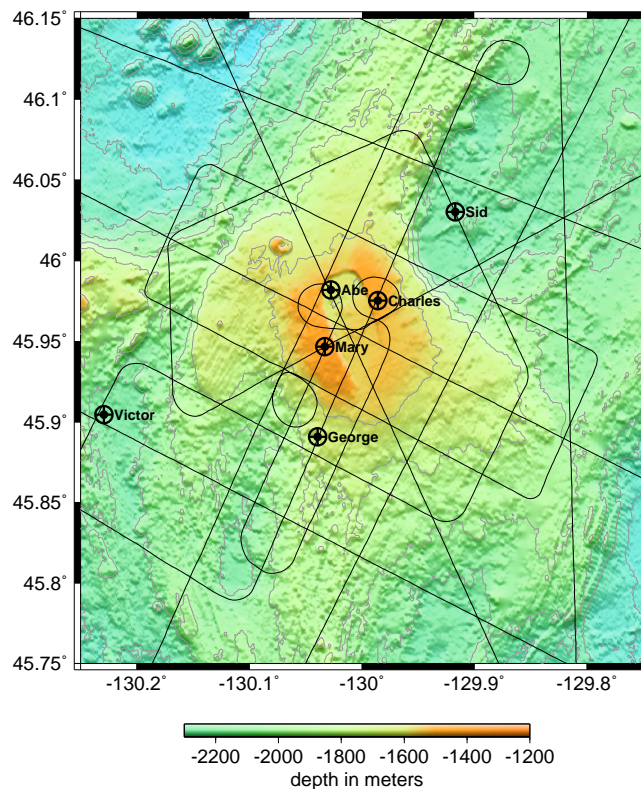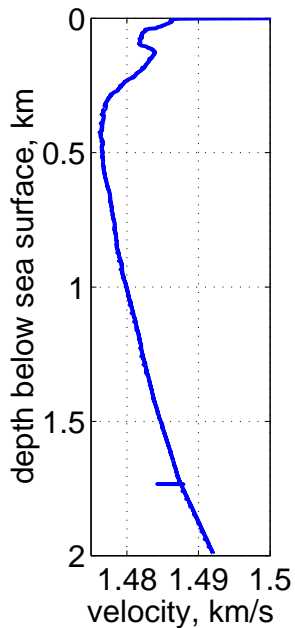
Figure 2.2a Sample water column velocity as a function of depth. This measurement was taken during the airgun survey cruise for the purpose of calibrating the hydrosweep mapping system. It is also used for water wave raytracing in the OBS relocation inversion. The data comes from a small pressure and temperature probe. Depth is determined from the pressure. Temperature and pressure together are used to estimate the acoustic velocity profile.
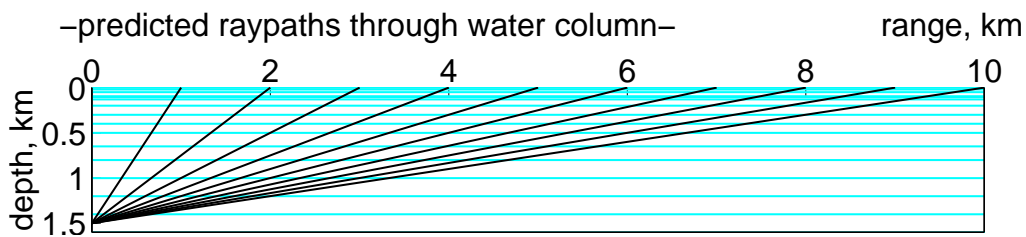
Figure 2.2b True scale raypaths through the water velocity model. Rays are nearly straight due to the minimal velocity variation. The straight rays make the linear relocation inversion assumption valid over short distances.
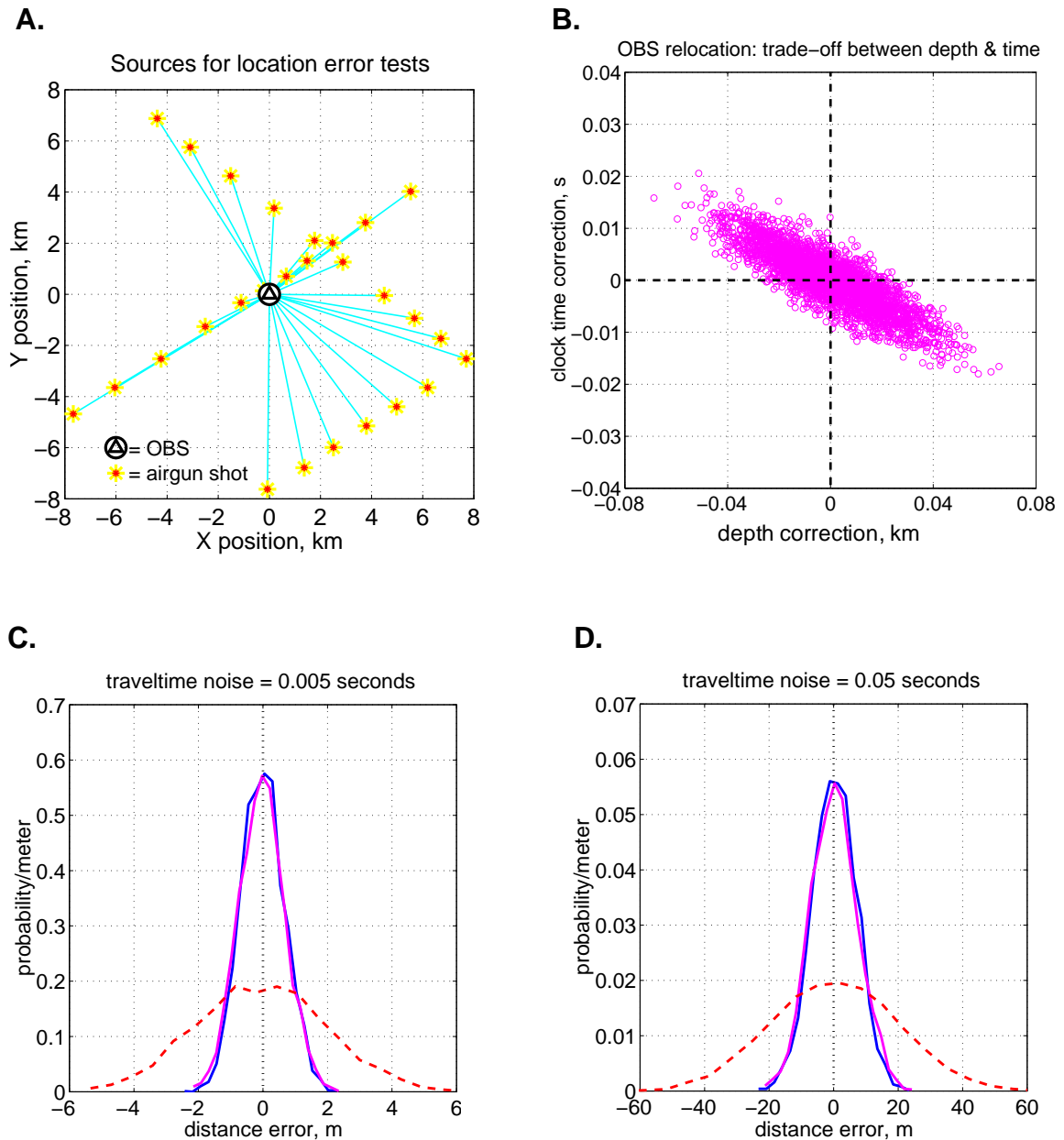
Figure 2.3 Sample resolution test of OBS relocation procedure. **A.** Typical geometry of shots used in instrument location. Most instruments in this study have more complete coverage than this example so these results represent a worst case scenerio. **B.** Trade off between clock correction and vertical position. Since rays reach the instrument only from the top, the predicted depth trades off with time. Because of this possible error we fix the vertical position of the instruments to < 10 meters using independent bathymetry measurements. **C.** Predicted relocation error for traveltimes with 0.005 s of random noise. Solid lines are horizontal error, dashed line is depth error. **D.** Predicted relocation error for traveltimes with 0.05 s of random noise. 0.05 s is roughly equivalent to a half wavelength with a dominant frequency of 10 Hz. We estimate our traveltime errors as much less than this value.

III. The velocity structure of Axial Volcano

3.1 Traveltime identification

3.1.1 Phase identification

This experiment was based on several seismic phases including crustal Pg phases, delayed phases which show interaction with crustal low velocity zones, Moho reflected PmP and mantle refracted Pn (fig. 3.1). 250 meter shot spacing provided sufficiently dense records to avoid spatial aliasing, though aliasing near the triplication would have been a problem at a lower trace density (fig. 3.2).

The first phase identifications were carried out on common receiver gathers where shots and OBSs lay along a straight line. Apparent velocities and relative amplitudes, when compared against previous experiments, provide grounds for positively identifying seismic phases (fig. 3.3). The Pg/PmP/Pn triplication has been reliably observed in both thick crust oceanic plateau settings (example, Menke *et al.* 1998) and along normal sections of ocean ridge (e.g. Tolstoy *et al.* 1993, Magde *et al.* 2000). The convergence of phases is marked by large amplitudes and an increase in apparent velocity to > 8 km/s. A more subtle marker is the "Pn gap" – a short interruption of Pg just before Pn emerges as the first arrival. This gap, resulting from deconstructive interference of Pg and Pn, is often visible even when Pn is too weak to be identified (fig. 3.4).

1−D traveltime modeling is useful to test the geologic plausibility of phase identifications. Figure 3.5 shows a set of traveltimes modeled using a combination of forward and inverse approaches. The implied crustal structure agrees well with previous knowledge of oceanic crust. Though useful for confirming phase identifications such modeling is limited by the 1−D assumption.

3.1.2 Automated traveltime picking

Automatic picking routines are a common way to cull traveltime information from a large volume of data. These programs comb through the data and assign traveltimes based on a number of sophisticated wave analysis techniques. Such approaches are often used when picking only first arrivals, or when working with well−studied uniform datasets such as global teleseisms. But interesting seismic data is often variable and difficult to describe *a priori*. The severe ray bending and diffraction caused by large velocity anomalies under volcanoes, as well as attenuation effects, make automated picking risky. In addition, by reducing the interaction of the seismologist and the data, it becomes much harder to support model results with direct observations. For these reason, an fully automated picking scheme was not employed.

A novel semi−automated routine was used however to speed up the picking process (fig. 3.6). After selecting a small number of control points, each trace is cross−correlated with the control trace on either side to determine the time lag which yields the best correlation. The time lags for the correlations on either side are weighted as a function of the distance between the shots to determine the

best pick:

$$t = t_L * (\mathbf{X}_R - \mathbf{X}) / (\mathbf{X}_R - \mathbf{X}_L) \quad + \quad t_R * (\mathbf{X} - \mathbf{X}_L) / (\mathbf{X}_R - \mathbf{X}_L)$$

where t_L and $\mathbf{X}_L$ are the traveltime and shot position of the control trace to the *left* of the trace being examined. t_R and $\mathbf{X}_R$ describe the trace to the right. This weighting strategy allows the procedure to accurately pick traveltimes through changes in the first arrival waveform. This routine is publicly available as part of the MF seismic processing program suite (sec. 2.2.3).

The phase picking process happens in real time so the user can further revise the picks as needed. The semi–automated approach ensures that each pick agrees with the user's interpretation of the data. Traveltime information is then stored according to the phase designation assigned by the user.

3.1.3 Multiple–pass picking approach

During the first pass of traveltime identification, many parts of the data are left unassigned because the phases are poorly understood. Additions to the traveltime data are based on improved understanding of the velocity structure from preliminary modeling, and on confidence gained by observing trends repeated throughout the dataset. The best results are obtained from an iterative approach in which traveltimes are repeatedly updated based on the results of interim 3–D modeling. The iterative approach is continued until the data interpretation and the model results converge to a self–consistent geologically–plausible result.

3.2 Effect of variable bathymetry

3.2.1 Errors introduced by topography

The primary advantage of an airgun seismic source over an explosive source on the sea floor is one of economy. The sacrifice of an airgun survey is the waveform complications introduced by the water column and a high impedance contrast at the sea floor. The effects are a combination of traveltime offsets and wavefield diffractions near irregular sea floor features.

The crudest remedy is to apply a static correction to each trace based on the bathymetry under the shot. This often fails because the ray entry point is likely not under the shot. A common strategy to "correct" for bathymetry is to search each shot point for the shortest path to the sea floor. After an approximate correction has been applied to the traveltime, the data can then be treated as if the sea floor were flat. This approach has been used by many authors (e.g. Tolstoy *et al.* 1993, Sohn *et al.* 1997) and is well suited to 2–D dimensional studies, as it traces the water wave in 3–D before applying 2–D assumptions for the rest of the ray path.

We avoid sea floor corrections by explicitly including bathymetry in the raytracing. Though this is the most accurate approach, it demands vigilant phase picking to distinguish sea floor effects from lateral variations in velocity structure.

3.2.2 Modeling technique

To understand the role of bathymetry, a 2.5–D modeling scheme is used to estimate the effects of an arbitrary sea floor on an incident plane wave. Both the traveltime effects and wave front healing that occurs after crossing an irregular boundary are considered.

First, the traveltime to the sea floor from an arbitrary datum is calculated using an average rock velocity (fig. 3.7). Each point along the sea floor is treated as a Huygen's point source. As this spherical wavefront expands, 3–D spreading diminishes the amplitude until it contacts the receiver surface. At a given point on the sea surface, the observed wave field is a summation of the contributions from a wide range of sea floor sources. A typical waveform is drawn from the data to provide a realistic input signal. The modeled traces have the same 250 meter spacing as the real data. Figure 3.8 demonstrates the effects of different wavelength ridges on the sea floor. In addition to aiding the traveltime picking, this information was used to determine how accurately the sea floor needed to be incorporated into the 3–D model.

3.2.3 Implications for traveltime picks

Figure 3.9 is a summary of the scattering effects expected from sea floor irregularities. Over long wavelength sea floor features, traveltimes are shifted and waveforms are coherent making them easy to observe. Over shorter features, the wavefront loses coherency and aliasing becomes a problem. Real data similar to this would be difficult to pick on a noisy record section. The shortest wavelength features are invisible in this deep water.

This inability to resolve certain sea floor features introduces error. However, it also demonstrates that sufficiently small features can be left out of the ray tracing model. Though geometry in the 3rd dimension affects the results, the 2.5−D assumption is valid over much of the terrain since features are often ridges and fault scarps.

3.3 Creation of starting model

3.3.1 Bathymetry−draped 1−D model

Success of the tomographic method relies on a good starting model which includes any *a priori* information. A composite 1−D model was assembled from prior studies (Sohn et al. 1997, Van Heeswijk 1986) and the preliminary 1−D models discussed in section 3.1. Since many processes including hydrothermal circulation, extrusive layering and cooling are , to first order, a function of depth below sea floor (lithostatic pressure), a bathymetry−draped model was geologically appropriate. The composite 1−D model was draped on the regional bathymetry such that isovelocity surfaces are "parallel" to the sea floor.

3.3.2 Optimizing 1−D model

An accurate starting model is important because the raypaths used in the tomographic inversion depend on the initial structure. It is also reference to this base−model that defines what velocity features are "anomalous".

To optimize the pseudo–1–D model, inversions were performed using 3–D raytracing but only allowing the velocity structure to vary in 1–D. Observations in the raw data suggested significant disturbances in the caldera region. To keep these from dominating the inversion, rays which passed near the caldera were not included in the 1–D inversions. Multiple iterations using these constraints converged quickly to the structure in figure 3.10. Section 3.4 provides details of the inversion process. No Moho appears in the model because the preliminary 1–D approach does not consider PmP or Pn phases. To avoid tainting crustal features with Moho influences, no traveltime information from ranges beyond the PmP triplication (~42 km) are used in this first stage.

The water velocity, based on xbt result (figure 2.2a) and fixed in the inversion, has a constant velocity of 1.49 km/s. Velocities increase rapidly in the top 2 km below sea floor. This trend is ubiquitous in ocean crust and similar to that found by Heeswijk (1986) in the Axial caldera. It reflects the progressive compaction of extruded basalts and the transition to sheeted dikes. There is a jump in velocity near 2 km. This feature, also observed widely in marine seismic data, is thought to reflect the boundary between extrusive basaltic volcanics and intrusive gabbros. Velocity gradients in the lower crust are small. This low gradient is manifest in raw data as a flat low amplitude Pg arrival before the cross over.

3.4 3–D velocity structure

3.4.1 Why tomography?

Cliché as it sounds, tomography is only as good as the data on which it is based. Features in the subsurface velocity structure are revealed by exploiting discrepancies in the traveltime predictions. Significant model perturbations require significant traveltime discrepancies that ought to be observable in the raw data. If few features exist in the traveltime curves, complex tomographic results should be viewed warily.

Significant features throughout the Axial airgun data, such as traveltime delays, triplications, shadow zones, secondary arrivals and amplitude variations suggested early on that this data set was a good candidate for tomographic inversion. Consider for example, a fan shot crossing the caldera (fig. 3.11). This feature is an observation *in the data*. Tomography is better constrained than the simple waveform modeling shown. However, it is these simple observations in the data that give credence to the inversion results and suggest that tomography is a viable tool for this data set. Whenever possible here, tomographic results are backed up by raw data observations.

3.4.2 Tomographic inversion for upper and lower crustal structure

Raytracing and traveltime prediction are accomplished with an efficient 3–D ray– theoretical code written by W. Menke. Velocities are specified on a warped grid. This grid model is prepared for raytracing by splitting each warped parallelepiped into two prisms, each of which is subsequently split into three tetrahedra. The velocity within each of the resulting six tetrahedra is a linear combination of the four corners. In the resulting constant gradient velocity field, raypaths are arcs of

circles. This allows the eikonal equation to be solved analytically through each tetrahedron. This approach, which eliminates integration along a raypath, is fast.

Coarse resolution velocity grids were used to start. More detailed grids were developed to provide finer resolution in areas of high ray density. The final grid geometry was selected to balance several criteria:

- to provide a tight grid in regions of high ray density
- to represent sea floor topography with adequate resolution
- to provide a smooth grid conducive to raytracing

Evaluating these criteria for coarse velocity grids provided a basis for the next generation of models.

The final model grid was plaid in the horizontal dimensions (nodes lie on parallel but irregularly spaced planes), sheared vertically to follow the bathymetry (fig. 3.12). Horizontal node spacing is 2x2 km near the caldera, and increases away from the volcano. Vertical node spacing increases from 0.4 km in the upper and mid crust to 1.5 km in the lower crust.

A suite of model visualization and manipulation programs was written to accompany the raytracer of W. Menke. The package includes tools for viewing velocity models, raypaths and traveltimes in 2 and 3 dimensions (fig. 3.12–14, 4.4). Interactive viewing programs permit the user to toggle between depth slices

while exploring model space and rotate 3–D isovelocity plots (fig. 4.5). Model building tools aid in the creation of velocity models and inversion control files. Plots are exportable and programs are easily adapted for specific uses in the Matlab environment. The full program suite can be obtained at *http://www.ldeo.columbia.edu/~mwest/software.html*.

The inversion is parameterized using the same grid as the velocity model. Each node can vary by itself, together with a group of nodes, or not at all. The grouping of nodes can weight certain size features or reflect prior knowledge of the structure. Preliminary inversions of the data used a coarse parameterization to highlight regional variations. However, final inversion results allowed each node to vary individually.

An initial set of rays is shot spanning all take off angles and azimuths. This provides a starting place to locate actual source–receiver pairs. By pre–shooting the model all ray paths to a given receiver are identified. This allows multiple phases to be calculated.

Once traveltimes have been calculated, frechêt kernels are derived from stored ray information by computing the traveltime derivatives with respect to velocity at each node or group of nodes. A damped least squares inversion is used to update the velocity model to minimize the traveltime misfit.

$$T^{pre} - T^{obs} = G * (V^{new} - V^{orig.})$$

$$dT = G * dV$$

$$dV = (G^T * G + \varepsilon^2 I)^{-1} * G^T * dT$$

$$\text{where } G_{ij} = \partial T_i / \partial V_j$$

This linearized solution ignores the dependence of the inversion kernels, G, on the velocities, V, being sought from the inversion. Alterations in the velocity structure cause the raypaths to shift positions. To minimize instability, only small changes are permitted in the modeled velocity structure before calculating new ray paths. Iterating the forward and inverse steps allows the raypaths to shift as the velocity structure evolves. Model updates within each iteration are kept small by applying a damping factor to the inversion and/or by applying only a portion of the suggested model change. Damping also drives changes in unconstrained portions of the model to zero, keeping poorly sampled areas of the model from adding unwarranted complexity to the results. A damping factor of

$\varepsilon^2 = 0.1* \parallel G^T G \parallel_\infty$ was used to achieve the final model.

16,400 rays are used in the inversion for crustal structure. Phases which illuminate the Moho and upper mantle are dealt with separately after crustal features are determined. Pn emerges as the first arriving phase at large range. To avoid mantle complications only rays with source–receiver distances less than the cross over distance were used in the inversion.

Predicted traveltimes from the draped 1–D model deviate from real data with an rms error of 0.18 s. Much of this variation comes from a small percentage of rays which pass under the caldera and are delayed by 0.5 seconds or more. Three

iterations of the inversion procedure reduce this to 0.089 s, an improvement of 51%. Subsequent iterations do little to improve the model fit though they add complexity to the model as measured by the variance of the difference between the current model and the 1−D starting model. Tracing rays also becomes more difficult in complex models. Based on these factors, the iterative process was terminated when the traveltime residuals stop improving significantly. An over−simplified model is preferred rather than risking the introduction of structural details that do not exist. The basic geometry of the model is roughly consistent through the iterative process, though the amplitude of the anomalies evolves. The resolved section of the final model for crustal velocity structure is shown in figures 3.13 and 3.14.

A simple though often neglected step in tomography is to closely examine the predicted data against the real data. A qualitative feel for the error distribution is difficult to obtain without examining the observed and predicted data together. By updating the web−browsable record sections with the latest predicted traveltimes, the distribution of error could be assessed visually as well. This type of approach offers a more intuitive feel for the data than statistics alone can provide.

3.4.3 Resolution tests

Another way to asses the power and limitations of the inversion process is through resolution tests. By testing the tomographic process with a hypothetical but fully known model, we can assess how well the tomographic process

performs geographically. Raytracing is carried out on a synthetic model. These traveltimes are then inverted using the same starting model and inversion parameters as in the real inversion. The results can be compared directly with the starting model to assess the resolution of the procedure. Figure 4.3 shows the results of a resolution test using a 3 x 3 x 3 grid of velocity anomalies in the central portion of the model where we expect to have resolving power. As in most tomography, the shallowest portion of the model is poorly constrained. A few kilometers under the sea floor, near the depth of the caldera low velocity zone, the inversion does a fair job of returning the input model geometry. Deeper in the crust, the overall geometry of the anomalies is captured though they are smeared over a larger area. Though the ray coverage at depth is still good, azimuthally it is not as well distributed as at shallower depths.

Magde, L. S., A. H. Barclay, D. R. Toomey, R. S. Detrick, J. A. Collins, Crustal magma plumbing within a segment of the Mid–Atlantic Ridge, 35° N., *Earth Planet. Sci. Lett., 175,* 55–67, 2000.

Menke, W., M. West, B. Brandsdottir, and D. Sparks, Compressional and shear velocity structure of the lithosphere in Northern Ireland, *Bull. Seis. Soc. Am., 88,* 1561–1571, 1998.

Sohn, R. A., S. C. Webb, J. A. Hildebrand, and B. D. Cornuelle, Three–dimensional tomographic velocity structure of upper crust, CoAxial segment, Juan de Fuca Ridge; implications for on–axis evolution and hydrothermal circulation, *J. Geophys. Res., 102,* 17,679–17,695, 1997.

Tolstoy, M., A. J. Harding, and J. A. Orcutt, Crustal thickness on the Mid–Atlantic Ridge: Bull's–eye gravity anomalies and focused accretion, *Science, 262,* 726–729.

Van Heeswijk, M., Shallow Crustal Structure of the caldera of Axial Seamount, Juan de Fuca Ridge, M. S. Thesis, Oregon State University, 1986.
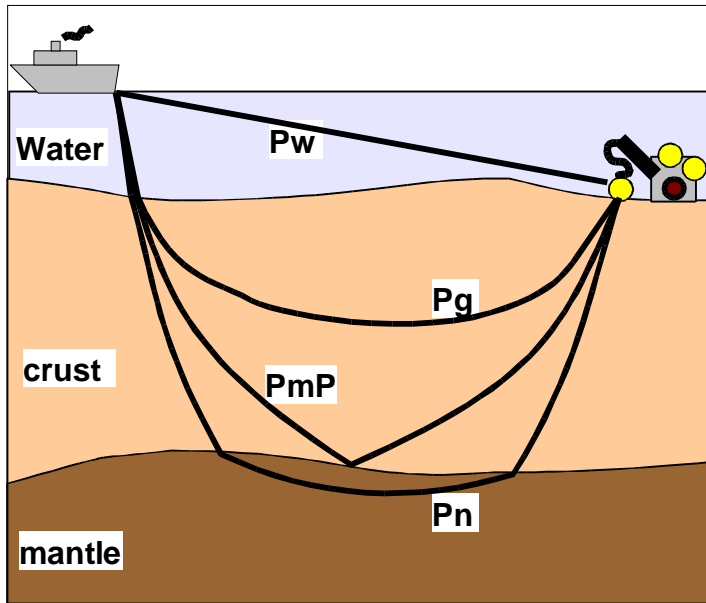
Figure 3.1 Principle ray paths used in this study. The direct water wave arrival, Pw, is used to relocate instrument packages on sea floor and determine clock corrections. Pg and variations of it are used in the traveltime tomography. The Moho reflection, PmP is used to determine crustal thickness and Pn is used to constrain upper mantle properties.
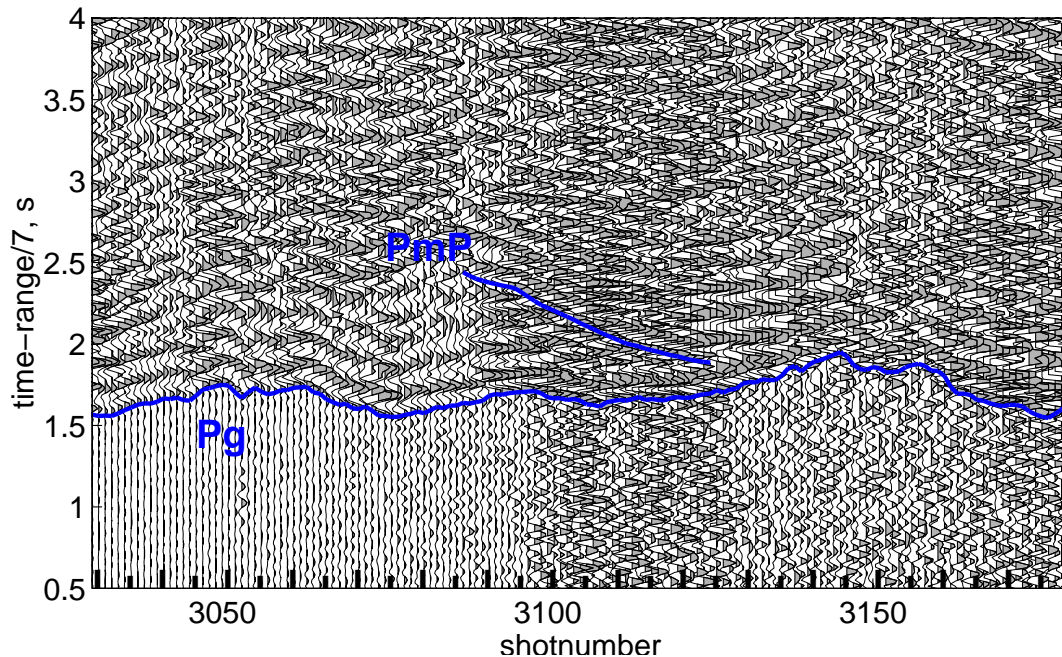
Figure 3.2 Record section showing good PmP phase. Either Pg or PmP (depending on velocity–reduced time scale) would be aliased and possibly undetected if the shot spacing was increased. Shots here, and throughout most of this experiment, are spaced at ~250 meters unless otherwise stated.
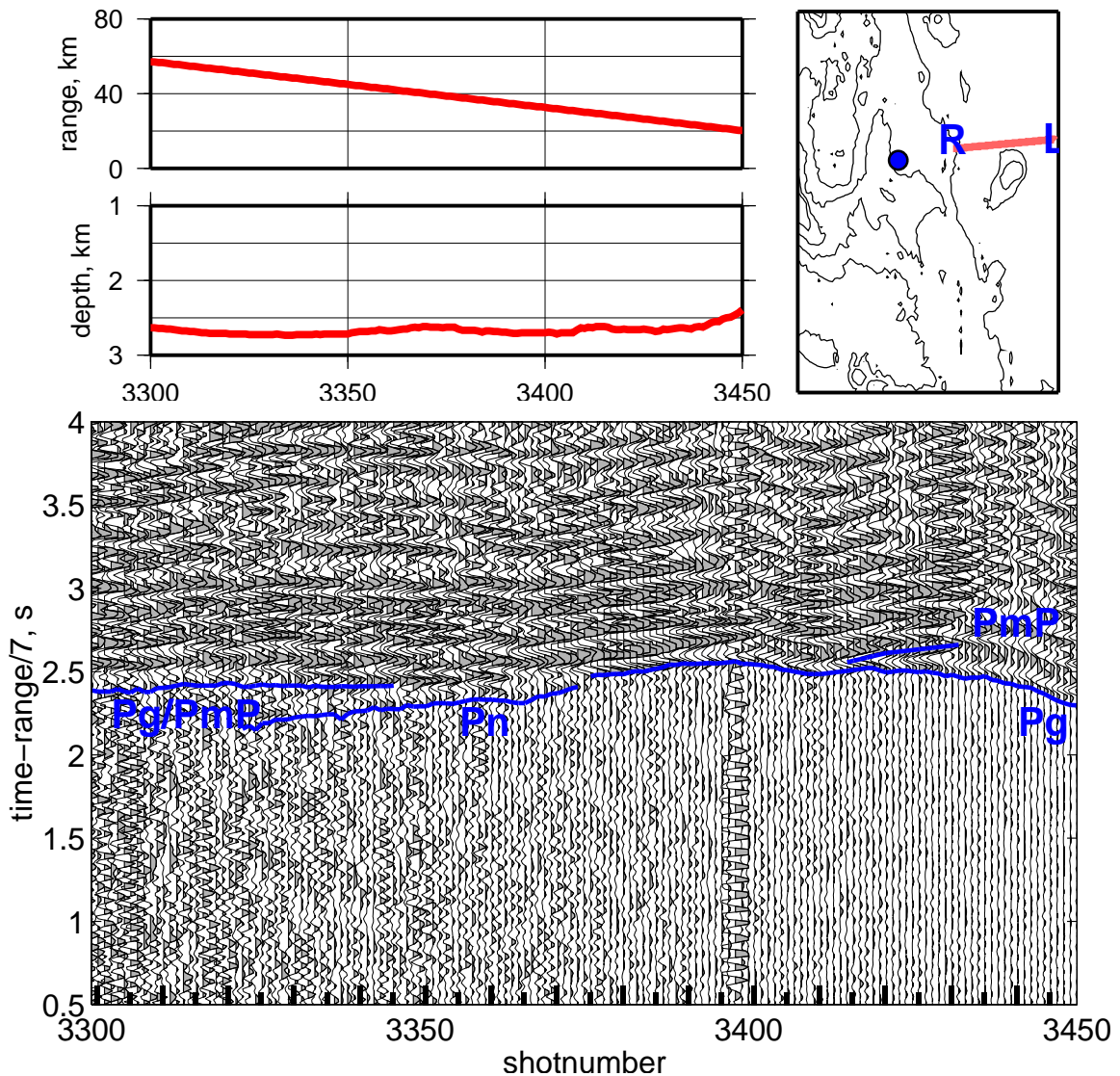
Figure 3.3 Off–axis record unperturbed by low velocity zones. Pg is observed before the Pn cross over (to the right). A short PmP phase is visible behind Pg. The separation between phases is unclear for a short stretch before Pn emerges as the first arrival with a steeper apparent velocity. Note the large amplitude arrivals where phases interfere near the cross over.

Note on seismic displays: *This, and all other records shown, have had a 2 Hz high pass filter applied to remove long–period microseism noise. A low pass filter of 12–16 Hz (16 Hz here) is used to minimize the ambient water column noise. Traces are scaled as a function of range². Horizontal axis is shot number. Shot spacing is typically 250 meters. Vertical axis is reduced time. Vertical lines mark ship turns. Subplots show supplemental information to put record in context. Range is the horizontal shot–receiver distance. Depth plot shows the bathymetry under the shot point. And the map shows shot and OBS locations. R and L mark the right and left side of the trace display. While no depth is included explicitly in modeling, a bathymetry correction is applied to some records for display purposes.*
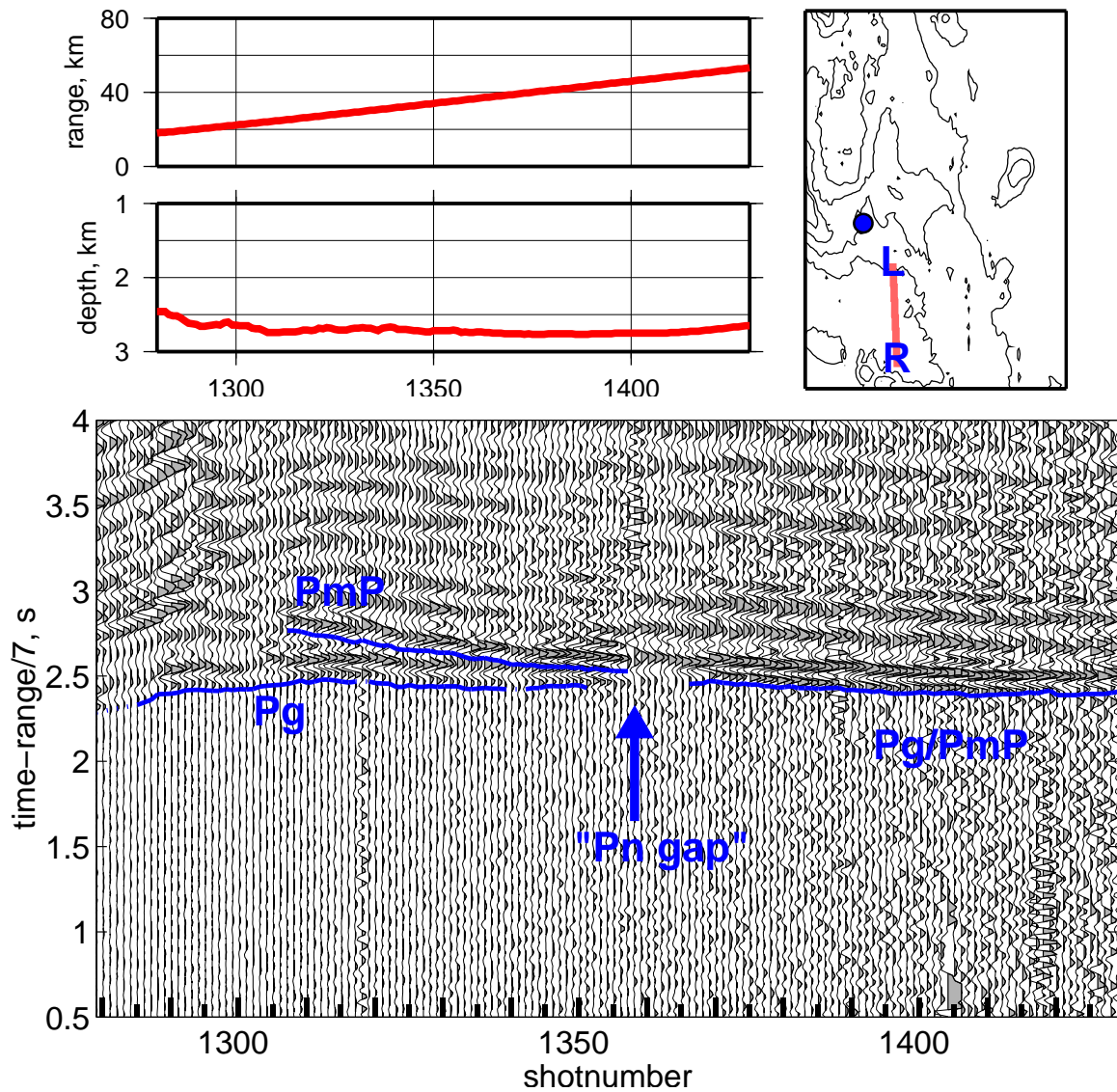
Figure 3.4 Example of Pn gap. Clear Pg and PmP phases are seen over this section of smooth bathymetry. Where the two converge, destructive interference eliminates the first arrival. Pn would emerge shortly after this gap though its amplitude is too small to be observed on this record. The Pn gap is used as a tool for locating and understanding the Pg/PmP/Pn triplication. Observations from "clean" records such as this help in understanding records over rough bathymetry or near lateral velocity gradients. Since the Pn gap observation is independent of traveltime it is a power tool in perturbed records.

Figure 3.5 Example of 1–D preliminary modeling based on single record section. A combination of forward and least squares inverse approaches were used on several records to obtain 1–D velocity models. **Top left:** Typical velocity profile. **Top right:** Rays paths through this structure. **Left:** Fit of observed and predicted traveltimes. An advantage of 1–D forward modeling is the easy incorporation of multiple phases. Early indications from such models suggested a crustal thickness of at least 8 km and mantle velocities of roughly 8 km/s.

Figure 3.6 Example of interactive semi–automated picking routine. In the **rear panel**, traveltimes have been picked on key traces where pulse shape or traveltime slope changes significantly or where a discontinuity occurs. **Front panel** The picking routine fills in the rest of the traces based on distance–weighted cross correlation averages with adjacent traces. The procedure occurs on screen so results can be manually adjusted afterwards. This set of traces also demonstrates the impact of the caldera low velocity zone. Shots are nearly equidistant from the OBS, yet a sharp discontinuity offsets first arrivals by 0.4 seconds as traces sweep across the caldera region.

$$S'=\sum_{j=1}^{n} S(t_i+r/v_{rock}+R/v_{water})$$

X, km

depth, km

time

θ_{max}

R

j=1 .... j=n

incident plane wave

time

$S=S(t_i)$
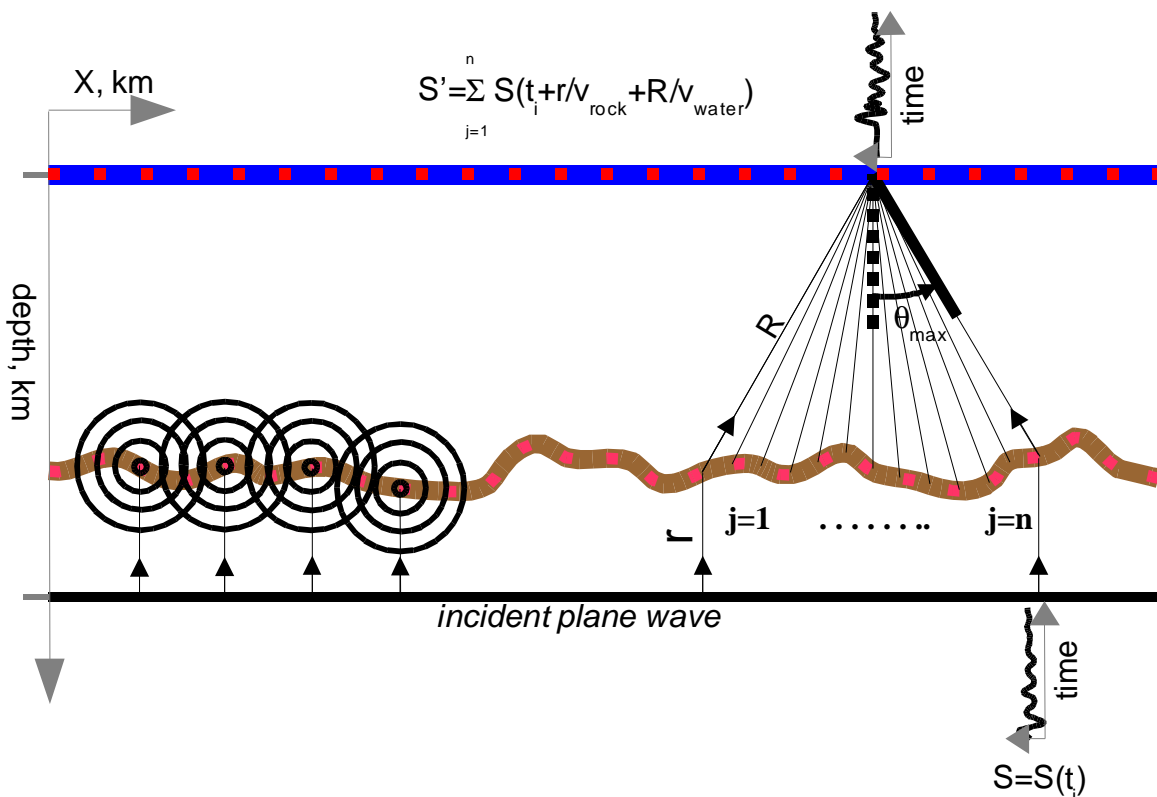
Figure 3.7 Model used to calculate effects of irregular seafloor topography on seismic traces. A vertically incident plane wave reaches the seafloor at a time determined by the topography and rock velocity. Each point on the seafloor is a Huygens scattering source radiating a spherical wave front (though the bathymetry is 2–D, 3–D geometrical spreading is included). At any point on the sea surface, the resulting wave form, S', is the summation of sea floor point sources. In practice, wide angle rays only contribute to the coda so the summation includes incident angles up to θ_{max}. A representative input wave form, S, was sampled from the data.
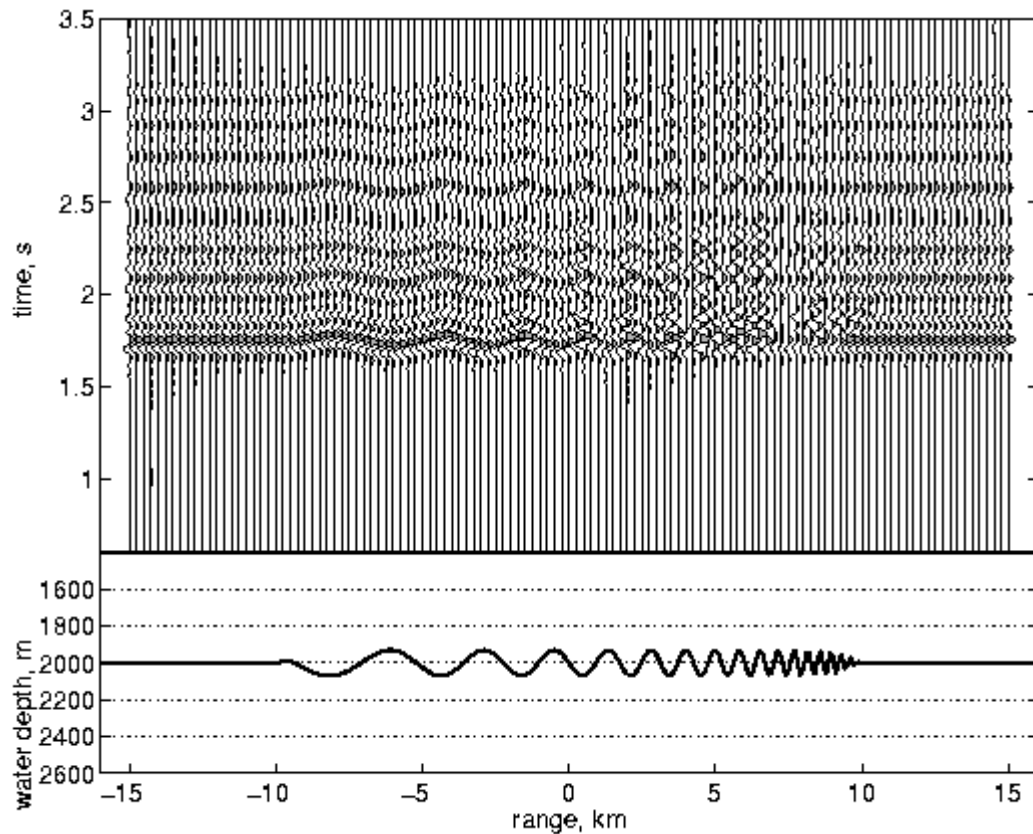
Figure 3.8 Sample results of bathymetry modeling (see fig. 3.7). Long wavelength seafloor topography is mirrored in traveltimes and does not affect amplitudes. Intermediate topography decreases trace coherency by affecting both traveltimes and amplitudes. Short wavelength features are largely invisible.
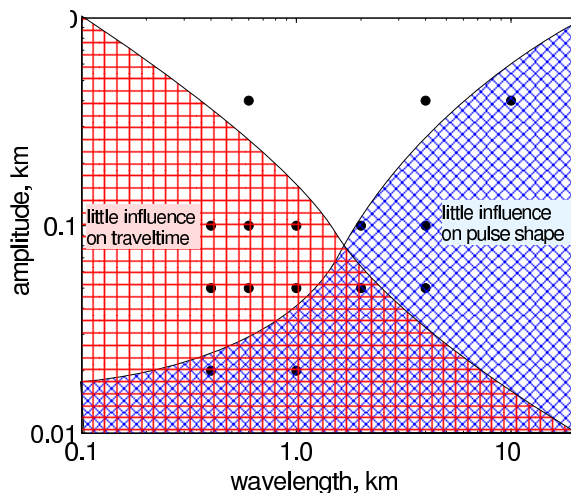
Figure 3.9 The effects shown in figure 3.8 are a function of topographic wavelength and amplitude. In this figure, the shaded region on the left shows wavelength and amplitude combinations which have only limited effect on traveltimes. The right shaded region marks combinations which have only limited influence on trace coherency. The two intersect in the bottom of the figure. Classifications are subjective estimates and reflect potential influence on this project. This information was used to understand effects observed on seismic records and to determine the resolution of bathymetry required in the raytracing models (features which are adequately smoothed by scattering effects, need not be included.)
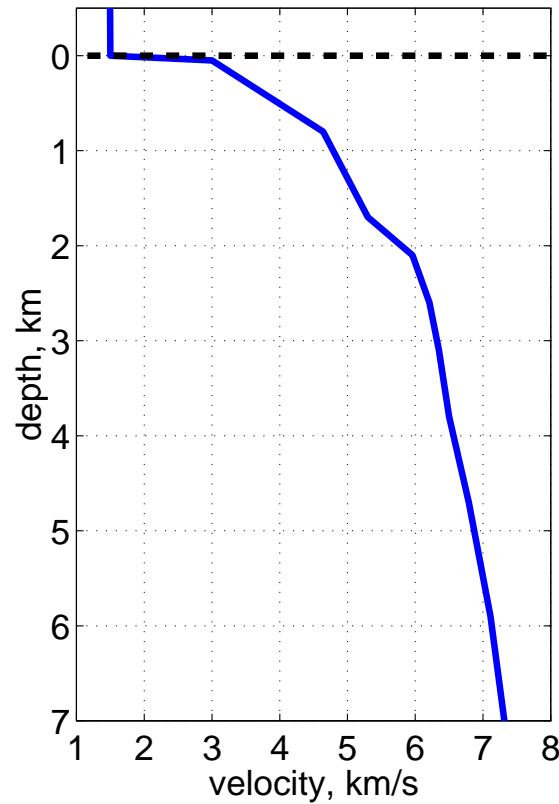
Figure 3.10 Final 1–D velocity model. This structure in the result of multiple 1–D topographic inversions (ray tracing in 3–D). The starting model for the inversions (not shown) is a synthesis of single line models (see fig. 3.5) and the shallow structure of Van Heeswijk *et al.* (1986) and Sohn *et al.* (1998). The inversion used only Pg phases so Moho is not present in the model. The profile is the base structure against which perturbations are measured. Since it does not include caldera–crossing rays, it represents oceanic crust which is cooler than near the caldera.
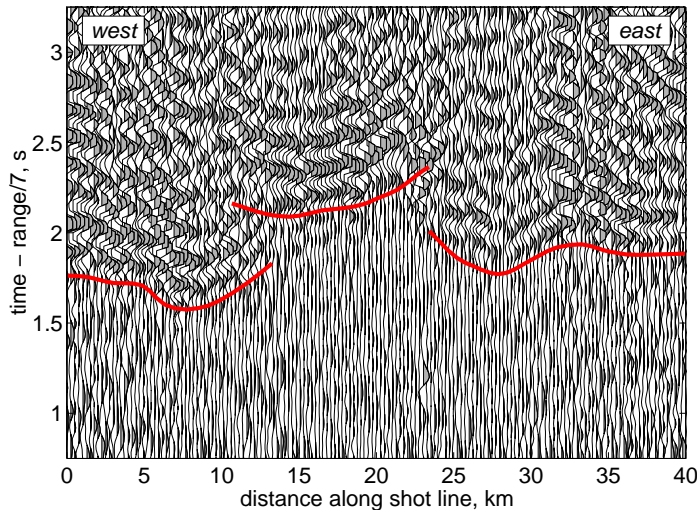
Figure 3.11 Top Record showing effect of low velocity zone (similar to fig. 3.6).

Middle Modeled low velocity zone. Simple 2–D model considers only the effects of horizontal velocity variations. While this model is not meant to accurately represent the low velocity zone beneath Axial it is a useful tool for understanding the possible origin of features in the seismic record.
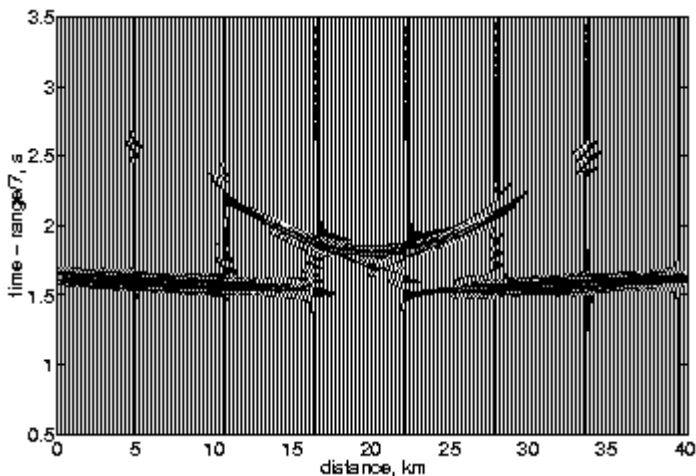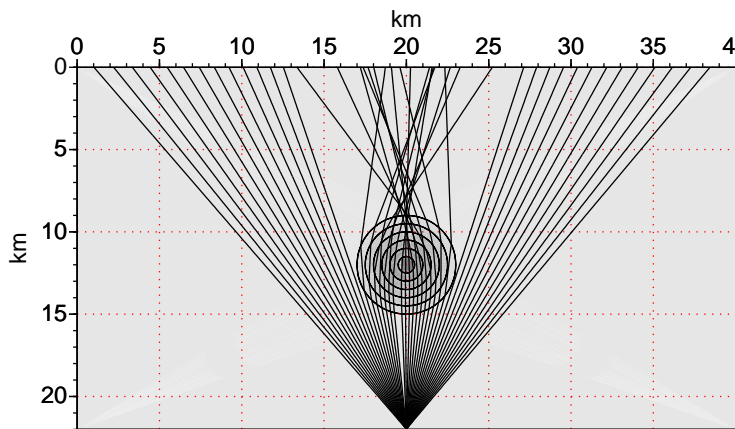
Bottom Waveform modeling through the low velocity zone shown above. Though such simple modeling does capture the nuances of the real seismic record, it is a tool for exploring the plausibility of different models.
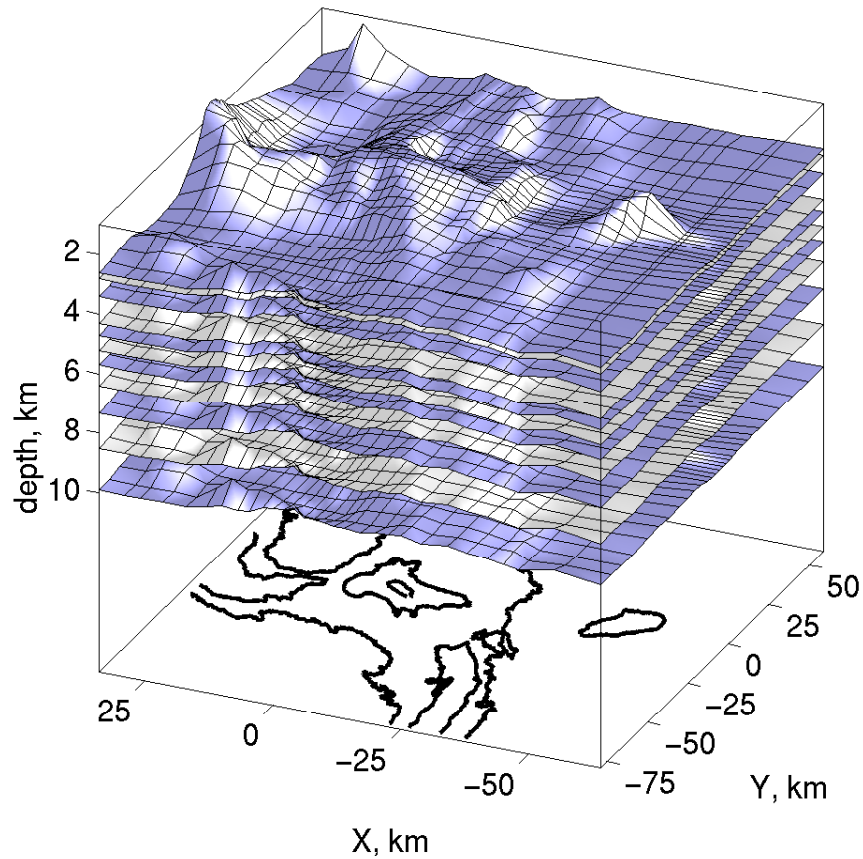
Figure 3.12 Grid used for raytracing and inversion. Pseudo–planes of nodes lie "parallel" to the seafloor. On each plane nodes are plaid in the horizontal dimensions. Horizontal grid spacing is 2x2 km near the caldera increasing around the edges where resolution is poor. Vertical spacing is 0.4 km in the shallow crust increasing to 1.5 km in the lower crust. The cartesian coordinate system is centered on 46°N / 130°W and rotated 26.65° so the Y–axis aligns with the ridge axis and the X–axis is perpendicular to the ridge. The system is right–handed with a positive Z–axis downward. The view is from the south. Shading of planes is only for clarity.

Figure 3.13 Vertical slices through final crustal velocity model. 3 slices are perpendicular to the rift zone, 3 are parallel. Figures are contoured at 0.5 km/s intervals. Yellow is 3.0–3.5 km/s. Darkest brown is > 7.0 km/s. Blue is the water. Blank regions do not have adequate ray density to be constrained. The most notable feature is the low velocity zone under the caldera. It is observed on the two caldera–crossing lines. While disturbances are seen away from the caldera, the bulk of the low velocity region is contained within the outer lines.
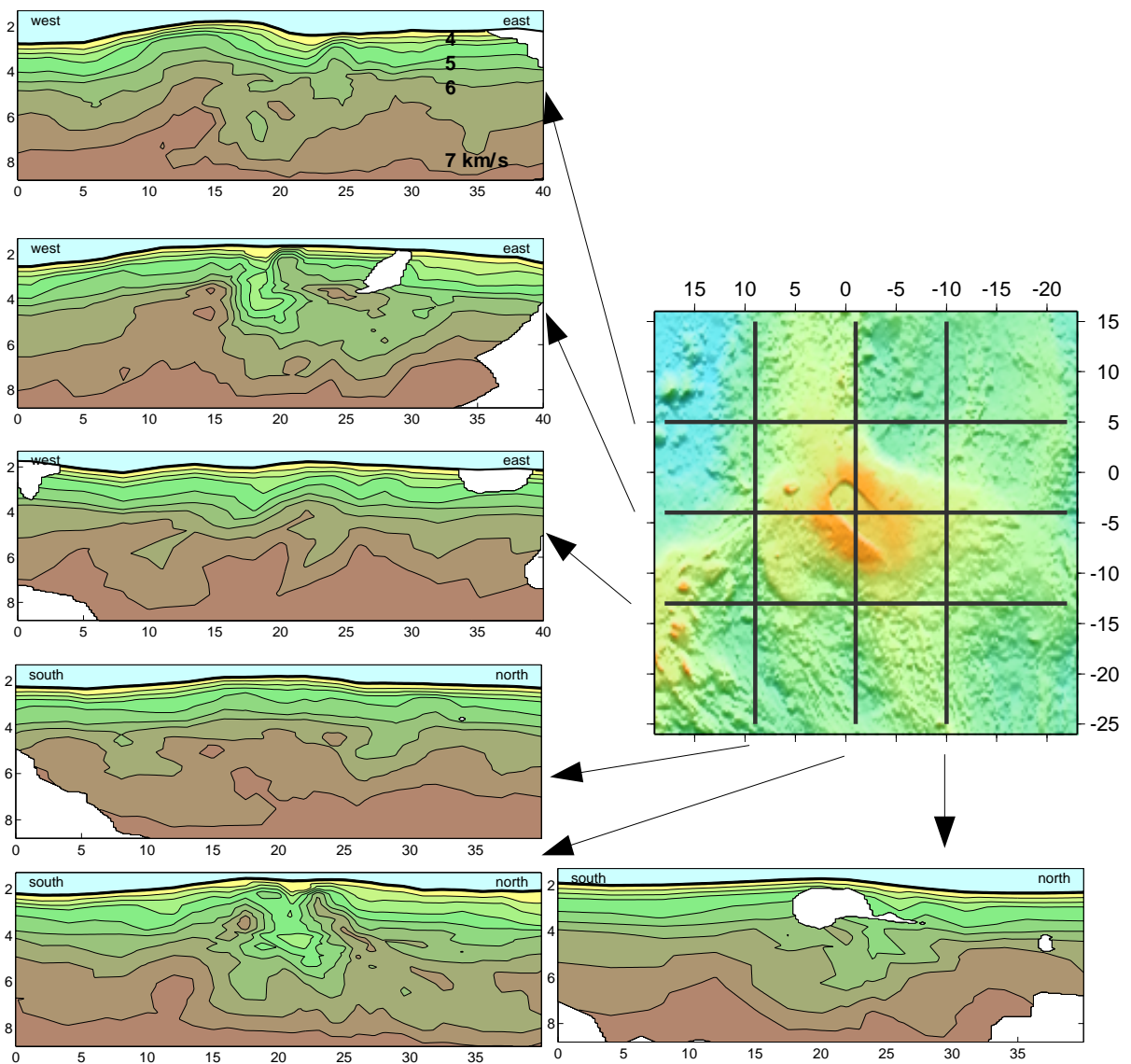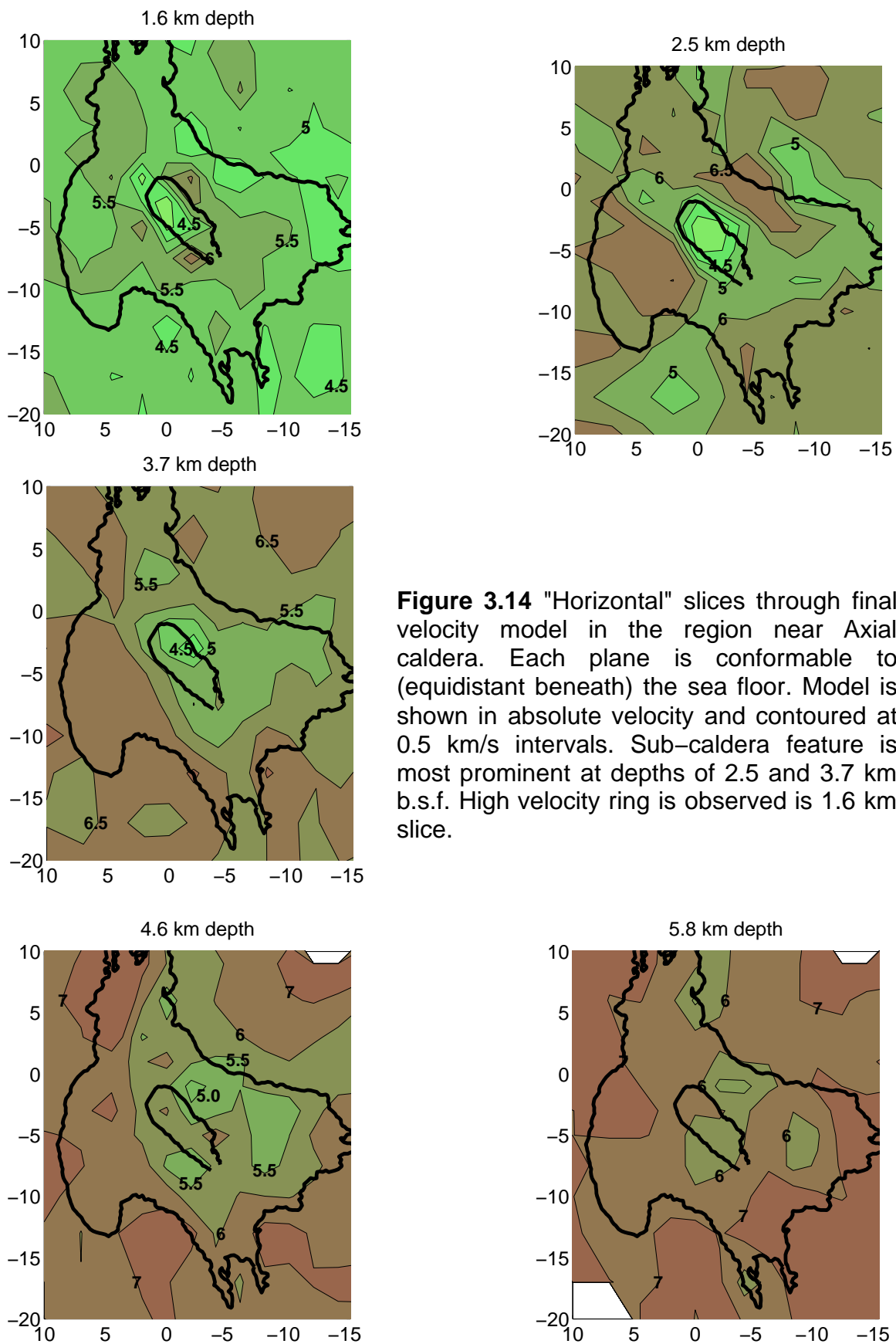
Figure 3.14 "Horizontal" slices through final velocity model in the region near Axial caldera. Each plane is conformable to (equidistant beneath) the sea floor. Model is shown in absolute velocity and contoured at 0.5 km/s intervals. Sub–caldera feature is most prominent at depths of 2.5 and 3.7 km b.s.f. High velocity ring is observed is 1.6 km slice.

IV. Massive magma reservoir beneath Axial Volcano,

Juan de Fuca Ridge

(Submitted to Nature, March 2001)

Axial Volcano is the dominant structure on the Juan de Fuca ridge, rising 700 meters above the adjacent segments with rift zones extending 100 km along the ridge axis (fig. 4.1). The melting anomaly that created the Cobb–Eickelberg chain of volcanoes, of which Axial is the most recent, has persisted at least 9 Ma[1], but has only recently begun to interact with the ridge. Ridge morphology and the volcano's off–center position in the current Brunhes magnetic anomaly[2] suggest that Axial lies as much as 15 km west of the original axis of the ridge. We show here that, despite its obvious influence on the ridge, the deeply rooted magmatic system beneath Axial is distinct from nearby ridge segments. The massive magma body which constructed Axial via a circular dike system now feeds eruptions to the summit and along Axial's rift zones. The volume of the magma body is larger than those beneath any of the shield volcanoes of Iceland[3,4] and is 2–3 times wider than the magma reservoir observed on the East Pacific Rise[5,6]. The magma chamber beneath Axial is the largest basaltic–type reservoir imaged to date.

Frequent seismic swarms and deformation events point to a robust magma supply system at Axial[7–9]. Lateral dike injection, observed during a 1998

eruption[10], originated from a source under the caldera and carried magma up to 50 km along the volcano's rift zones, which are substantial constructional features. Such diking events suggest that magma supply is strongly focused beneath the volcano. The existence of the 3x8 km summit caldera, and its 3 m subsidence during the 1998 eruption[11], imply substantial magma storage beneath the volcano. We show here that the reservoir feeding Axial is much larger than the volume of an eruption, with magma distributed over more than 100 km^3, containing 5–11 km^3 of magma.

The compressional velocity image of the volcano that we present here is based on data collected during a 1999 active seismic experiment. 5025 shots from the R/V Ewing's airgun array (20 guns totaling 142 liters) were recorded on six ocean bottom seismometers deployed on the volcano's flanks[12]. Water wave traveltimes and GPS–determined shot locations were used to precisely locate the seismometers on the sea floor (error <20 m) and to determine clock drifts (error < 0.02 s). The dense record sections permitted the identification of major compressional wave arrivals, including the crustal turning wave Pg, Moho reflected PmP and mantle refracted Pn. Traveltimes from 19,200 Pg phases are used in this study.

The most dramatic feature of seismic ray paths that cross the caldera is a sharply delineated zone in which Pg is delayed by up to 0.5 s (fig. 4.2). This delay is caused by a compressional wave low veloctiy zone beneath the caldera,

which we show is due to magma. The compressional velocity structure of the magma chamber and its surroundings is imaged by tomographically inverting the traveltime data. The velocity field is parameterized on an irregular tetrahedral grid, with prescribed water velocity and bathymetry drawn from multibeam sonar measurements. Traveltimes and their Frechet derivatives are calculated using ray theory, and a linearized damped least−squares method is used to update the velocity field. Three iterations of the inversion were performed, starting with a bathymetrically−draped one dimensional model, leading to a 51% reduction of the r.m.s. traveltime error. Resolution tests (fig. 4.3) demonstrate that good horizontal resolution extends to depths of 5−6 km below seafloor.

The tomography indicates that the low velocity zone is centered directly beneath the caldera, is oval in map view (8x12 km elongated NW−SE), and has a compressional velocity reduced by as much as 2 km/s relative to its surroundings (fig. 4.4). The most intense part of the anomaly (slow by more than 1.0 km/s) is confined to mid−crustal depths of 2.25−3.5 km below seafloor. The amount of magma in this region can be estimated using laboratory measurements of velocity in partially melted rock (see methods). Uncertainty in physical parameters requires a range of estimates, but we determine a lower bound on magma content by using conservative values. Minimum bounds on the magma stored in this well−defined mid−crustal reservoir range from 2.5−6.0 km^3 depending on the model of melt inclusion geometry. Melt fraction in the center of this reservoir exceeds 10−20% depending on the style of magma distribution.

This reservoir is 10–60 times larger than the 0.1–0.2 km^3 total estimated volume of the 1998 eruption[13]. Analysis of the rift zone dimensions and volcanic activity, combined with these melt estimates, suggests that magma resides in the crust for a few hundred to a few thousand years and possibly much longer before erupting. Basalts from the vicinity of Axial's caldera exhibit remarkably homogeneous chemistry[14] despite local mantle heterogeneity[15]. Tomographic resolution is insufficient to constrain whether the magma occurs in discrete macroscopic bodies or as a mush. If the melt phase is sufficiently connected however, the large volume of the magma chamber and the lengthy implied residence time suggest mixing may help to homogenize the chemistry.

A broad region of reduced velocities extends to at least 6 km depth, indicating that the crust beneath the magma chamber contains at least 2–5 km^3 of melt distributed in small concentrations (2%–6%) over a large volume. The lower crustal melt combined with the more concentrated reservoir above it, hold an estimated total of 5–11km^3 of magma. The melt in the deep crust is likely associated with on–going replenishment of the magma chamber. If the 1998 eruption marks the end of an eruptive period, as is suggested by the absence of post–eruption seismicity[7], the current presence of melt in the lower crust indicates that any periodicity is due to upper crustal processes and not intermittent replenishment from the mantle.

Away from the caldera, velocities increase smoothly with depth. Velocity

contours 4–6 km/s are upto 1 km deeper than on other parts of the Juan de Fuca[16,17]. The 0.5–1.0 km of additional extrusives implied by these depressed velocities is consistent with magmatic overproduction and the substantial volcanic edifice. Theories explaining magma chamber depth, including neutral buoyancy[18] and hydrothermal freezing horizons[19], predict magma near the transition from extrusive basalts to intrusive gabbros. The thicker extrusives at Axial may help keep the magma chamber at depth despite the high rate of magma injection.

Above the magma reservoir, a well–defined ring of high velocity material (up to 1.0 km/s fast) intrudes the layered background (fig. 4.4,4.5). This high velocity ring is slightly larger than the caldera and roughly the same size as the summit plateau. Rings like these can sometimes arise as artifacts in tomographic imaging. We exclude this possibility here, since the ring is associated with specific traveltime advances on near–offset, caldera–crossing lines (fig. 4.1). The 5.5–6.5 km/s velocities of this feature suggest a ring of cold dense basalt at shallow depths[20].

Mitchell[21] highlights the role of circular magma supply systems in young submarine volcanoes preceding a transition to rift dominated volcanism. While Axial is clearly rifting, it has yet to accommodate enough extension to split its summit plateau (fig. 4.1). We propose the high velocities observed under the perimeter of Axial's summit are the result of repeated emplacement of magma

through sub–vertical ring dikes as the volcanic edifice was being constructed. The subsequent onset of rift volcanism has begun to elongate the feature.

The caldera, located within the ring, is merely the most recent visible collapse feature. This high velocity ring occurs immediately below and outside the caldera walls, which are the morphologic expression of a fault system that accommodates caldera inflation and deflation. Eruptions through the caldera edges and along summit rifts, such as in 1998, reinforce this feature by intruding more magma into the shallow extrusive zone.

The extrusion of new material onto pre–existing oceanic crust has built up a broad volcanic edifice at Axial. Though rifting across the volcano is clearly occurring today, the dominance of radial symmetry (instead of 2–D symmetry) of the magma supply suggests Axial is very young and has accommodated little rifting thus far. Rift zone morphology suggests an age of roughly 50,000 years[22]. The few kilometers of spreading during this time could account for the slight cross–axis elongation of the magma reservoir, the summit plateau and the ring dike feature. The magma system of Axial Volcano is not observed to extend northward or southward into the regions of the Coaxial and Vance segments of the Juan de Fuca Ridge. There appears to be no steady–state connectivity with the magma chamber on Coaxial segment, 15–20 km away, that was responsible for the 1993 lateral diking event. This lack of connectivity is consistent with the significantly different trace–element ($^{87}Sr/^{86}Sr$) chemistry reported for Axial and Coaxial basalts[15]. It also implies a very focused magma transport process to

Axial through the uppermost mantle, that allows little mixing of magma over horizontal scale lengths of 20 km.

Images of the central magma body under Axial Volcano, together with deep crust melt constraints and shallow intrusive features, provide a clear picture of a hybrid volcano−ridge. Axial fills a knowledge gap between basaltic shield volcanoes and mid−ocean ridges and provides a glimpse of how the former transitions into the latter. The interaction of hot spot and ridge has produced a volume of melt too large to be removed by a few eruptions and strongly suggests melt is a steady−state feature of Axial Volcano.

Methods

Melt estimates. Assuming a predominately basaltic composition, and minimal open pore space at the depth of the low velocity zone, velocity perturbations are controlled by temperature, degree of crystallization, melt fraction and melt distribution. We evaluate the low velocity anomaly relative to cooler, more crystalline conditions which are assumed away from the caldera. We subtract 5% of the low velocity anomaly to account for possible differences in the degree of crystallinity between basalt and gabbro[20]. We then remove an additional 6% of the anomaly to allow for sub−solidus temperature differences [23,20]. We attribute the remaining velocity anomaly to melt fraction based on several independent studies[20,23−26]. Our estimates encompass the full range of velocity to melt functions with Takei[24] predicting the most conservative melt content and Sato

and Sacks[23] yielding somewhat larger values. This range allows for uncertainty in mineral composition and the style of melt distribution. Larger melt volumes reflect models with low magma connectivity (low aspect ratio inclusions or large dihedral angle grain contacts) while smaller volumes reflect models with more magma connectivity (high aspect ratio inclusions or films, small dihedral angle grain contacts).

Acknowledgments

1. Desonie, D.L. & Duncan, R.A. The Cobb–Eickelberg seamount chain; hotspot volcanism with mid–ocean ridge basalt affinity. *J. Geophys. Res.*, **95,** 12,697–12,711 (1990).

2. Tivey, M.A. & Johnson, H.P. The magnetic structure of Axial Seamount, Juan de Fuca Ridge. *J. Geophys. Res.*, **95,** 12,735–12,750 (1990).

3. Gudmundsson, O. Brandsdottir, B. Menke, M., & Sigvaldason, G.E. The crustal magma chamber of the Katla volcano in South Iceland revealed by 2–D seismic undershooting. *Geophys. J. Int.* **119,** 277–296 (1994).

4. Brandsdottir, B., Menke, W. Einarsson, P., White, R.S., & Staples, R.K. Faroe–Iceland Ridge experiment; 2, Crustal structure of the Krafla central volcano. *J. Geophys. Res.***102,** 7867–7886 (1997).

5. Dunn, R.A., Toomey, D.R. & Solomon, S.C. Three–dimensional seismic structure and physical properties of the crust and shallow mantle beneath the East Pacific Rise at 9°30'N. *J. Geophys. Res.* **105,** 23537–23555 (2000).

6. Toomey, D. R., Purdy, G. M., Solomon, S. C. & Wilcock, W. S. D. The three–dimensional seismic velocity structure of the East Pacific Rise near latitude 9 degrees 30' N. *Nature* **347,** 639–645 (1990).

7. Dziak, R. P. & Fox, C. G. Long–term seismicity and ground deformation at Axial Volcano, Juan de Fuca Ridge. *Geophys. Res. Lett.* **26,** 3641–3644 (1999).

8. Tolstoy, M., Vernon, F.L. & Orcutt, J.A. Magmatic Activity on Axial Seamount: A Combined Ocean Bottom Seismic and Tilt Experiment. *EOS Trans., AGU*, (1997).

9. Sohn, R.A., Crawford, W.C. & Webb, S.C. Local seismicity following the 1998 eruption of Axial Volcano. *Geophys. Res. Lett.* **26,** 3433–3436 (1999).

10. Embley, R. W., Chadwick, W. W. Jr., Clague, D. A. & Stakes, D. 1998 eruption of Axial Volcano; multibeam anomalies and seafloor observations. *Geophys. Res. Lett.* **26,** 3425–3428 (1999).

11. Fox, C. G. In situ ground deformation measurements from the summit of Axial Volcano during the 1998 volcanic episode. *Geophys. Res. Lett.* **26,** 3437–3440 (1999).

12. Webb, S.C., Deaton, T.K., & Lemire, J.C. A broadband ocean bottom seismometer system based on a 1 Hz natural period geophone, *Bull. Seismol. Soc. Am.*, (in press).

13. Chadwick,William. W. Jr., Embley, R. W., Milburn, H. B., Meinig, C. & Stapp, M. Evidence for deformation associated with the 1998 eruption of Axial Volcano, Juan de Fuca Ridge, from acoustic extensometer measurements. *Geophys. Res. Lett.***26**, 3441–3444 (1999).

14. Rhodes, J. M., Morgan, C. & Liias, R. A. Geochemistry of Axial Seamount lavas; magmatic relationship between the Cobb hotspot and the Juan de Fuca Ridge. *J. Geophys. Res.* **95,** 12713–12733 (1990).

15. Embley, R. W., Chadwick, W. W., Perfit, M. R., Smith, M. C. & Delaney, J. R. Recent eruptions on the CoAxial segment of the Juan de Fuca Ridge: Implications for mid–ocean ridge accretion processes *J. Geophys. Res.***105,** 16501–16525 (2000).

16. Sohn, R.A., Webb, S.C., Hildebrand, J.A., & Cornuelle, B.D. Three–dimensional tomographic velocity structure of upper crust, CoAxial segment, Juan de Fuca Ridge; implications for on–axis evolution and hydrothermal circulation. *J. Geophys. Res.* **102,** 17,679–17,695 (1997).

17. Cudrak, C.F., & Clowes, R.M. Crustal structure of Endeavour Ridge segment, Juan de Fuca Ridge, from a detailed seismic refraction survey. *J. Geophys. Res.* **98,** 6329–6349 (1993).

18. Ryan, M.P. In *Magmatic Systems* (ed. Ryan, M.P.) 97–135 (International Geophysics Series 57, Academic Press, Inc., San Diego, CA, 1994)

19. Morgan, J.P., Chen, J.Y. The genesis of oceanic crust; magma injection, hydrothermal circulation, and crustal flow. *J. Geophys. Res.* **98,** 6283–6297 (1993).

20. Christensen, N. I. Compressional wave velocities in rocks at high temperatures and pressures, critical thermal gradients, and crustal low–velocity zones. *J. Geophys. Res.* **84**, 6849–6857 (1979).

21. Mitchell, N.C. Transition from circular to stellate forms of submarine volcanoes. *J. Geophys. Res.* **106,** 1987–2003 (2001).

22. Hammond, S.R. & Delaney, J.P. Evolution of Axial Volcano, Juan de Fuca ridge. *Eos. Trans. AGU.* **66,** 925, (1985).

23. Sato, H., Sacks, I. S. & Murase, T. The use of laboratory velocity data for estimating temperature and partial melt fraction in the low–velocity zone; comparison with heat flow and electrical conductivity studies. *J. Geophys. Res.* **94,** 5689–5704 (1989).

24. Takei, Y. Constitutive mechanical relations of solid–liquid composites in therms of grain–boundary contiguity. *J. Geophys. Res.* **103,** 18183–18203 (1998).

25. Stocker, R.L. & Gordon, R.B. Velocity and internal friction in partial melts. *J. Geophys. Res.* **80,** 4828–4836 (1975).

26. Humphreys, E.D. & Dueker, K. G. Physical state of the Western U.S. upper mantle. *J. Geophys. Res.* **99,** 9635–9650 (1994).

Appendix A – Expanded details of melt estimates

Assuming a predominately basaltic composition, and minimal open pore space at the depth of the low velocity zone, velocity perturbations are controlled by temperature, crystal size, melt fraction and melt distribution. While it is not possible to simultaneously solve for all parameters, maximum bounds can be can be placed on crystallinity and thermal effects to determine a minimum melt content.

Since the thermal structure of Axial is unknown we allow temperature to explain as much of the velocity anomalies as laboratory data allows. Christensen (1979) has observed temperature–induced velocity changes in an East Pacific Rise basalt sample of 3.5% Compressional velocity in a mid–Atlantic Ridge gabbro varied by 4.8% under similar testing conditions. Sato (1989) notes a maximum of 6% change in velocity over a range of subsolidus temperatures.

We must also account for a range of crystalline structures at the depth of the magma body. While the deeper parts of the crust are likely gabbro, basaltic compositions may exist in the upper parts of the magma chamber. Since these nuances are not constrained we consider the possibility that composition accounts for some of the observed velocity anomalies. The velocities of the low–porosity basalt sample and the gabbro discussed above can differ by as much as 8% though pure basaltic and gabbroic structures are unlikely to occur along the same depth horizons.

To account for these thermal and compositional differences, 11% of all variation in compressional velocity (relative to the background 1−D structure) is attributed to thermal and compositional effects. The remaining velocity anomaly is attributed to melt.

Several authors have considered the effect of partial melt on seismic velocities. The wide range of results (fig. 4.6) illustrates the numerous conditions under which melting can occur. Humphreys and Dueker[26] and Takei[24] allow a range of values that reflect the role of melt distribution within the rock. In general, high aspect ratio melt inclusions such as elongate pore space or dikes allow the liquid phase to reduce velocities more effectively than low−aspect ratio inclusions which do not permit as much connectivity of the liquid. Different types of melt distribution are responsible for much of the variation observed in the figure. We use a range of velocity to melt conversions to account for this effect. Sato[23] arguably presents the most robust data as the values come from laboratory tests of rock samples at all stages of melting. We do not use the high melt fraction limit of Humphreys and Dueker[26] because of their simplistic linear assumption. The remaining curves are used to calculate the required melt in the magma chamber velocity models. The minimum and maximum melt contents reflect the variety of velocity to melt functions presented here. Larger melt volumes reflect models with low magma connectivity (low aspect ratio inclusions, large dihedral angle) while smaller volumes reflect models with more magma connectivity (high aspect ratio inclusions or films, small dihedral angle).
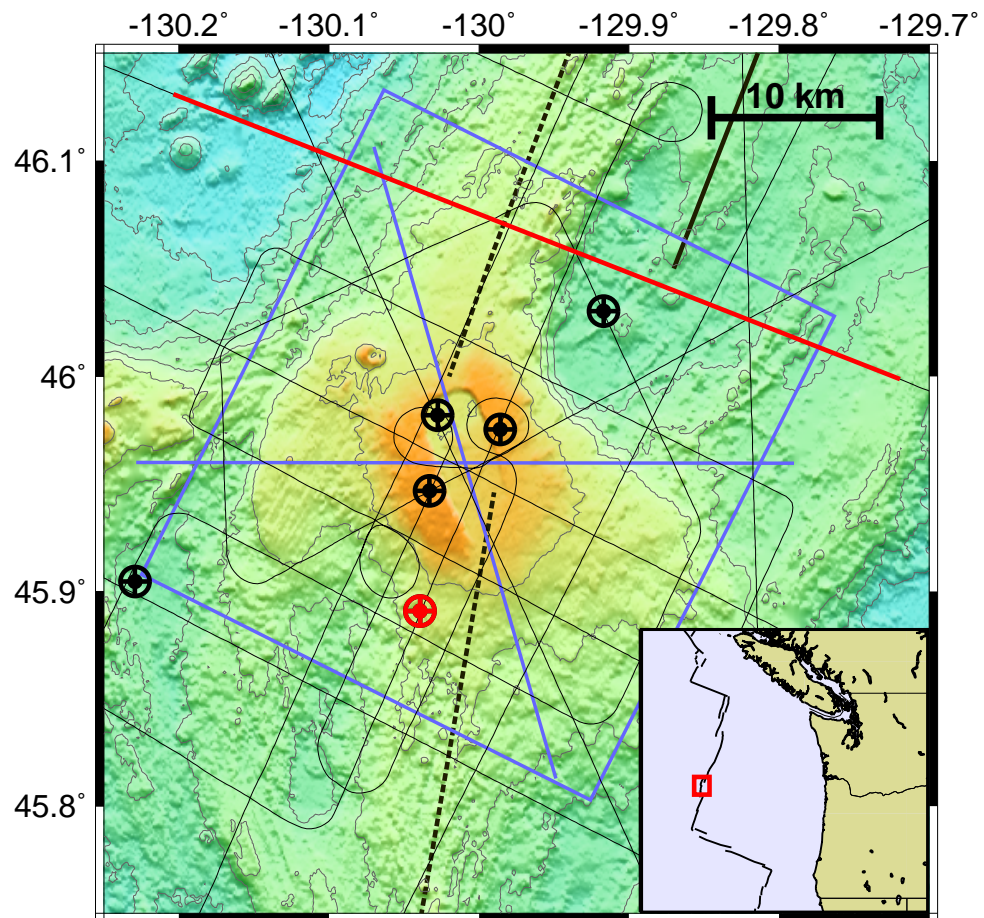
Figure 4.1 Bathymetry of Axial Volcano. Orange is 1400 meter depth, blue is 2800 meter depth, contour interval is 200 meters. Summit caldera is in center of figure. Bold dotted lines mark the north and south rift zones. The southern end of the adjacent CoAxial segment is marked with a bold solid line. Thin black lines mark airgun shot lines, bulls eyes show ocean bottom seismometers used in analysis. Blue box is area shown in figure 4.3. Two blue lines mark cross–sections in figure 4.4. The red line and seismometer display shot geometry for figure 4.2. Inset map shows experiment location on the Juan de Fuca Ridge. A 10 km scale bar is in upper right corner**.**
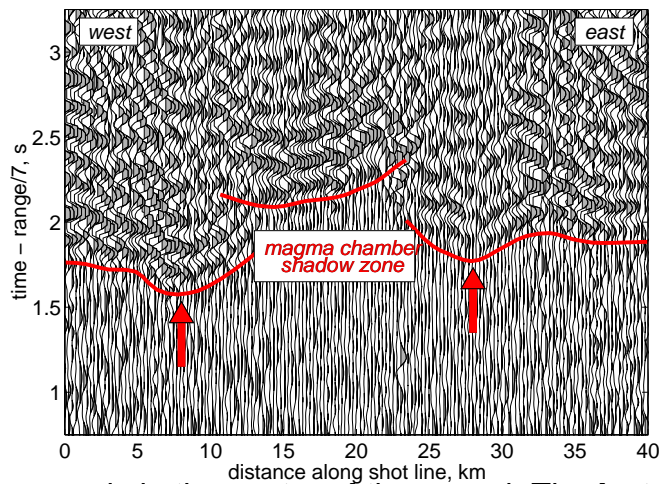
Figure 4.2 Example record section. Shot–receiver geometry is marked on figure 1. A 2–8 Hz bandpass filter and a static topography correction have been applied for viewing purposes. Rays from this fan shot cross the caldera at depths of a few kilometers. Shot ranges are 20–29 km. The massive low velocity anomaly is clearly evident in the traveltimes delayed by more than 0.5 seconds in the center of the record. The feature is evident on numerous records with similar geometry across the caldera. The early–arriving bumps on either side of the delayed region (marked by arrows) show the effect of the high velocity ring. This feature is observed on multiple records as well.

Figure 4.3 Results of checkboard resolution tests in a 25x25 km box. The synthetic input model (**left panels**) were created by adding a grid of 3–D gaussian–shaped anomalies to the 1–D structure. Traveltimes were forward modeled by raytracing through this structure using a geometry identical to the one in the real tomographic inversion and assuming similar errors. The same inversion strategy was then applied to the synthetic data set to see how well the input structure could be recovered (**right panels**). Three depth sections are shown here. The shallow resolution (0.7 km below seafloor) is noisy though general features are recovered. At depths of the low velocity zone (3.0 km) the anomalies are well–located. Peak amplitudes are somewhat less than in the input model as a result of smearing. Deeper in the crust (4.6 km) the overall geometry is recovered though smearing is more evident. In the mid and lower crust under the caldera, this test demonstrates our ability to resolve features similar to the observed magma chamber. The effect of smearing is to conservatively underestimate the true amplitude of anomalies.

Figure 4.4 East–west (**top panel**) and northwest–southeast (**lower panel**) profiles through caldera as marked in figure 4.1. Compressional wave velocity is contoured in intervals of 0.5 km/s. The caldera extent is indicated above panels. Depths are relative to the caldera floor, which is 1.46 km below sea floor. The low velocity zone directly beneath the caldera is the result of a partially molten magma chamber. Fingers of high seismic velocities penetrate up around the low velocity zone to within 0.5 km of the seafloor. These panels show a degree of radial symmetry beneath Axial with features being somewhat elongated along the caldera.

Figure 4.5 Southeast view of 3–D iso–surface velocity contours beneath volcano. Box is 16x16 km and 5 km high. Dotted axes show the surface has been lifted for viewing purposes. Scale box is 3x3 km. Red iso–surface marks the volume with compressional velocity at least 1.0 km/s slow relative to best–fit 1–D regional structure. Blue iso–surface marks rock with compressional velocity at least 0.3 km/s fast. This high velocity ring is above the low velocity zone, just wider than the caldera and elongated along the same axis as the caldera.
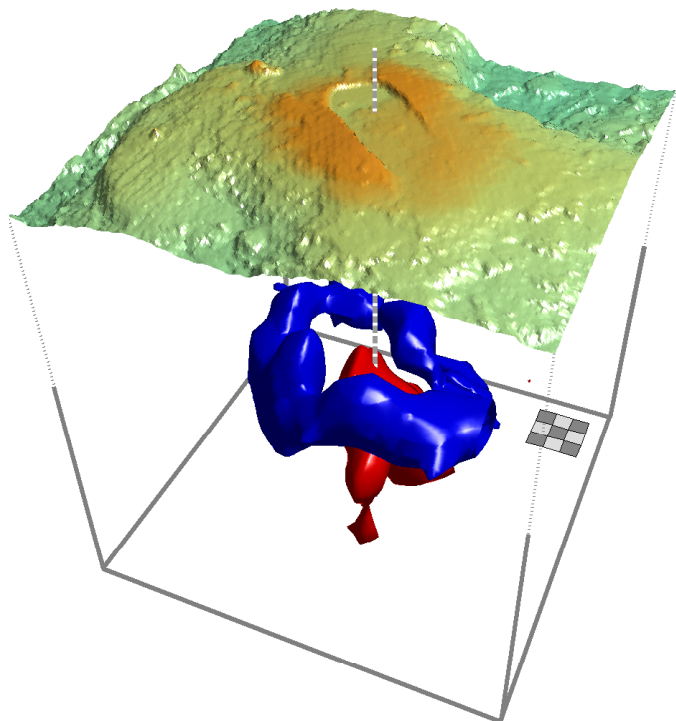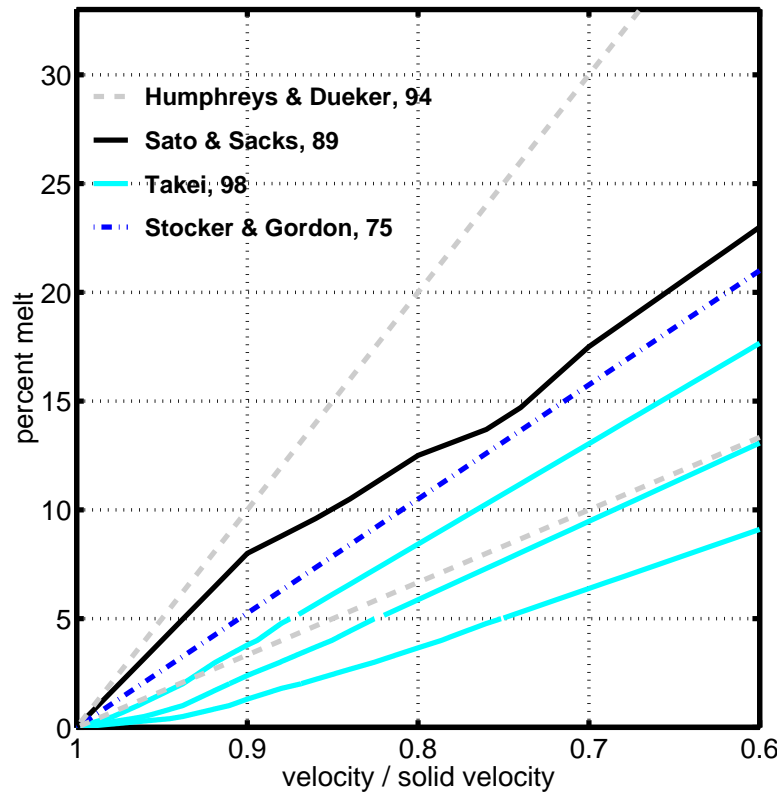
Figure 4.6 Velocity anomaly to melt relationships used to estimate the magma content of the caldera low velocity zone. Before applying any of these functions, estimates of velocity change due to temperature and composition are removed.

V. Regional and upper mantle observations at Axial Volcano

5.1 Low velocity zones on the flanks of Axial

5.1.1 Northeast flank low velocity anomaly

The sub–caldera low velocity zone dominates the velocity structure near Axial. There are other significant features however, in addition to the high velocity ring, which warrant attention to what they may suggest about the geology of the volcano. Two regions of anomalous low seismic velocities stand out in figure 3.14, most prominent at a depth of ~2.5 km.

10 km northeast of the caldera is a 50 km^2 region underlain by low velocities. The anomaly peaks at 3 km depth and continues down to at least 6 km. While the size is comparable to the central caldera anomaly, the amplitude is much smaller.

Late arrivals associated with this feature are observed for several geometries (fig. 5.1). These records also show that the low velocity volume (LVV) under the northeast flank is distinct from the central anomaly at mid–crustal depths. A small volume of rock has a velocity anomaly of –1.0 km/s while most of the volume is slow by no more than –0.5 km/s. Figure 5.2 shows the distribution of the anomaly vs. depth. The presence of melt cannot be shown unequivocally. However, the maximum anomalies are hard to explain without at least a small

melt fraction. Using the previously established criteria, this region could contain up to 0.3 km^3 of melt. Alternatively, it could be purely a thermal and/or compositional effect.

Below 5 km depth, the northeast flank anomaly and the caldera magma chamber are connected by a slow feature (fig. 5.3). The velocity difference is not great (less than 0.6 km/s) but enough to suggest high temperatures or perhaps small amounts of melt. Even so, the thermal or compositional feature between these regions suggests that the northeast flank anomaly is (or was) sourced by the same region of the lower crust.

If magma is currently fluxing through the northeast flank anomaly then volcanic activity should be evident. Sohn *et al.* (1999) recorded seismic activity under the eastern flank which they interpreted as extension or shearing related to the CoAxial or Vance segments. The topographic high in this area also hints at something under the flank. However, the possibility of volcanic activity northeast of the caldera remains speculative. If the northeast flank velocity anomaly is fed by the same source as the caldera, magmas associated with the east flank should carry the same geochemical signature as the caldera eruptives. At present, basalt sample coverage is not adequate to corroborate this hypothesis, but the possibility of a common source with the caldera magma reservoir should be considered by future geochemical surveys.

A second interpretation is that the northeast flank anomaly is the remnant of a

previously active magma chamber. Though it is not in–line with the migration of the Cobb hot spot, an intermediate magma chamber could have been created during the supposed ridge jump to the Axial rift zones. The left over heat, and possible melt, from this body could be creating the observed seismic effects. Either way, the low velocity volume observed 10 km northeast of the caldera remains poorly understood.

5.1.2 Southeast flank low velocity anomaly

15 km southeast of the caldera lies a third smaller low velocity volume (fig. 5.3). Its velocity perturbations (less than 0.7 km/s) do not require melt. Unlike the northeast flank anomaly, this one does not appear to have a deep root in the crust. Figure 5.4 shows the area of the anomaly with respect to depth. This feature is largely confined to depths of 2–3 km b.s.f. Despite the low velocities, there is little evidence to suggest that this body is an independent active magma reservoir. Still, the substantial material differences implied by the velocities are enough to warrant consideration.

At the depth of this feature, it is unlikely that porosity could account for the observed low velocities. Compared to other studies (Cudrak 1993, Sohn 1997) and even this study, 3+ km is too deep to be in the sheeted dikes or the shallower extrusive layers. If a thickening of layer 2 is responsible for this anomaly it is localized to the southwest flank. Other causes for such a velocity perturbation are composition, heat and partial melt. Assuming a basaltic chemistry, it is hard to get these perturbations even if the LVZ is entirely basalt

set in crystalline gabbro. This is doubtful even if a magma reservoir once existed. Solidified magma chambers have been shown by several authors (Foulger and Toomey 1989) to be seismically fast, presumably because they too are well–crystallized. Heat and partial melt remain as the two viable explanations for these slow velocities.

Since no deep root is observed under the anomaly it seems more likely that it is sourced laterally. Evidence is not conclusive, but it is possible this region is sourced by the highly productive central magma chamber. Current diking appears to be concentrated in the north and south rift zones, but perhaps additional melt is or was supplied to dikes from the southwestern flank of the volcano. The strong rift–parallel lineations on either side of the anomaly (fig 3.4) support this suggestion. Geochemical data may hold the key to proving or disproving this claim.

5.2 Crustal thickness and the Cobb Hotspot

5.2.1 Crustal thickness from Moho reflected phases

Strong Moho–reflected PmP phases are observed throughout the data set at ranges greater than 20 km. Preliminary 1–D modeling revealed a crustal thickness of roughly 8 km away from the caldera (fig. 3.5). This discovery of thickened crust, predicted by previous research (Hooft *et al.* 1995), suggested that a comprehensive survey of crustal thickness across Axial is warranted. 1677 PmP arrivals in 44 separate phase observations are used in this analysis.

Traveltimes are picked using the picking scheme described in section 3.1.2. We estimate error in the traveltime picks at well under 0.02 s (3 samples).

The traveltimes are a function not only of the Moho but also of the overlying crustal structure. Using the structure provided by the tomographic study, PmP traveltime misfit can be attributed to crustal thickness variations. Errors associated with traveltime prediction through the 3–D model (< 0.07 s) are propagated into the Moho estimates as well.

Velocities in the upper 6 km of crust are based of the 3–D tomography results. Outside the zone of resolution, the crustal structure is based on the best fit regional 1–D model. Velocities are 7.0–7.2 km/s at a depth of 6 km. To reach Moho, we augment this model with lower crustal velocities of 7.2–7.4 km/s and examine errors from this assumption *a posteriori*. Allowing a full range of geologically plausible velocities (7.0–7.7 km/s) introduces 0.06 s of error into the traveltime predictions.

A multiple–model comparison method is used to determine depth to Moho. Nine test models are created by adding a flat reflector to the crustal velocity model at depths of 6 to 14 km below sea surface at 1 km intervals. Predicted PmP traveltimes for each model are derived by raytracing for the reflected phase. Modeled traveltimes are interpolated to find the Moho depth which predicts zero traveltime error at each point of reflection. These depth are gridded to create a Moho surface. Gaps in the coverage are filled via linear interpolation on a

Delaunay–triangulated surface. Away from the convex area defined by the PmP bounce points, the Moho is tied to a crustal thickness of 8 km. This approximate thickness away from the caldera is suggested by 1–D velocity models derived from record sections such as figure 3.3. The preliminary Moho surface is then smoothed with a moving box averaging filter.

The flat Moho assumption introduces error since a sloping interface will have a different PmP reflection point. To incorporate this effect, the entire procedure was run again, replacing the flat Moho in the preliminary models with the smoothed undulating Moho. Of the original PmP phases, 770 were successfully traced through the final model. After smoothing, the PmP traveltime misfit was 0.10 s. Considering the two–way traveltime error of 0.20 s, lower crustal velocities of 7.0–7.8 km/s, the Moho depth error is estimated as ~0.9 km.

Table 5.1

picking error	*0.02 s*
crustal model error	*0.07 s*
lower crustal V misfit	*0.06 s*
PmP misfit in smoothed model	*0.10 s*
total PmP traveltime error	*0.20 s*
depth error of Moho	*~0.9 km*

5.2.2 Crustal thickness under Axial

Crustal thickness is reliably determined in much of the area within 25 km of the caldera. Gaps in coverage are attributable to a lack of ray coverage with

appropriate offset (~20–40 km) or an inability to detect PmP energy due to high attenuation, particularly near the magma chamber. The latter was a limiting factor for crustal measurements directly under the caldera. Most Moho observations are 5–20 km away from the summit. This coverage is sufficient to constrain two separate observations about the Moho.

The most significant observation is a thickening of the crust under Axial. The maximum crustal thickness of 11 km is nearly twice the thickness of "typical" 6 km oceanic crust (fig. 5.5). Very thick crust has been observed under hot spot related islands including the Marquesas (15–17 km) and Hawaiian islands (Caress *et al.* 1995). And crustal thickness variations of a few kilometers have been observed on both slow and fast spreading ridges (Barth and Mutter 1996, Hooft *et al.* 2000). However, 11 km crust is further evidence that Axial should not treated as just an over–productive ridge.

The area of greatest thickening does not extend along–axis nor is it observed off–axis (fig. 5.5). The crust thins rapidly to no more than 8.5 km within 15 km of the caldera in all directions.

The bump on the Moho is remarkably similar to the inverted shape of the volcanic edifice – round, 20–40 km in diameter and perhaps even elongated NW–SE, like the volcano, the caldera and the crustal magma chamber. It is also worth noting a relatively thin region of crust under the Helium basin. Though it is not well constrained, this is an additional place where topside crustal variations

are correlated with Moho variations.

5.2.3. Volcanic productivity

Much of the crustal thickening under Axial is local. In places, the slope of the Moho is much steeper than on the topside flanks of the volcano. Steep Moho topography has been observed before (Caress *et al.* 1995, Staples *et al.* 1997) and is thought to result from differences in volcanic productivity. Excess melt delivery will create thicker crust to accomodate the extra material. What is notable at Axial is the small area of the crustal thickening. While 100 km of ridge may have crust thickened by 1–2 km (Hooft *et al.*1995), the region with crust in excess in 9 km is no more than 300 km^2.

This is strong evidence for focused magmatism under Axial. If Axial's rift zones are being fed by a sheet–like diapir in the mantle, an inverted ridge of thick crust would be expected. Instead, the Moho variation strongly mirrors the topside relief. A small cylindrical region of melt production is more consistent with the observed crustal thickness than 2–D sheet flow assumed under many ridges. Viscosities near the Moho and the role of lateral gravitational stress and flow are poorly known, but there is little reason not to expect significant Moho topography. If this relief is indicative of the melt supply, then not only does Axial appear independent of the CoAxial and Vance segments of the Juan de Fuca, the high productivity does not even appear to extend under Axial's rift zones.

By applying a ridge anology (albeit a questionable one), we can place limits on

the total melt supply. Whether thick crust is the result of underplating or excess extrusion of lavas, the crust is still entirely the result of magma extraction from the mantle. At a minimum, 11 km crust requires 40–80% more melt delivery than 6–8 km crust. This model assumes that the normal thickness of crust is provided by 2–D flow. If along axis transportation of melt from a 20 km wide source region accounts for the crustal thickening along the rift zones (as is suggested by down–rift dike eruption events), then the melt production could easily exceed three times what is required under the Juan de Fuca ridge in general. Since the fastest spreading ridges on Earth spread at roughly three times the rate of the Juan de Fuca (17 cm/yr at southern East Pacific Rise), it is quite likely that the production of melt under Axial Volcano exceeds anything observed beneath a typical mid–ocean ridge. Qualitatively, this fits with the 11 km thick crust and the wide magma chamber, both of which exceed anything observed under ridges elsewhere. This high magma productivity beneath Axial suggests that melting should be initiated at greater depths than under normal ridge segments. This has been independently suggested by the higher Sr and lower silica saturation of Axial basalts, both indicators of deeper melting (Rhodes *et al.* 1990).

5.3 Gravity field

5.3.1 Residual gravity field

The gravity field of Axial has been examined on two very different scales. Hooft *et al.* (1995) explored crustal thickness and mantle temperature along the length of the Gorda and Juan de Fuca ridges. Their observations were based on

measurements from numerous cruises but ship track spacing limited their observations to long wavelength (>20 km) features. The free air gravity field (not shown) is dominated by bathymetric effects with a local 20 mGal high over Axial. They calculated a Residual Mantle Bouguer anomaly (RMBA) by removing from the gravity field the effects of bathymetric variation assuming a crust/water density contrast of 1.7 g/km^3, and cooling effects away from the ridge axis (fig. 5.6). The Cobb–Eickelberg seamounts dominate the gravity field but are not considered here because they formed in the absence of ridge influences.

A 50 mGal relative depression in the RMBA gravity field over Axial extends 75 km in each direction along the ridge. The results of Hooft *et al.* (1995) are based largely on this long wavelength feature. Applying relationships derived by Ito and Lin (1995), they estimate a 1.5–2.0 km thickening of the crust and a 30–40° elevation in mantle temperatures under Axial Volcano. However, the long wavelength nature of their dataset and methods would mask any local Moho relief near the volcano.

The second gravity field analysis of Axial was conducted on a local scale by Hildebrand *et al.* (1990). Sea surface and sea floor measurements were compiled to examine crustal structure within 20 km of the caldera. The regions of overlap between Hildebrand *et al.* (1990) and Hooft *et al.* (1995) show a similar gravity trough trending northwest–southeast across the volcanic edifice (fig. 5.6). Using the theory of ideal bodies (Parker 1974) and 37 seafloor gravity measurements, they identify regions of anomalous low density beneath the

caldera. In a 10 km x 10 km cube centered on the caldera, much of the underlying crust to a depth of 10 km is interpreted as having a density at least 0.15 g/cm^3 lower than the surroundings. A smaller volume, still centered on the caldera is inferred to have a density at least 0.3 g/cm^3 lower than the surroundings.

5.3.2 Density of the crustal root

The density contrast across the Moho is poorly determined in most geologic settings. Yet a knowledge of this contrast is a useful constraint on both lower crustal and upper mantle composition. A contrast of 0.5–0.6 g/cm^3 is commonly used (Hooft *et al.* 1995, Detrick *et al.* 1995) to interpret regional gravity surveys in ridge environments. However much smaller contrasts of 0.1 g/cm^3 have been identified across the Moho in Iceland (Menke 2000).

Hildebrand *et al.* (1990) examine the density contrast across the Moho in conjunction with crustal thickness beneath Axial using sea surface gravity measurements. They assume the Axial edifice is isostatically compensated by a buoyant crustal root which mirrors the bathymetry and is proportionally larger in amplitude. For a given ratio of the Moho root thickness to the volcanic edifice height, they perform an inversion of the relative gravity data to determine the corresponding density of the crust root. Since neither can be determined absolutely, they conclude with a function relating density contrast of the lower crustal root with the root–to–edifice height ratio. This function is shown in figure 5.7 as the bold black line.

Since crustal thickness is determined directly via seismic methods in this current experiment, the relationship determined by Hildebrand *et al.* (1990) can be used to estimate the crust–to–mantle density contrast. First the thickness of the crust root is estimated by removing the 1.2 km of seafloor topography from the crustal thickness measurement. This leaves 2.3 km of excess Moho topography, relative to the 8 km minimum thickness observed in this experiment. If a background crustal thickness of 6 km is assumed however, the seismic results indicate 4.3 km of crustal thickening. Combining the root thickness of 2.3–4.3 km with the volcanic edifice height of 1.2 km gives a ratio of crustal root height to edifice height of 1.9–3.6. Comparison with Hildebrand *et al.*'s results implies a crustal root density contrast of 0.11–0.20 g/cm^3 (fig. 5.7). This value is lower than is usually assumed across the oceanic Moho, implying that either the local mantle has an unusually low density or the crustal root is more dense than observed elsewhere. Both are plausible in this location. Excessive heat, the presence of melt and geochemical depletion could all work to lower the effective density of the mantle under the volcano. Heat and melt beneath the Moho are consistent with recent observations at highly productive ridges (Dunn *et al.* 2000).

The suggestion of a dense crustal root is well supported by observations at the Marquesas and Kerguelen Islands where crustal underplating by a hotspot is thought to be responsible for very high seismic velocities in the lower crust (Caress *et al.* 1995, Recq *et al.* 1990). The small density contrast implied by the

gravity model suggests similar underplating may occur at Axial. Higher mafic content entrained in the underplated region could lower the density contrast across the Moho as well. Note that this is a local observation only.

There is no evidence that a similarly small density contrast underlies the distal ends of the rift zones. Tolstoy *et al.* (1993) found significant lateral variation in lower crustal density along the mid–Atlantic ridge. They found that such density variations can partially mask a mantle Bouguer anomaly. Barth and Mutter (1996) came to a similar conclusion on the East Pacific Rise. Though crustal thickness was found to vary by 2.6 km along the ridge, the mantle Bouguer gravity signature varied by less than 10 mGal – not nearly as much as would be expected from an additional 2.5 km of crust. They also find weaker Moho seismic reflection strengths in areas of thin crust. From this they suggest that the transition zone from crust to mantle is much thicker under thinner crust. The densities in this transition zone (lower than mantle densities) offset the gravitational high expected over thin crust. Tolstoy *et al.* (1993) implicate density variations in the lower crust in a slow spreading rate regime. Barth and Mutter implicate density variations in the mantle in a fast spreading rate regime. As the Juan de Fuca has an intermediate spreading rate, and the influence of the Cobb hotspot is not clear, there is every reason to expect similar density variations along Axial and its rift zones. So while a low density root directly under the volcano is observed, this is not necessarily representative of densities along the Juan de Fuca.

5.3.3 Crustal thickness along the ridge

The observed 11 km crust under the volcano is 3 km more than predicted by the mantle Bouguer anomaly of Hooft *et al.* (1995). The limited width of the crustal root makes it difficult to observe in the gravity field. Figure 5.8 shows the anticipated gravity anomaly due to the crustal root. ("Crustal root" is defined here as the ~3 km of crustal thickening observed in the seismic analysis (fig. 5.5). It does not include the additional assumed thickening relative to standard 6 km crust.) The gravitational field is estimated by treating the root as a point mass at 11–12 km b.s.f., and calculating the mass anomaly from the root's ~310 km^3 volume. A crustal root density anomaly of 0.1–0.2 g/cm^3 will only generate a gravity signature of 2–4 mGal, smaller than the noise level of the regional gravity study (>5 mGal). The crustal root is essentially invisible from regional observations. The seafloor gravity survey of Hildebrand *et al.* implied Moho topography but was unable to constrain the excess thickness. In short, the seismically–observed Moho is fully consistent with the observed gravity. Though the latter does not predict the crustal root, this analysis demonstrates specifically that it should not.

This root must be an additional feature superimposed on the crustal thickening observed in the gravity. Within 20 km of the summit, the crustal thickness is constrained seismically but variations are largely invisible to the regional gravity survey. Beyond 20 km in either direction, the Moho is not seismically constrained but a broad region with 1.5–2.0 km or more of excess crust is predicted by the gravity, depending on the assumed density structure. Combining these

observations gives the Moho topography in figure 5.9.

5.3.4 Isostatic observations

The gravity studies of Hildebrand *et al.* (1990) and Hooft *et al.* (1995) are combined with the seismic results to create a working model of the crust along the central portion of the Juan de Fuca ridge. The regional thickening inferred by Hooft *et al.* relies on assumptions about the density contrast across the Moho. A similar crustal structure can be inferred *without* relying on this study however by comparison to standard models of oceanic crust. The thinnest crust observed seismically under Axial is ~8 km, much thicker than most oceanic crust. At some distance away from the volcano the crust likely thins to typical values of 6 km. This implies about 2 km of crustal thickening centered on Axial not including the seismically observed bump. This estimation is in agreement with, and completely independent of the results of Hooft *et al.* (1995).

The shape of this crust can be used to further constrain the density contrasts across Moho. Figure 5.9 shows the relative weight of the excess mass above and below a 6 km crust (Δdepth*$\Delta\rho$ in km*g/cm^3). This figure is misleading because the masses are sensitive to the arbitrary datums at 0 and 6 km depth. However the *slope* of the mass curves depend only on the density contrasts. Assuming Airy isostatic compensation of the long wavelength features, the ideal lower crustal density contrast (relative to the mantle) will give the best fit between the topographic mass excess and the lower crustal mass excess, not including a static offset.

Using upper crust density contrasts of 1.4–1.7 g/cm^3 (relative to sea water at 1.0 g/cm^3), crustal root density contrasts of 0.1–0.2 g/cm^3 (relative to mantle), the best fitting lower crustal density contrasts range from 0.38 to 0.53 g/cm^3. Several factors could introduce error near the volcano including melt in the crust, thicker layer 2A, and error in the root shape. However, the predicted density range varies little even if the points within 10 km of the summit are excluded from the model.

The isostatic analysis shows that the very low density contrast determined independently for the crustal root is a local feature. Errors associated with the isostatic calculations are large due to the assumption of normal 6 km crust and/or the density assumptions of Hooft *et al.* (1995). Even with a wide margin of error however, the inferred regional density contrast across the Moho of 0.38–0.53 g/cm^3 is significantly larger (200–400%) than the 0.1–0.2 g/cm^3 of the root. This is further evidence that underplating and/or partial melt in the mantle are most significant within ~10–20 km of the summit. We interpret this as more support for a narrow zone of high magmatism under the volcano.

5.4 The Cobb hotspot

5.4.1 Mantle refracted (Pn) phases

A mantle refracted Pn phase was observed sporadically in this experiment (example fig. 3.3). Though the shot–receiver geometry explicitly included long

offsets with the hope of collecting Pn data, only 5% of the shots with suitable range had a Pn phase identifiable above the noise level. These 343 Pn picks constitute only 9 separate segments of the refraction lines. Pn phases have been recorded and used successfully in the ridge environment. Despite the large volume airgun array and ideal geometry used here, the Pn data is disappointing, but not surprising. The thick crust identified in this chapter significantly increases the effects of geometric spreading. Instead of emerging as a first arrival at 20 km, as is often seen in 6 km crust, Pn near Axial emerges beyond 40 km. This means fewer, weaker Pn phases. A second limiting factor is the high attenuation due to melt in the crust, identified in chapter 4. Thick attenuating crust decreases the energy of a phase as it propogates to and from the mantle. From the crustal and Moho studies, it is clear in hind sight why Pn was observed in so few places.

Tomographic inversion of the Pn data for upper mantle structure is not feasible based on only 9 observations. However, analysis of the Pn apparent velocities can determine average mantle velocities. Because of traveltime errors associated with the water column, apparent velocities are calculated from the slope of the Pn arrivals in lieu of their absolute traveltime. This approach is insensitive to static time errors. Apparent velocities are estimated as the reciprocal of the best fit slope to traveltime picks plotted as a function of shot–receiver range. Error due to bathymetry under the shots is minimized by applying a correction based on the water depth under the shot position. The assumption of subvertical raypaths through the water column is based on calculated Pn take–off angles of $< 10°$, resulting in horizontal seafloor entry errors of ~300

meters.

The apparent velocity estimates assume a flat Moho. Correction for the observed Moho topography is performed by estimating the 2–D Moho dip between the Pn entry and exit point. This dip is estimated as the Moho slope between source and receiver. Away from the caldera, where the Moho is not constrained by the PmP analysis, a crustal thickness of 8 km is assumed. In the dipping layer model, the true mantle velocity (v_m) is related to the observed (dipping) velocity (v_o) as:

$$v_m = v_c / (\sin[\sin^{-1}(v_c/v_o) + \theta])$$

where θ is the slope of the Moho from source toward receiver and v_c is the velocity of the lower crust.

5.4.2 Seismic velocities of the upper mantle

Figure 5.10 shows estimated Pn apparent velocities after application of the bathymetry and Moho corrections. The largest source of error is the traveltime slope estimation from the picks themselves. An estimated pick error of 0.03 s (4 samples) translates into apparent velocity errors of 0.1–1.5 km/s depending on the number of traces on which the Pn phase is observed and rms fit of the picks to a straight line (fig. 5.10). Error in the Moho dip, estimated as ± 5 degrees translates into an upper mantle velocity error of ± 0.25 km/s. While the estimated error explains much of the scatter in mantle velocities, it renders the estimates useless for all but the most cursory interpretation. Overall, the upper mantle

velocities are similar or slightly higher than other similar studies (Menke *et al.* 1998 , Dunn *et al.* 2000). We rule out the presence of mantle melt on a regional scale which would require velocities slower by nearly 1 km/s. This is no surprise since the Pn observations are largely off–axis (fig. 5.11) where melt is not expected. No geographic pattern has been found in the mantle velocities (i.e. systematic slowness near the rift zones or summit), partially due to the absence of measurements near the neovolcanic zones. The attenuation due to melt and the thicker crust, as well as shot geometry, make it particularly hard to sample the region under the caldera. No obvious anisotropic trend is found. The two lowest measurements are 7.7 km/s perpendicular to the ridge axis and 7.5 km/s along the ridge axis.

The only correlation of observed mantle velocities is with Pg/Pn cross over distance and source–receiver range – larger apparent velocities occurring at shorter offsets (fig. 5.12). The velocities exceeding 8.5 km/s are suspect because they exceed typical upper mantle values. However, the correlation is strong even allowing for large velocity errors. Since apparent velocities are calculated from traveltime slope, not absolute traveltime, they are protected against timing and location errors. Model error could introduce bias through the bathymetry and Moho corrections. However the trend exists regardless of whether the corrections are used.

The Pg/Pn cross over distance is a proxy for crustal thickness in a 1–D structure. In thinner crust, Pn emerges as the first arrival at closer range. Though a dipping

Moho will shift the cross over distance, the effect is opposite of the observed correlation. That is, an interface that slopes up from source to receiver will increase both the apparent velocity and the Pg/Pn cross over distance. The correlation in figure 5.12 is negative.

The apparent velocities of the upper mantle suggest that higher velocities are observed under areas of thinner crust. Since crustal thickening is the result of excess magmatism in the upper mantle, this data suggests that the mantle, under areas of thicker crust, is seismically slower due to temperature, chemical depletion or the presence of melt.

It is important to note this analysis is independent of the crustal velocity model, except for the small Moho dip correction in the bottom panel. Errors cannot propogate from the tomography or crustal thickness into the apparent velocities. However, other factors, such as out of plane Pn propagation must be addressed before the correlation of crustal thickness and mantle velocity can be confirmed or quantified.

5.5 The role of ridge and hotspot

5.5.1 Chemical heterogeneity in the mantle

The concept of mantle heterogeneity has been used frequently to explain variations in basalt chemistry near Axial (Embley *et al.* 2000) and along several ocean ridges. The rationale is simplistic. Chemical trends which cannot be

explained by processes in the crust or on the seafloor, such as variations in trace element composition or isotope ratio, are attributed to their mantle source.

Despite this heterogeneity, Axial consistently erupts lavas with remarkably consistent chemistry (Rhodes *et al.* 1990). This has led several studies to suggest that significant mixing occurs in the crustal magma chamber to smooth the variation inherent in the mantle source. The mechanics of mixing are not known, largely because the geometry of melt distribution is poorly understood. Though the tomographic images presented here do not reveal the small scale distribution of melt, they put bounds on the absolute amount of magma contained beneath the volcano. The greatest possible mixing would occur if the entire mid–crustal volume of 2.5–6 km^3 is well–connected and convectively active. As there is little evidence to support this idea, any true mixing probably occurs on a smaller scale or perhaps at other locations in the system such as in surface–feeding dikes.

The simple model presented here explores the effects of mixing in a magma chamber as illustrated in figure 5.13. The model assumes the mantle contains equal volumes of chemically distinct magmas. These units are randomly added to a crustal magma reservoir quantified by its mixing volume, that is, the volume of melt which is actually involved in any mixing. When a new batch of magma is added to the mixing volume, it mixes instantaneously. The new composition of the melt is determined by averaging the old chemistry and the new (absolute content, not ratios) as a function of the their total volumes. A volume is removed

(erupted) from the reservoir to bring the mixing volume back to its prescribed mixing volume. By running this model through a few thousand iteration, the probability distribution of the eruptive chemistry can be determined.

This magma erupted from the mixing reservoir in this model can be compared to the products of the magma chamber at Axial. Within the limitations of the assumptions stated above, the model places bounds on the amount of mixing that is possible in a crustal magma reservoir. As an example, we use Sr/Zr to Zr composition from samples of Rhodes *et al.* (1990). The input mantle chemistries are represented by the regional samples from the flanks, rifts and areas surrounding Axial (fig. 5.14). We assume basalt samples from the caldera are the products of the magma chamber. The volume of the magma chamber in the model is taken as the lower bound on melt content beneath Axial – 5 km^3. The contours show the 2σ probability distribution function (containing 95% of all samples) for a mixing volume of 5.0 km^3 with mantle variation on the scale of 0.05, 0.5, 5.0 km^3 (0.05 km^3 is the inner contour). Large scale mantle heterogeneity requires a larger mixing volume. Since the largest possible mixing volume is the total volume of melt (5–11 km^3), there is an upper bound on the size of discrete homogeneous units of magma input to the reservoir. For this model and set of inputs, it is likely that the Sr/Zr compositions observed regionally vary, at a minimum, on a scale of 0.5 km^3, and possibly much smaller.That is, mixing in the magma chamber can not smooth variations enough to match observed chemistries unless the chemical variation in melt from the mantle varies on a scale of 0.5 km^3 or smaller.

5.5.2 Summary of mantle observations

Several observations of this project support the notion that Axial Volcano is underlain by an unusually prodigious magma source:

- large volume on melt in mid−crust (low velocity zone)

- thicker extrusive layer near volcano (depressed shallow velocities)

- crust up to 11 km thick (deeper PmP reflections)

- underplating or highly mafic lower crust (low dens. contrast in root)

- high mantle temperatures (implied by thicker crust)

- excess melt supply (implied by thicker crust)

- possible low velocities under thicker crust (Pn correlation)

While many of these features are not surprising, they confirm that the mantle under Axial is different than along other parts of the ridge. Perhaps most telling is the predominance of radial symmetry. The magma reservoir, excess extrusives and the crustal thickening are roughly circular, as opposed to linear, features. This implies that a local mantle anomaly, instead of a wide sheet−like feature, provides magma to Axial which is then redistributed along the rift zones. The down−rift diking implied by morphology and observed in 1998, is wholly consistent with the new observations.

The narrow width of the crustal root implies that the strongest influences of the Cobb hotspot are localized under a single volcano. The narrow (~20 km) root and the broader 100+ km keel likely result from two different mechanisms. The

narrow, less dense root, appears to be the result, at least in part, of underplating. The broad crustal thickening identified by Hooft *et al.* has a more typical density contrast. Instead of underplating, this extra thickness may result from a simple excess of magma production. The impact of the Cobb hotspot is fundamentally different than the hotspot under Iceland, for example, where the massive plume influence extends 100s of kilometers away from the center. Axial may represent the small hotspot endmember on the spectrum of ridge–hotspot interaction.

Hooft *et al.* estimate the mantle temperature anomaly under Axial as 30–40° based on the model of Ito and Lin (Ito and Lin 1995, Hooft *et al.* 1995). Their model defines a direct relationship between mantle temperature anomaly and crustal thickness for hotspot influenced ridges. Since this model comes from examination of Iceland, the Azores, the Galapagos, Tristan and Easter Island, it is not clear if their conclusions fit the smaller Cobb hotspot. If they do, then the 5 km crustal thickening determined here may imply temperatures elevated by much more than 30–40° in order to achieve high enough magma flux to create the crustal thickness.

5.5.3 Tectonic evolution of a hotspot–ridge interaction

The large melt content and very thick crust under the volcanic edifice should be sufficient warning against interpreting the Axial system from the traditional ridge paradigm. For example, the magma reservoir should not be included in studies of spreading rate vs. magma chamber depth. Magmatism and the likely presence of melt on the adjacent CoAxial segment show that the north rift zone

is not accommodating the full 6 cm/yr spreading required along the Juan de Fuca. Perhaps the neovolcanic zone at Axial should best be thought of as a rifting volcano.

Axial forms an important link in our understanding of how ridges are born. The limited spreading across Axial, young age estimates (Hammond and Delaney 1985) and offset location in the current magnetic anomaly indicate that the flanks of Axial sit on pre–existing crust. As the hotspot moved under its current position, heat and melt in the mantle penetrated the crust eventually erupting and forming a small seamount. Its proximity to the ridge imposed relative tension on an otherwise radial stress field. While the melt supply remained localized, rifting in the crust began to distribute magma in dikes perpendicular to the axis of minimum stress. As the rift system began accommodating strain, passive spreading started to shut down on the nearby ridge segments.

This is Axial today. The volcano is rifting, unlike typical northeast Pacific seamounts. But it has not yet transitioned into a proper ridge segment. It is still fed by focused magmatism from the hotspot. Geodetic measurements should help determine how much of the spreading has shifted to Axial. Geochemical studies may be able to track the growth into ridge if the hotspot's lack of distinct chemistry can be overcome. Morphologic and seismic investigations of the Vance and CoAxial segments will determine the degree to which they are still active.

A glimpse of the future may be provided by a split volcano on the East Pacific Rise at 15°40' N (fig. 5.15). A recent study suggests that spreading jumped 7–10 km west and bisected a pre–existing volcano (Carbotte *et al.* 2000). Now the remnants of this volcano can be seen straddling the ridge axis. Perhaps this rifted volcano, on a fully established ridge, is what Axial will look like in the future.

As the Cobb hotspot and the axis of the Juan de Fuca ridge continue to converge, they can only become further indistinguishable. As the old ridge segments shut down and spreading shifts entirely to what is now Axial's rift zones, perhaps a new "Axial segment" of the Juan de Fuca will come into its own and significant spreading will occur across the volcano and its rift zones.

Barth, G. A., and J. C. Mutter, Variability in oceanic crustal thickness and structure; multichannel seismic reflection results from the northern East Pacific Rise, *J. Geophys. Res., 101*, 17,951–17,975, 1996.

Carbotte, S. M., A. Solomon, and C. G. Ponce, Evaluation of morphological indicators of magma supply and segmentation from a seismic reflection study of the East Pacific Rise 15 degrees 30'–17 degrees N., *J. Geophys. Res. 105,* 2737–2759, 2000.

Caress, D. W., M. K. McNutt, R.S. Detrick, J. C. Mutter, Seismic imaging of hotspot–related crustal underplating beneath the Marquesas Islands, *Nature, 373,* 600–603, 1995.

Cudrak, C. F., and R. M. Clowes, Crustal structure of Endeavour Ridge segment, Juan de Fuca Ridge, from a detailed seismic refraction survey, *J. Geophys. Res. 98,* 6329–6349, 1993.

Detrick, R. S., H. D. Needham, and V. Renard, Gravity anomalies and crustal thickness variations along the Mid–Atlantic Ridge between 33 degrees N and 40 degrees N., *Geophys. Res., 100,* 3767–3787, 1995.

Dunn, R.A., D.R. Toomey and S.C. Solomon, Three–dimensional seismic structure and physical properties of the crust and shallow mantle beneath the East Pacific Rise at 9°30'N, *J. Geophys. Res., 105,* 23,537–23,555, 2000.

Embley, R. W., W. W. Chadwick, Jr., M. R. Perfit, M. C. Smith, & J. R. Delaney, Recent eruptions on the CoAxial segment of the Juan de Fuca Ridge: Implications for mid–ocean ridge accretion processes, *J. Geophys. Res.105,* 16,501–16,525, 2000.

Foulger, G. R., and D. R. Toomey, Structure and evolution of the Hengill–Grensdalur volcanic complex, Iceland: Geology, geophysics and seismic tomography, *J. Geophys. Res., 94,* 17,511–17,522, 1989.

Hammond, S. R., and J. R. Delaney, Evolution of Axial Volcano, Juan de Fuca Ridge, *Eos. Trans. AGU., 66,* 925, 1985.

Hildebrand, J. A., J. M. Stevenson, P. T. C. Hammer, M. A. Zumberge, R. L. Parker, and C. G. Fox, A seafloor and sea surface gravity survey of Axial Volcano, *J. Geophys. Res., 95,* 12,751–12,763, 1990.

Hooft, E. E. E., and R.S. Detrick, Relationship between axial morphology, crustal thickness, and mantle temperature along the Juan de Fuca and Gorda Ridges, *J. Geophys. Res., 100,* 22,499–22,508, 1995.

Hooft, E. E. E., R. S. Detrick, D. R. Toomey, J. A. Collins, and J. Lin, Crustal thickness and structure along three contrasting spreading segments of the Mid–

Atlantic Ridge, 33.5 degrees –35 degrees N., *J. Geophys. Res., 105*, 8205–8226, 2000.

Ito, G., and J. Lin, Oceanic spreading center–hotspot interactions; constraints from along–isochron bathymetric and gravity anomalies, *Geology, 23,* 657–660, 1995.

Menke, W., M. West, B. Brandsdottir, and D. Sparks, Compressional and shear velocity structure of the lithosphere in Northern Ireland, *Bull. Seis. Soc. Am., 88,* 1561–1571, 1998.

Menke, W., Crustal isostacy indicates anomalous densities beneath Iceland, *Geophys. Res. Lett. 26,* 1215–1218, 1999.

Parker, R. L., The theory of ideal bodies for gravity interpretation, *Geophys. J. R. Astron. Soc., 42,* 315–334,1975.

Recq, M., D. Brefort, J. Malod, and J. L. Veinante, The Kerguelen Isles (southern Indian Ocean); new results on deep structure from refraction profiles, *Tectonophys.,182,* 227–248, 1990.

Rhodes, J. M., C. Morgan, & R. A. Liias, Geochemistry of Axial Seamount lavas; magmatic relationship between the Cobb hotspot and the Juan de Fuca Ridge, *J. Geophys. Res., 95,* 12,713–12,733, 1990.

Sohn, R.A., S. C. Webb, J. A. Hildebrand, and B. D. Cornuelle, Three–dimensional tomographic velocity structure of upper crust, CoAxial segment, Juan de Fuca Ridge; implications for on–axis evolution and hydrothermal circulation, *J. Geophys. Res. 102,* 17,679–17,695, 1997.

Sohn, R. A., Crawford, W.C., and S. C. Webb, Local seismicity following the 1998 eruption of Axial Volcano, *J. Geophys. Res., 26,* 3433–3436, 1999.

Staples, R. K., R. S. White, B. Brandsdottir, W. Menke, P. K. H. Maguire, and J. H. McBride, Faroe–Iceland Ridge experiment; 1, Crustal structure of northeastern Iceland. *Geophys. Res.,* 102, 7849–7866, 1997.

Tolstoy, M., A. J. Harding, and J. A. Orcutt, Crustal thickness on the Mid–Atlantic Ridge; bull's–eye gravity anomalies and focused accretion, *Science, 262,* 726–729, 1993.
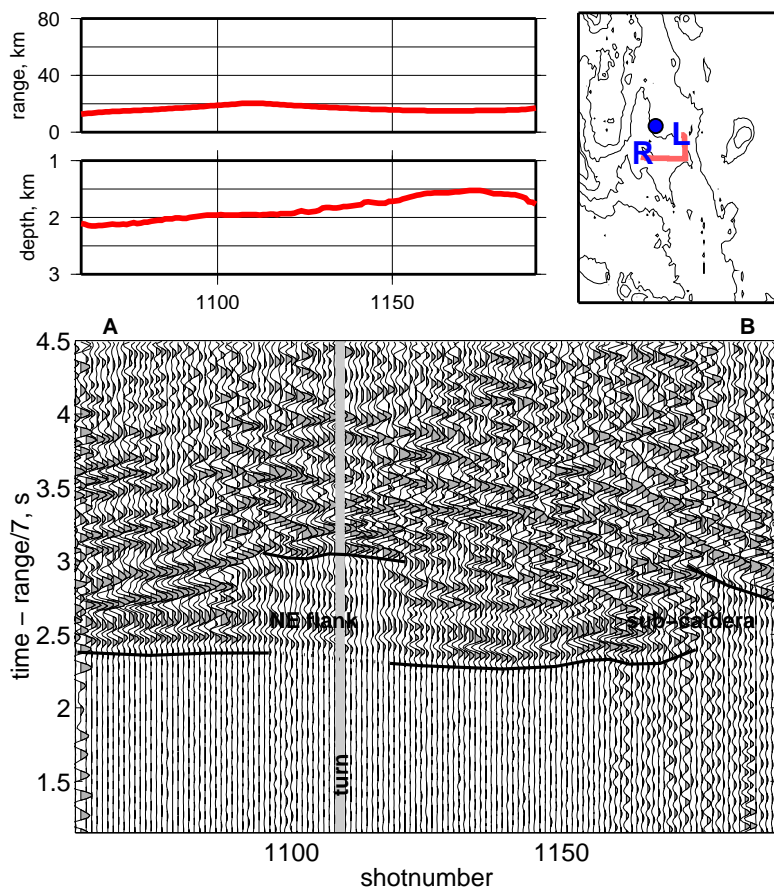
Figure 5.1 Evidence for the northeast flank low velocity anomaly. This record shows shadow zones from two separate features, each with large amplitude delayed arrivals of ~0.5 s. The feature near the turn can be constrained to the east of the caldera while the shadow at the right side of the record is clearly associated with the caldera region.

Figure 5.2 The depth distribution of the northeast flank velocity anomaly. Note velocity perturbations barely exceed 1.0 km/s though a large area is slow by 0.5 km/s
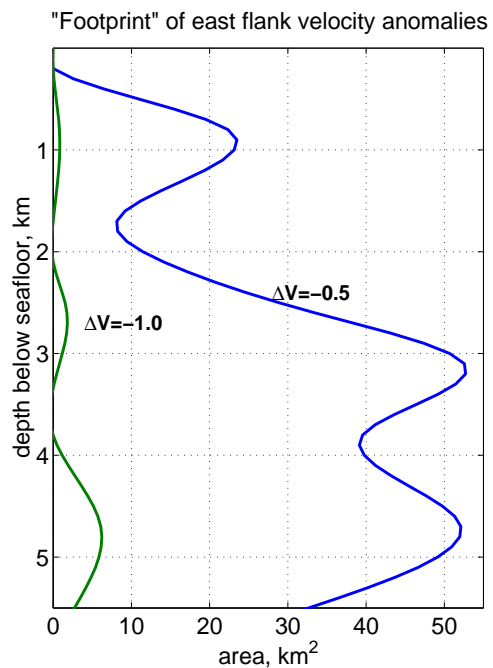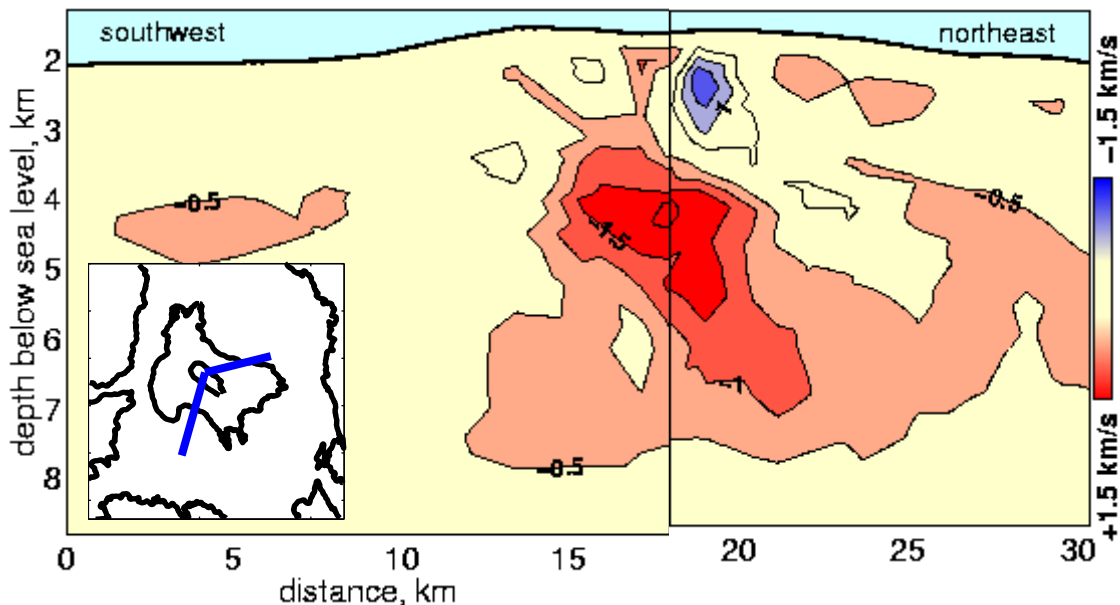
Figure 5.3 Cross section of the caldera, northeast flank and southwest rift low velocity anomalies. The northeast anomaly may be connected at depth to the central caldera low velocity zone. The southwest rift feature does not appear connected. The caldera anomaly is far greater in amplitude than the adjacent features. (Typo in figure. red is negative 1.5 km/s, blue is positive)

Figure 5.4 Depth distribution of southwest rift zone anomaly. The anomaly lacks the large perturbations (> 1 km/s) observed elsewhere and is limited in depth. It does not appear to have a deeper crustal root.
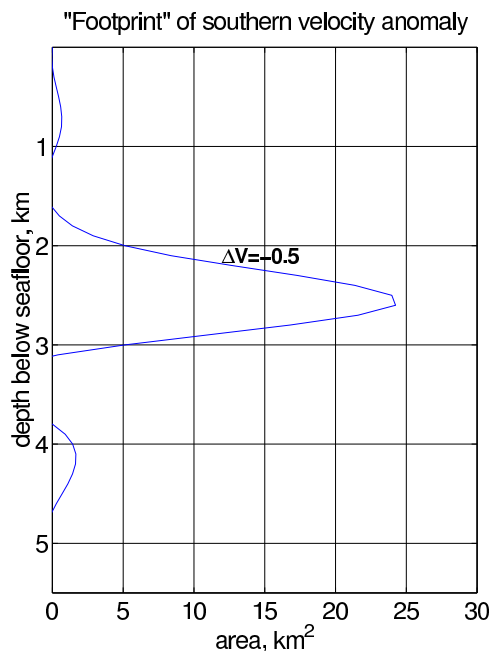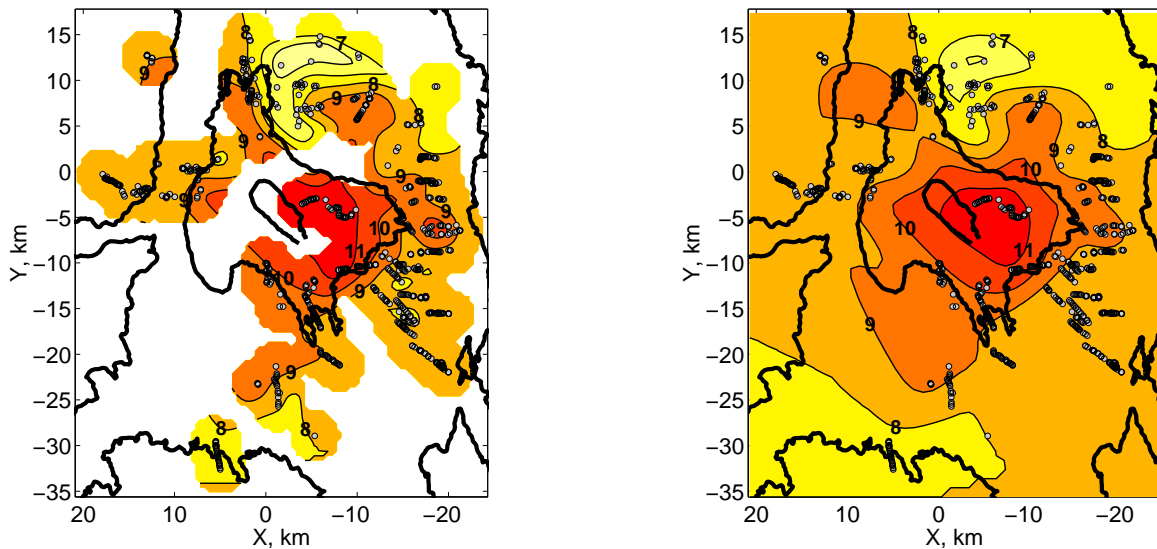
Figure 5.5 Crustal thickness from PmP phases. The **left** panel shows the areas of the model where the Moho depth is constrained. Moho "bounce points" of PmP phases are marked as circles. The **right** panel shows a smooth interpolated view which crudely fills in the surrounding area assuming a background crustal thickness of eight km. From either panel, crustal thickening appears to mirror closely the overlying seafloor topography. The crustal thickness should not be confused with Moho topography. Though most of this thickening is the product of a deeper Moho, ~ 1.4 km of the thickening is due to topside topography.
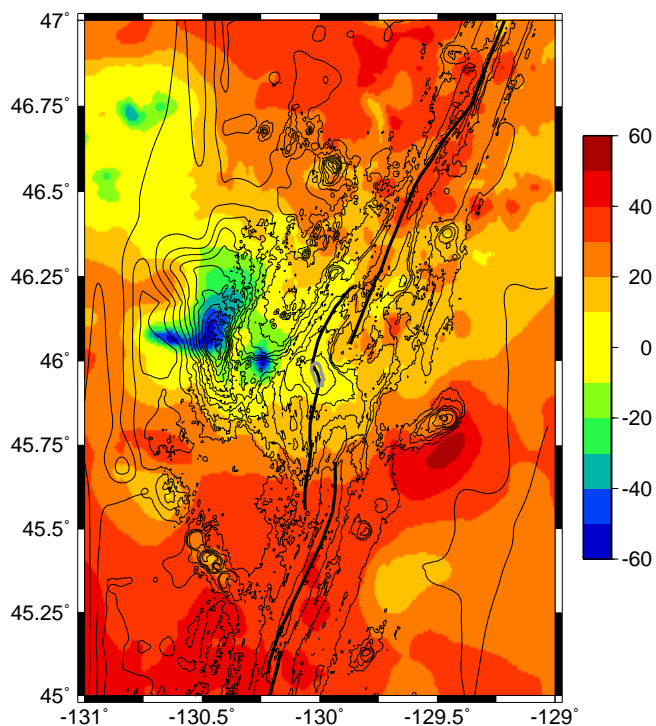
Figure 5.6 Residual Mantle Bouguer Anomaly (Courtesy of Hooft *et al.* (1995)). The free air gravity field (not shown) is dominated by the topography. All different versions of Bouguer anomaly show a similar low centered on Axial. Gravity has been contour shaded at 10 mGal intervals. Regional bathymetry contours have been overlain on the gravity. Ridge segments and caldera are superimposed as well.

Figure 5.7 Modified from Hildebrand *et al.* (1990) figure 13. Black line marks Hildebrand *et al.*'s trade off between crustal root density and topside to bottomside "topography". Relation was derived from inversions of well sampled sea surface gravity within ~20 km of the caldera. Their gravtiy field is not shown though it is similar to the Axial region as determined by Hooft *et al.* (1995) in figure 5.7.
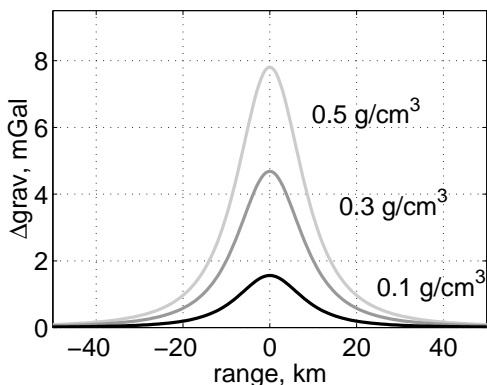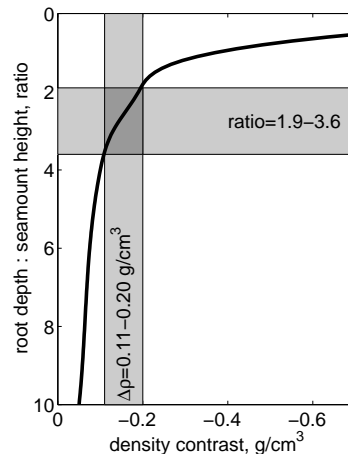
Figure 5.8 Gravity anomaly at sea level due to crustal root of different densities. Volume of root is estimated from crustal thickness. Given the 5 mGal nominal error in the regional RMBA gravity, the crustal root is largely undetectable from long wavelength analysis, especially for the estimated density contrast of 0.1–0.2 g/cm^3.

Figure 5.9 Isostatic estimate of Axial to constrain the density contrast of the "extra" lower crust, not including the seismically determined crustal root. **Top panel** shows parameters. **Bottom panel** shows lower crust mass anomaly (gray) for several densities. Best fit lower crustal density contrast is solid black line. Range of values given in text. Crustal density contrasts are negative w.r.t. mantle.
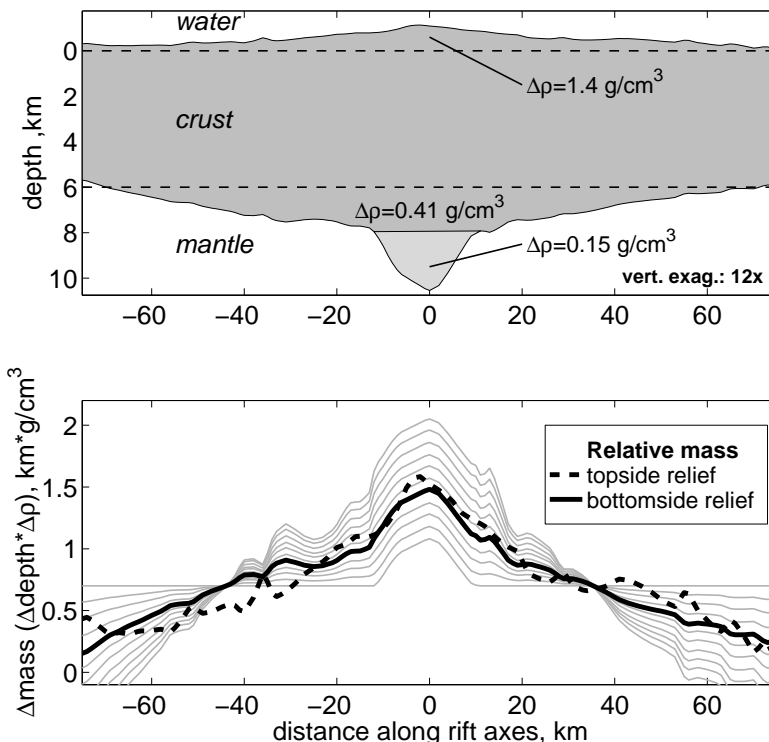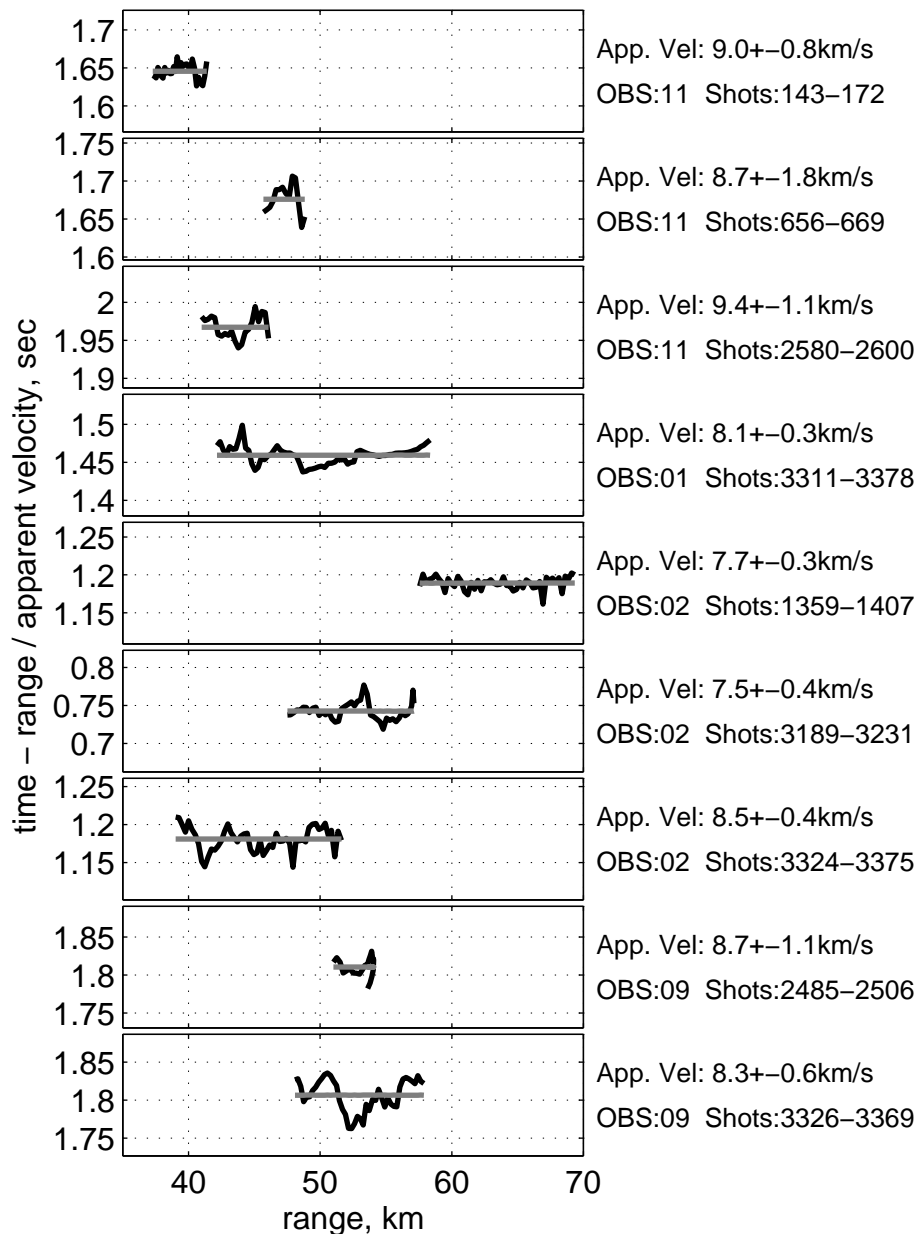
Figure 5.10 Apparent Pn velocities with errors measured for nine distinct Pn observations. Traveltime picks are in black. Gray line is the least squares best estimate of the slope. Times are reduced by the observed apparent velocity. No bathymetry or Moho dip corrections have been applied to the figure. Such corrections have been included in the estimated velocity. Note the different ranges at which Pn is observed.

Figure 5.11 Approximate section of mantle sampled by each Pn observation. Corresponding apparent velocities are labeled. No clear geographic trend is observed.
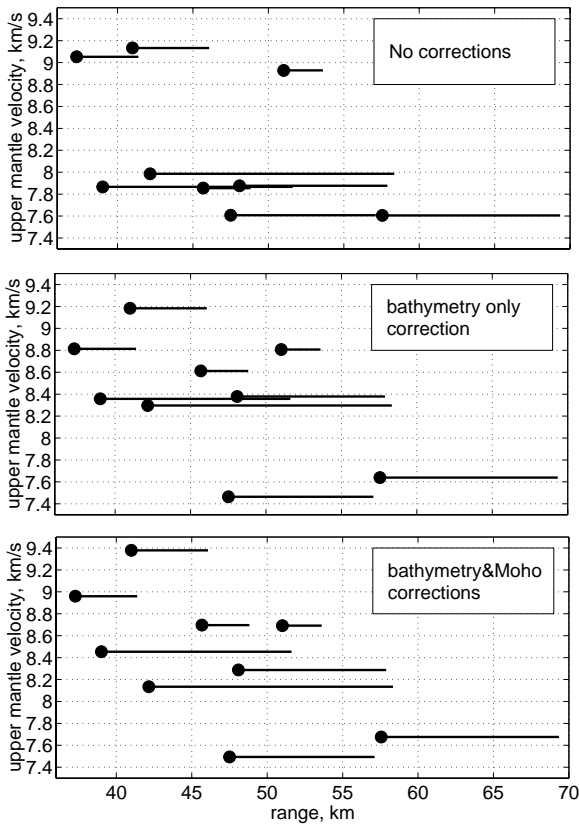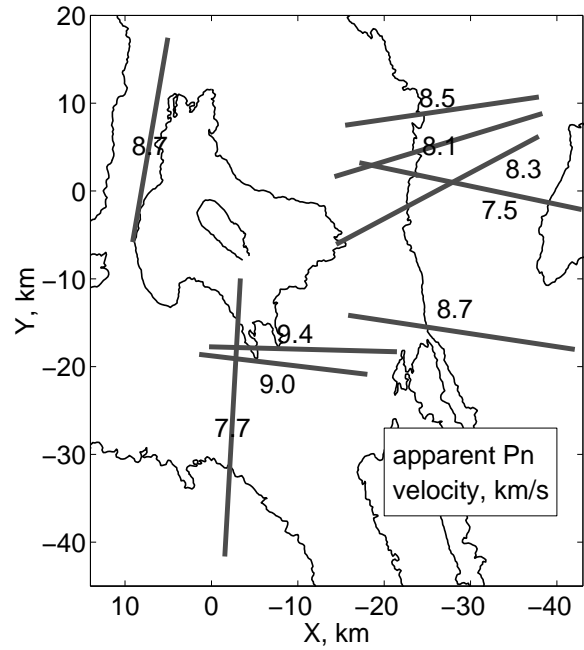
Figure 5.12 Correlation of apparent velocity and cross over distance (rough proxy for crustal thickness). Lines mark the range of observed Pn phases. Solid dots mark the approximate Pg/Pn cross over distances. The trend is seen in the raw velocities and after corrections for bathymetry and Moho dip. Though the effect of Moho dip on the cross over distance is not accounted for, it would only amplify the trend observed here.
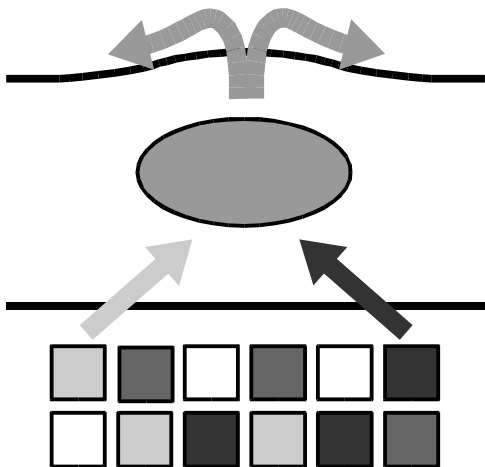
Figure 5.13 Schematic of magma mixing model. Equal volume heterogeneous volumes of melt are added to the mixing volume. This volume is continually "mixed" and magma is removed to maintain constant volume. The products, at top, are a smoothed version of the input chemistries. While this model is realistic, the size of the effective mixing volume is unknown. There is little reason to believe that magma is mixed throughout the magma chamber. However, the size of the magma chamber places an upward limit on the mixing volume.

Figure 5.14 Modified from Rhodes *et al.* (1990). Data points are basalt samples from Rhodes *et al.* Crosses are regional samples from the flanks and rift zones around Axial. Circles are samples from the caldera. Caldera samples show much less variation in Sr/Zr to Zr composition. In the mixing model, regional samples are considered a proxy for the range of variation found in the mantle. The caldera samples are taken to represent the mixed output of the reservoir. The contours show the 2σ range of variation expected from a mixing volume of 5km^3. The inner contour marks homogenous mantle volumes of 0.05 km^3, the middle contour is 0.5 km^3, and the outer contours marks 5.0 km^3 mantle volumes.
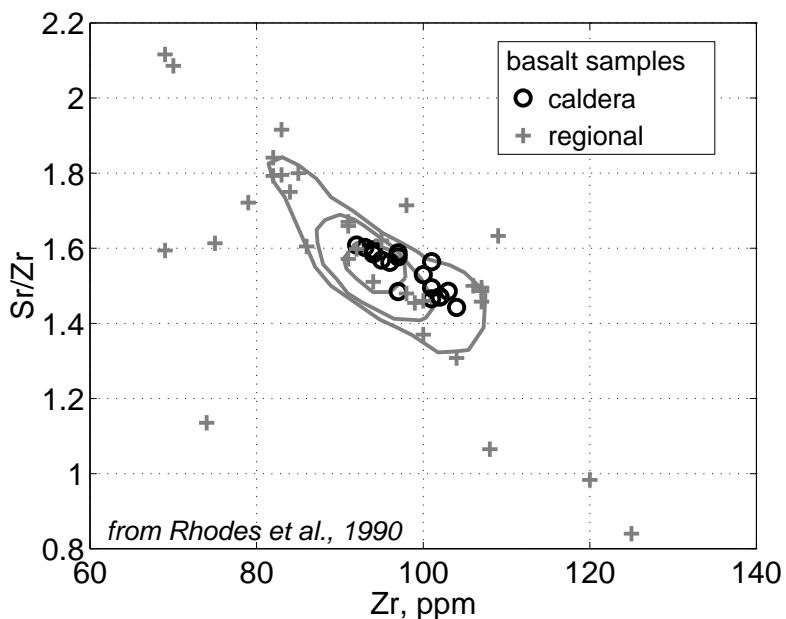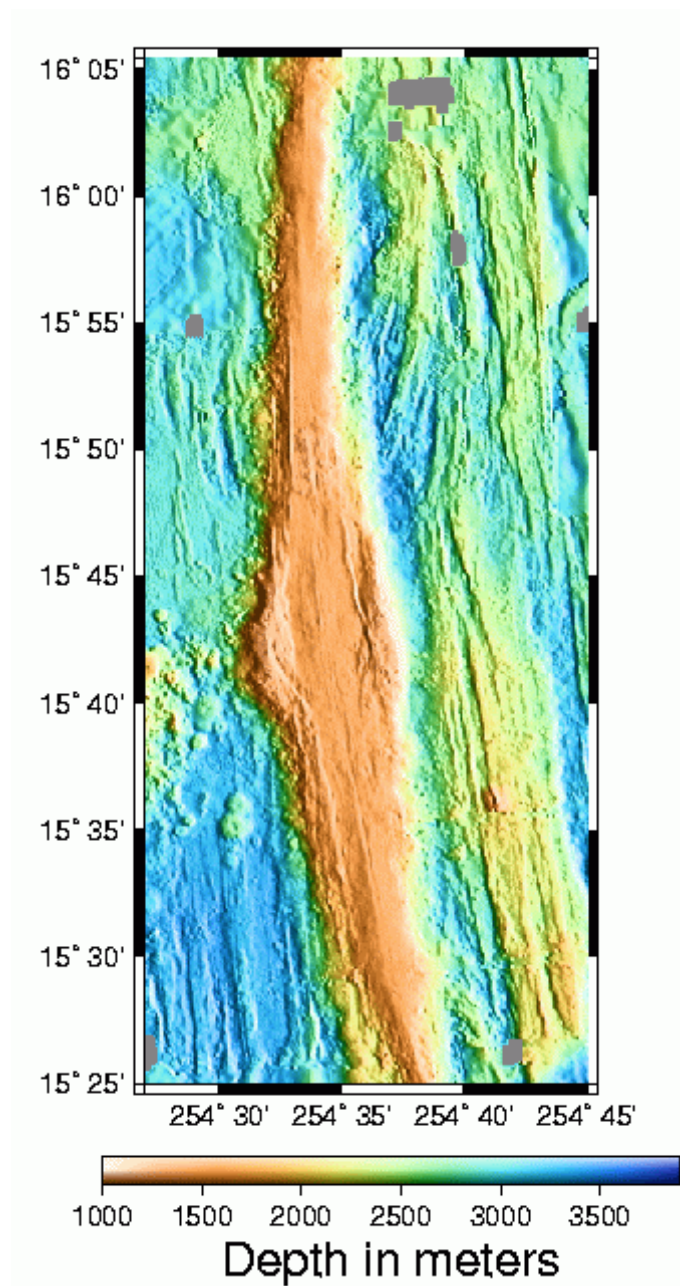
Figure 5.15 From Carbotte *et al.* 2000. Ridge axis of East Pacific Rise. The high ridge is the current axis of spreading. A paleo–ridge is visible ~5' to the east of the axial high. Carbotte *et al.* interpret this morphology as a westward ridge jump of 7–10 km within the past 100 kya. A wider section of ridge at 15°42' N is in–line with off axis seamounts to the west. This is interpreted as a volcano which was split by the ridge jump. Perhaps this volcano was associated with the first volcanic activity on the new ridge segment. If this is the case, it may loosely represent the future at Axial.

Appendix: Shallow crustal magma chamber beneath the axial high of the Coaxial Segment of Juan de Fuca Ridge at the "Source Site" of the 1993 eruption

William Menke, Michael West, Maya Tolstoy, Spahr Webb and Rob Sohn

(to be submitted)

Summary

Seismic imaging reveals a shallow crustal magma chamber beneath the Source Site of the 1993 eruption on Coaxial Segment, Juan de Fuca ridge. The magma chamber is at least 6 km3 in volume and contains at least 0.6 km3 of melt, enough to supply at least several eruptions of size equal to the one in 1993. No mid–crustal connection of this magma chamber with the magmatic plumbing of nearby Axial volcano (the current expression of the Cobb–Eickelberg hot spot) is evident, confirming previous geochemical and geological studies that argued against mixing between the two. The lack of connectivity implies that magma transport though the uppermost mantle and lower crust are very highly focused into narrow (<5 –10 km) conduits.

The Coaxial Segment of the intermediate–spreading Juan de Fuca Ridge extends from about 5 to about 80 km north from the summit caldera of Axial volcano, the most recent of the Cobb–Eickelberg chain of volcanoes (fig app.1). Coaxial Segment occupies an en echelon position with respect to the North Rift

of Axial. Magmatism and resulting crustal accreation of the North Rift and Axial overlap for about 15 km. This area is one in which both ridge and hot spot processes are occurring in very close proximity.

Both Axial and Coaxial have experienced recent volcanic eruptions. In 1993, a dike propagated from a bathymetric high (the so called "Source Site", at 46:10N) near the southern end of Coaxial Segment to a distance of about 40 km to the north (Butterfield et al. 1997, Embley et al. 2000). In 1998, a dike propagated from near the Axial caldera to a point about 50 km to the south (Dziak and Fox 1999). The propagation of both dikes were monitored by tracking the numerous microearthquakes that they caused by hydroacoustic means (Dziak and Fox 1999, Fox et al. 1995). The 1998 eruption caused 3 m of subsidence of the Axial caldera (Fox 1999), and is believed to be associated with a central magma chamber beneath that volcano. Geological mapping of lava flows along Coaxial and their chemistry, which is distinct from Axial basalts, have been used to argue that the source of the Coaxial lavas is distinct from the Axial magma chamber (Embley et al. 2000). Here we use seismic imaging to show that these inferences are correct, and to argue that the 1993 eruption most likely originated in a shallow crustal magma chamber located beneath the Source Site. This magma chamber is distinct from, and apparently unconnected to, the Axial magma chamber.

The data that we present here is from a 1999 active seismic experiment that was primarily focused on imaging the Axial magma chamber. About 5000 shots from

Research Vessel Ewing's airgun array (20 guns totaling 142 l) were recorded on six ocean bottom seismometers (OBS's) (Webb 1998) deployed on the volcano's flanks. Water wave traveltimes and Global Positioning System determined shot locations were used to precisely locate the OBS's on the sea floor (error <20 m) and to determine clock drifts (error < 0.02 s). The dense record sections permitted the identification of the major compressional waves, including the crustal turning Pg, Moho reflected PmP and mantle refracted Pn. Although many lines of shots were recorded during this experiment, four lines in particular, recorded by two OBS's located just north of Axial, are relevant to this discussion of Coaxial Segment.

Line 1 crosses the Coaxial Segment Source Site at 46:11N. A distinct shadow zone and delayed Pg arrivals (by 0.1–0.3 s) are evident on record sections from both OBS 1 and 2, at source–OBS ranges of 14–20 km (fig. app.2, bottom). These features occur at just those positions along Line 1 where the Pg waves pass beneath the Source Site. We infer that the Pg waves are interacting with a low compressional velocity zone (LVZ) associated with a magma chamber at that location. In order to accept this interpretation, the possibilty that the delayed arrivals are actually deeper PmP Moho reflections must be discounted. A record section from Line 2 to OBS 2, which has Pg waves that miss Coaxial Segment, provides the necessary evidence (fig. app.2, top right). No shadow zones or delayed arrivals are evident on this line, even though it has the same source– OBS ranges (5–20 km) as Line 1. PmP reflections are seen on record sections (not shown) for Line 4 to OBS 1, which sample crust to the east of Coaxial

Segment. These reflections start at about 25 km range (corresponding to a crustal thickness of about 8 km), suggesting that confusion of PmP with delayed Pg with ought not to be a problem for Line 1's shorter ranges. Finally, Line 3 crosses the very southernmost part of Coaxial Segment at 46:07N. No shadow zones or delayed arrivals are evident on record sections from this line, indicating that the Coaxial magma chamber does not extend this far south.

Some insight into the dimensions of the magma chamber can be gained by simple, forward modeling of the traveltimes of Line 1. We begin with a three–dimensional model of the region in which the velocity field is parameterized on an irregular tetrahedral grid, with prescribed water velocity and bathymetry drawn from multibeam sonar measurements. The velocity field is initially a best fitting one–dimensional structure, draped onto the bathymetry. We then perturb this velocity field with a LVZ located beneath Coaxial Segment. The position of the delayed arrivals on Line 1 place strong constaints on the size and position of the LVZ along the segment: its southern end must be near 46:07N and it must extend at least 3 km northward; its width must be about 2 km; and the low velocities must occur at least at 4–5 km below sea level (about 2–3 km below sea floor). The data are not able to distinguish whether the LVZ persists north of 46:09N, nor to detect whether it extends beneath 5 km depth below seafloor. The minimum velocity required depends on how the velocity is assumed to vary within the perturbed area. A model in which it linearly decreases towards the center of the perturbation requires a minimum velocity of about 3 km/s (fig app.4). The Coaxial magma chamber is similar in width and overall traveltime

delay to the ones on the fast–sprading East Pacific Rise (EPR) at 9:30N (Toomey et al. 1990) and at 13:00N (Harding et al. 1989).

A tomographic inversion is also performed, using data from all lines and OBS's (16,700 Pg traveltimes), including those around Axial Volcano. Traveltimes and their Frechet derivatives are calculated using ray theory, and a linearized damped least–squares meathod is used to update the velocity field. Three iterations of the inversion are performed, starting with the bathymetrically–draped one dimension model, that result in a 54% reduction of the root mean square traveltime error. The final three–dimensional velocity field clearly reproduces all of the features evident from the simpler analysis (fig app.4). Of particular interest is the lack of connectivity of the Coaxial and Axial magma chambers, at least at mid–crustal depths. The two magma chambers are separated by about 10 km of basalt with normal compressional velocities (in the 6.0–6.5 km/s range) that show no sign of containing magma. Checkerboard–style resolution tests (not shown) indicate that the spatial resolution of the inversion is suffiently good in the critical region between the two magma chambers to detect connectivity, if it existed in the 2–6 km below sea level depth range.

The imaged part Coaxial magma chamber has a minimum volume of about 6 km3. While the relationship between seismic velocity decrease and melt fraction is imprecisely known, we estimate a minimum of 10% using the lab and theoretical studies of Takei (1998), Sato et al. (1989), and Christensen (1979).

The imaged portion of the magma chamber thus contains a minimum of about 0.6 km^3 of melt, sufficient to produce about 4 dikes of the size of the 1993 dike (with the 1 m width discussed by Embley et al. 2000). The magma chamber can supply crust at a 5.5 cm/yr spreading rate for at least 40 years, and perhaps longer, given that the magma chamber may extend northward out of the imaged area.

Two lines of reasoning suggest that the magma chamber may extend northward to about 46:12N (i.e. a total length of 5–6 km). The axial high, which represents the magmatically most robust part of the segment, extends to about there. Furthermore, the southernmost earthquakes associated with the 1993 dike propagation occured at about 46:12N. They may mark the point at the north end of the magma chamber at which the dike began. The total volume of melt in the magma chamber may therefore be about 1 km^3.

The 1993 dike propagated steadily over a three day period from the the Source Site to the so–called Flow Site, 40 km further north (at 46:32N), where it surfaced as a lava flow (Fox et al. 1995). The steady propagation strongly suggests that no further magma chambers occur along this 40 km length of Coaxial Segment, because such features would act to reduce the stress at the dike tip and to slow its propagation. There appears to be no source of magma further north along Coaxial Segment that could recharge the magma chamber. Recharge of the Coaxial magma chamber from Axial also appears to be ruled out, out on the grounds that their lavas have different chemistries (Embley et al.

2000) and because they appear to be unconnected on the seismic images. Thus we are lead to conclude that Coaxial is being recharged from a mantle source below. The mantle sources of the hot spot related Axial Volcano and Coaxial Segment of a ocean ridge thus appear to be separated horizontally by only 10–20 km, and yet remain chemically distinct. Magma transport through the melt generation region of the uppermost mantle (which extends to at least 75 km depth) must, when magma reaches the base of the crust, be focused to horizontal length scales of only 5–10 km, which is to say to relatively narrow conduits.

References

Butterfield, D., I.R. Johnson, G.J. Massoth, R.A. Feely, K.K. Roe, R.W. Embley, J.F. Holden, R.E. McDuff, M.D. Lilley and J.R. Delaney, Seafloor eruptions and evolution of hydrothermal fluid chemistry, *Philos. Trans. R. Soc. London, Ser. A., 355,* 369–386, 1997.

Christensen, N.I., Compressional wave velocities in rocks at high temperatures and pressures, critical thermal gradients, and crustal low–velocity zones, *J. Geophys. Res. 84,* 6849–6857, 1979.

Dziak, R.P. and C.G. Fox, The January 1998 earthquake swarm at Axial Volcano, Juan de Fuca Rige, Hydroacoustic evidence for seafloor volcanic activity, *Geophys. Res. Lett. 26,* 3425–3428, 1999.

Embley, R.W., W.W. Chadwick, M.R. Perfit, M.C. Smith and J.R. Delaney, Recent Eruptions on the Coaxial segment of the Juan de Fuca Ridge: Implications for mid–ocean riudge accetion processes, *J. Geophysical Res 105,* 16501–16525, 2000.

Fox, C.G., In situ ground deformation measurements from the summit of Axial Volcano during the 1998 volcanic episode, *Geophys. Res. Lett. 26,* 3437–3440, 1999.

Fox, C.G. W.E. Radford, R.P. Dziak, T.K. Lau, H. Matsumoto and A.E. Schriener, Acoustic detection of a seafloor presading episode on the Juan de Fuca Ridge using military hydrophone arrays, *Geophys. Res. Lett. 22,* 131–134, 1995.

Harding, A.J., J.A. Orcutt, M.E. Kappus, E.E. Vera, J.C. Mutter, P. Buhl, R.S. Detrick and T.M. Brocher, Structure of young oceanic crust at 13N on the East Pacific Rise from expanding spread profiles, *J. Geophys. Res. 94,* 12163–12196, 1989.

Sato, H., S.I. Sacks and T. Murase, The use of laboratory velocity data for estimating temperature and partial melt fraction in the low–velocity zone; comparison with heat flow and electrical conductivity studie, *J. Geophys. Res. 94,* 5689–5704, 1989.

Takei, Y., Constitutive mechanical relations of solid–liquid composites in therms of grain–boundary contiguity, *J. Geophys. Res. 103,* 18183–18203, 1998.

Toomey, D.R., G.M. Purdy, S.C. Solomon & W.S.D. Wilcock, The three–dimensional seismic velocity structure of the East Pacific Rise near latitude 9:30N, *Nature 347,* 639–644, 1990.

Webb, S.C., Broadband seismology and noise under the ocean, *Reviews of Geophysics 36,* 105–142, 1998.
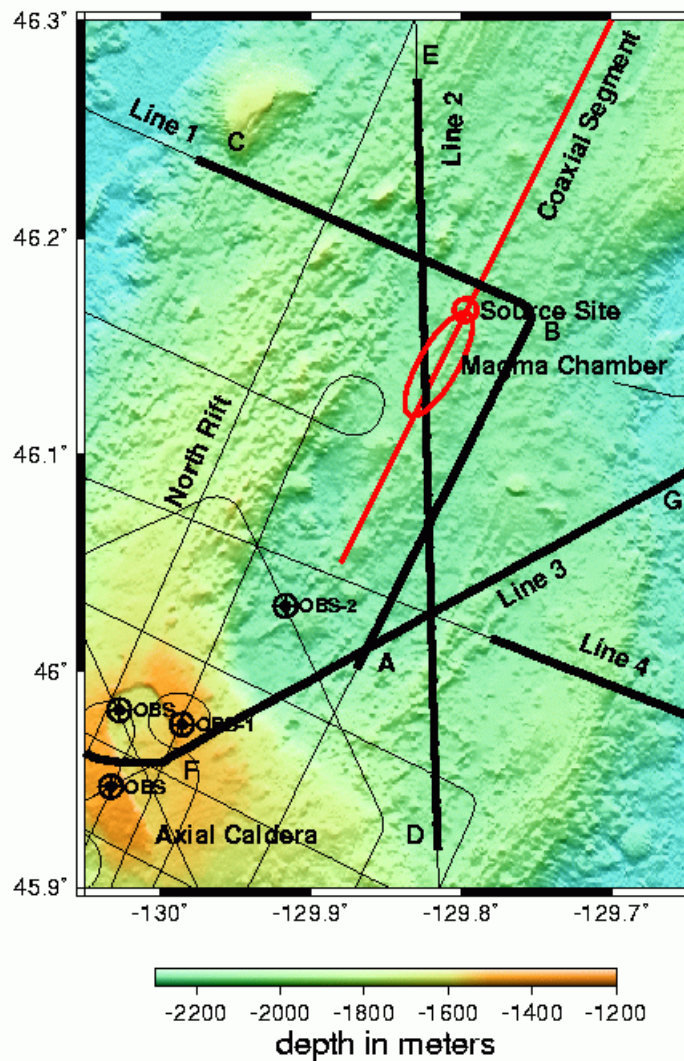
Figure App.1 Bathymetric map of Coaxial Segment (red line) and Axial volcano (lower left), showing Ocean Bottom Seismometers (OBS's) and lines of airgun shots (lines). Four lines discussed in text are highlighted in bold. The Source Site of the 1993 eruption and the magma chamber discussed in this study are shown in red. Bathymetric data courtesy of the National Oceanic and Atmospheric Administration.
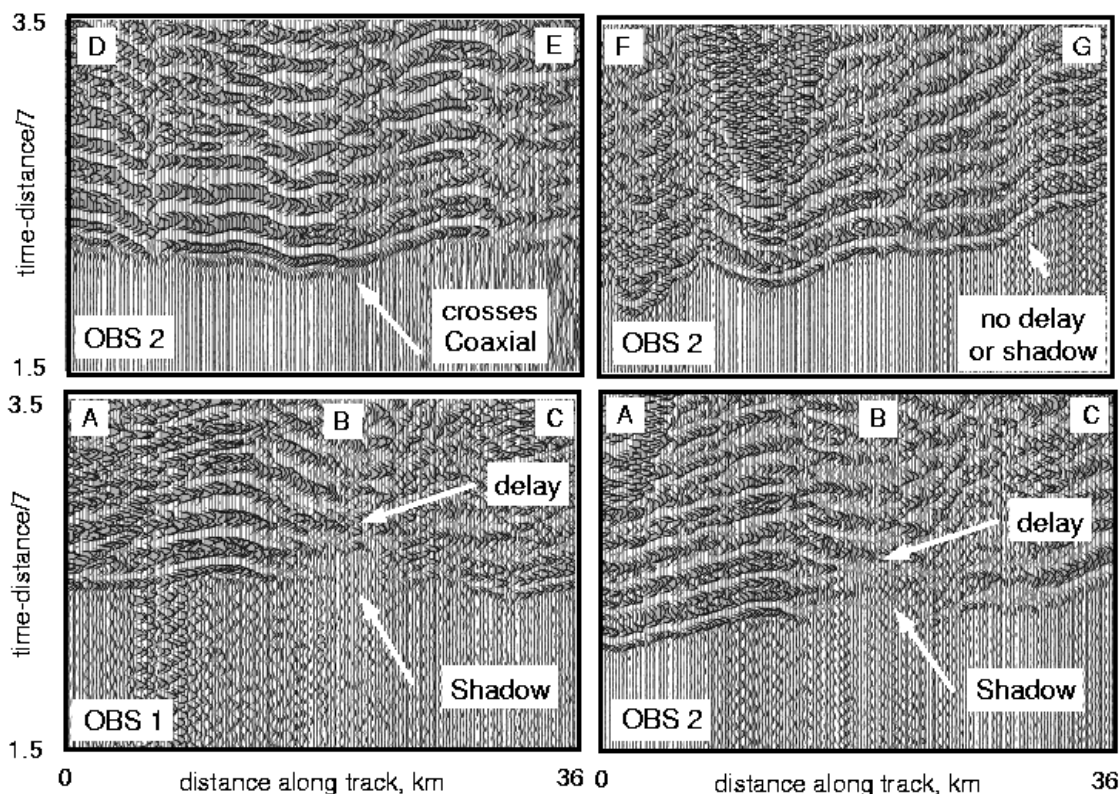
Figure App.2 Vertical–component seismic record sections, plotted as a function of distance along the ship track and reduced to 7 km/s. (Bottom left) Line 1 to OBS 2. (Bottom Right) Line 1 to OBS 2. Line 1 crosses the Source Site of the 1993 Coaxial Eruption. Both OBS's record a prominent delated arrival associated with a magma chamber beneath the source site. (Top left) Line 3 to OBS 2. Line 3 crosses Coaxial Segment well south of the sourth site. No delayed arrival is observed. (Top Right) Line 2 to OBS 2. Line 2 has about the same source–receiver ranges as does line 1, but does not cross Coaxial Segment. No shadowed or delayed arrivals are evident.

Figure App.3 Traveltime curves of Line 2 to OBS 2 data (squares), plotted as a function of of distance along the ship track and reduced to 7 km/s. Predicted traveltimes (crosses) are for a model with a one-dimensional bathymetrically-draped background compressional velocity structure perturbed by a small magma chamber located beneath the Source Site. (Top Graph) No magma chamber; (2nd Graph From Top) Magma velocity of 5 km/s; (3nd Graph From Top) Magma velocity of 4 km/s; (Bottom Graph) Magma velocity of 3 km/s. A magma velocity of 3 km/s is needed to fit the promenant delayed arrival in the 27–28 km distance range.
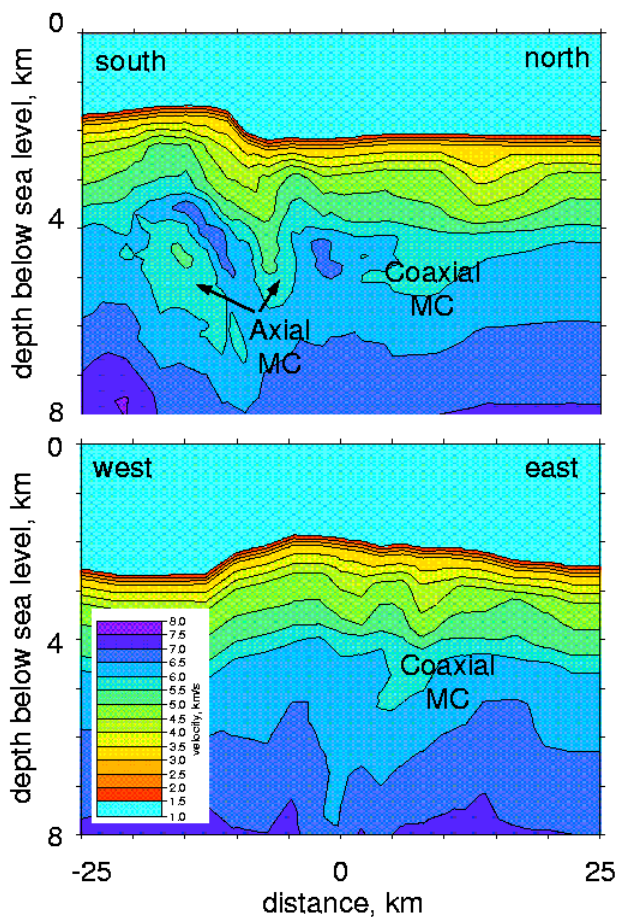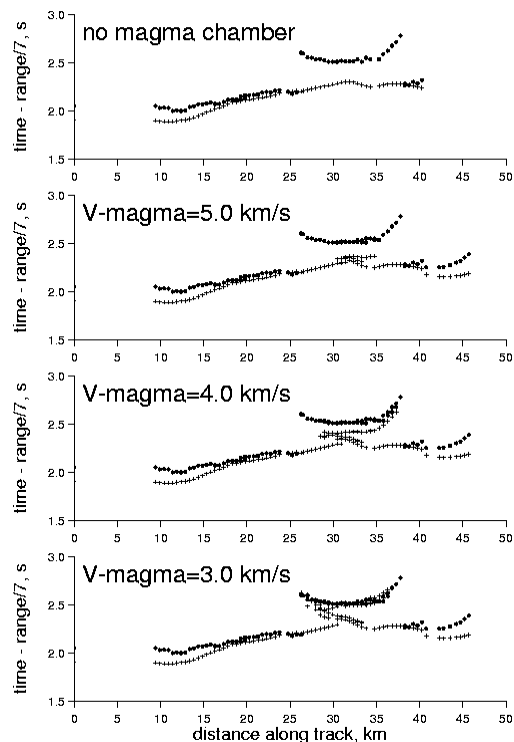
Figure App.4 Vertical cross–sections through the three–dimensional compressional velocity model produced by traveltime tomography. (Top) Cross–section along the axial of Coaxial Segment. This cross–section intersects both Axial volcano and Coaxial Segment magma chambers. (Bottom) Segment–perpendicular cross–section. This cross–section intersects only the Coaxial magma chamber.